PHOTONICS INSIGHTS

Revolutionary meta-imaging: from superlens to metalens

Tao Li,[a,*] Chen Chen,[a,*] Xingjian Xiao,[a] Ji Chen,[b] Shanshan Hu,[a] and Shining Zhu[a,*]

[a]National Laboratory of Solid State Microstructures, Key Laboratory of Intelligent Optical Sensing and Manipulation, Jiangsu Key Laboratory of Artificial Functional Materials, College of Engineering and Applied Sciences, School of Physics, Nanjing University, Nanjing, China

[b]National Mobile Communications Research Laboratory, School of Information Science and Engineering, Frontiers Science Center for Mobile Information Communication and Security, Southeast University, Nanjing, China

Abstract. The refractive-lens technique has been well developed over a long period of evolution, offering powerful imaging functionalities, such as microscopes, telescopes, and spectroscopes. Nevertheless, the ever-growing requirements continue to urge further enhanced imaging capabilities and upgraded devices that are more compact for convenience. Metamaterial as a fascinating concept has inspired unprecedented new explorations in physics, material science, and optics, not only in fundamental researches but also novel applications. Along with the imaging topic, this paper reviews the progress of the flat lens as an important branch of metamaterials, covering the early superlens with super-diffraction capability and current hot topics of metalenses including a paralleled strategy of multilevel diffractive lenses. Numerous efforts and approaches have been dedicated to areas ranging from the new fascinating physics to feasible applications. This review provides a clear picture of the flat-lens evolution from the perspective of metamaterial design, elucidating the relation and comparison between a superlens and metalens, and addressing derivative designs. Finally, application scenarios that favor the ultrathin lens technique are emphasized with respect to possible revolutionary imaging devices, followed by conclusive remarks and prospects.

Keywords: optics; imaging; metamaterial; superlens; metalens.

Received Oct. 10, 2022; revised manuscript received Dec. 3, 2022; accepted Dec. 16, 2022; published online Mar. 31, 2023.

[DOI: 10.3788/PI.2023.R01]

1 Introduction and Overview

For human beings, more than 80% of information is obtained through vision, and we can see how important the eye is as an imaging system. The invention of optical lenses implemented versatile powerful imaging devices that significantly expand the scope of human vision, such as microscopes, telescopes, and spectroscopes. Moreover, by incorporating imaging sensors, these imaging devices can record both static images and dynamic videos that greatly enrich human life. Refractive lenses play an extremely important role in optical imaging devices, which assemble light by reflection and refraction at the interface of two media with different refractive indices, governed by the well-known Snell's law[1]. Over time, optical imaging technology based on refractive lenses has been well developed. Systematic optical engineering with successive upgrading has given rise to outstanding imaging capabilities, such as high resolution, wide field of view (FOV), and broad wavelengths. Nevertheless, these systems are becoming increasingly complex with multiple optical elements such as cascaded lenses, internal reflection mirrors, and polarizers, which makes systems bulky, heavy, and inconvenient for portability.

From a fundamental perspective, these developments in refractive lenses cannot achieve super-resolution to break the diffraction limit as restricted by the optical principle. Although several strategies have been developed to access super-resolution microscopy based on luminescence techniques [such as STED (stimulated emission depletion microscopy) and STORM (stochastic optical reconstruction microscopy)] and achieved great success[2–6], they are not strictly optical imaging processes in principle, and their imaging functionality is still limited. According to intuitive scientific expectations, an optically perfect lens is always of revolutionary significance in

*Address all correspondence to Tao Li, taoli@nju.edu.cn; Chen Chen, chenchen2021@nju.edu.cn; Shining Zhu, zhusn@nju.edu.cn

imaging technology. On the other hand, more compact, lightweight, and stable optical systems are the ever-growing requirements in modern life. The traditional refractive lens relies on light propagation that inevitably makes the devices bulky, especially for those systems with cascaded compound lenses. Recent advances in computational imaging (including lensless imaging) have shown a successful solution to reduce the complexity of the optical system by discarding refractive lenses[7]. Nevertheless, they are not a real physical process, and the image quality strongly relies on post-processing algorithms, such as iterative phase recovery[8], compressive sensing[9], and Fourier ptychography[10]. It inevitably requires computational resources that are time consuming, and sometimes needs particular prior knowledge for imaging reconstruction.

Metamaterial, as a new conceptual revolution in material science, was proposed at the beginning of this century, and is composed of subwavelength unit cells with artificial electromagnetic (EM) responses that give rise to very flexible and abundant modulations of EM/optical parameters (e.g., permittivity, permeability, refractive index) at both global and local scales[11]. Based on this new design philosophy, not only can the permittivity be adjusted at will, but also the non-unit permeability can be achieved in the optical region and even to negative values by local magnetic resonances[12,13]. Once the permittivity and permeability both reach negative, a novel material is implemented showing an unusual effect of negative refraction, which is so-called negative index material (NIM)[14–16]. Besides many unusual effects and phenomena revealed in the NIM, John Pendry from Imperial College, London, theoretically derived an amazing function of perfect-lens imaging with unlimited resolution by a NIM slab due to its capability of amplifying the evanescent wave, which carries information of unlimited small features of an object[17]. In a real system, one cannot reach such an ideal condition in both theory and experiments, and an unlimited perfect lens is unachievable, though some NIMs have been demonstrated in the optical regime[18]. Then the concept of a superlens was proposed and demonstrated with the capability to break the diffraction limit[19,20].

In spite of the conceptual revolution of a superlens, it is hardly adopted in real imaging applications due to the huge loss, harsh working condition, and extreme difficulty in device development. Although researchers thereafter extended the concept to a hyperlens by anisotropic NIM design with hyperbolic dispersion, most relevant studies were still limited at the stage of effect demonstrations[21,22]. In 2011, a two-dimensional (2D) version of metamaterial, so-called metasurface, was proposed based on a single layer of meta-atoms (i.e., subwavelength resonators) with local modulation on the light wavefront and polarization, which significantly enabled highly flexible manipulation of light refraction and reflection, and was termed as a generalized Snell's law by Federico Capasso's group from Harvard University[22]. Unlike its bulky counterpart, this metasurface is ultrathin (usually tens to hundreds of nanometers), which greatly reduces the propagating loss inside the material and eases nanofabrication difficulty. Now, many researches have been carried out on metasurfaces in explorations of new design strategies, new functionalities, and possible applications. Among them, a metasurface with a focusing phase, i.e., the metalens, has always been the focus of attention owing to the tremendous application potential in imaging technology.

During the past decade, the design methods of metasurfaces have been greatly enriched. Non-resonant geometric [Pancharatnam–Berry (PB)] phase and dynamic propagation phase are widely used in multi-functional metasurfaces, and the constituent material was extended from the initial metal to dielectric to further reduce loss, and make the high-efficiency devices more applicable. Therefore, a dielectric metalens was successfully demonstrated in 2016 showing an imaging performance comparable to conventional microscopes at certain wavelengths[23]. Afterwards, more efforts have been made towards imaging applications, such as efficiency improvement[24], and chromatic and image-aberration corrections[25–27]. Another paralleled strategy based on a multi-level diffractive lens (MDL) was developed showing its advantage in large-scale achromatic flat-lens designs[28]. However, recent studies have shown that the imaging performances of metalenses/MDLs in efficiency, working bandwidth, image aberrations, FOV, etc., are mutually constrained[29–31]. Therefore, the comprehensive performance of today's metalenses is still inferior to traditional refraction lenses and compound lenses. Thus, it is necessary to carefully examine the application advantages of metalenses as considered to replace the conventional counterparts. In the meantime, new opportunities are opening for metalens imaging techniques with ultra-compactness and ultra-flexibility with respect to the current rapidly changing information society. Figure 1 displays the two branches of developing routes of optical materials to imaging flat lenses from natural materials and artificial metamaterials, both of which are ultimately working towards revolutionary imaging applications.

This review aims to provide a historic view on meta-imaging developments, including the evolution from metamaterials to metasurfaces, from perfect lens and superlens to metalens, where intriguing new physics have been revealed and fascinating functionalities are explored. Moreover, this review tries to clarify the most possible routes from the revolutionary metalens design to real applications with tremendous advantages or irreplaceable roles from recent sophisticated information from both academia and industry. Based on these considerations, this paper is organized in six parts. After the introduction and overview, we illustrate the invention of metamaterial and superlenses in the second part, and metasurfaces and metalenses in the third part. As a paralleled technique solution for flat-lens imaging, the development of MDLs as the upgraded version of conventional diffractive optical elements (DOEs) is addressed in the fourth part. Afterwards, we particularly emphasize the application scenarios that might be suitable to these flat lenses in the fifth part, where metalenses/MDLs are considered to give full play to their utmost advantages. Finally, in the summary, we provide conclusive remarks and prospects for this newly emerging flat lens with the impact on optical devices and technologies.

2 Metamaterials and Superlenses

2.1 Perfect Lens and Negative Index Material

Curiosity in nature exploration has driven researchers to explore the limits of imaging capability for centuries. In 1873, Abbe discovered the so-called diffraction limit, which describes an optical system such as a microscope that is unable to resolve two spots with a distance smaller than half a wavelength[32]. To explain this limitation, we refer to the wave nature of light, which can be classified into two types: propagating wave and

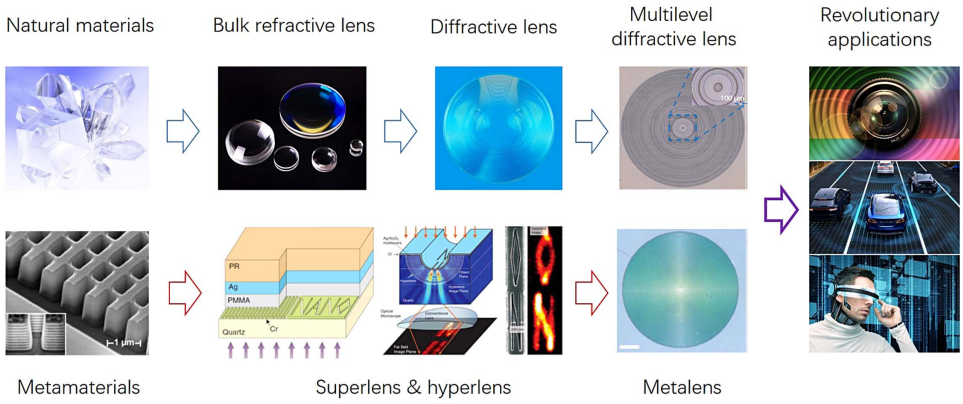

Fig. 1 Two branches of optical lens evolution towards revolutionary application in the information society, where the representative figures of metamaterials, superlenses, hyperlenses, metalenses, and multilevel diffractive lenses are adapted from Refs. [18,19,21,23,28], respectively.

evanescent wave. We are more acquainted with the propagating wave that has a real wave vector (k vector) in free space for propagation, by which most optical phenomena were revealed such as radiation, imaging, display, and projection. The evanescent wave loses the real k vector component in one or two dimensions, instead having an imaginary one, meaning that this kind of wave cannot radiate from the surface of an object. In fact, the origin of this evanescent wave lies in large k vectors in dimensions parallel to the object surface (defined as $k_{\parallel}$), which forces the normal component to be imaginary ($k_{\perp}$) according to the momentum conservation law. It can be interpreted in a very simple formula of the electric field of a light with plane wave form as

$$\mathbf{E} = \mathbf{E}_0(x, y)\exp(ik_z z - i\omega t), \tag{1}$$

where $k_z = \sqrt{k_0^2 - (k_x^2 + k_y^2)}$ corresponds to $k_{\perp}$, and k_x (k_y) belongs to $k_{\parallel}$. The evanescent wave can be deduced with respect to a large paralleled momentum aroused from the subwavelength structural features of an object surface (i.e., $k_{\parallel} > k_0$), which gives rise to an imaginary normal $k_{\perp}$ indicating an exponentially decaying wave away from the surface in the normal direction.

For an imaging system, the evanescent wave carries fine feature information and decays exponentially away from an object, and the conventional lens cannot capture this evanescent wave for imaging. Figure 2 schematically shows the radiation of light from an object surface with respect to different k vectors originating from different-sized features. It intuitively shows that an ultra-small structure generates the much larger G vector ($G = 2\pi/\Delta$, i.e., spatial frequency of surface structures; here, Δ is the corresponding feature size) than the free space k vector (k_0), which turns the normal component of the k vector (k_z) into an imaginary value that leads to the exponential decay of this evanescent field in normal direction.

In this regard, a conventional imaging system based on propagating light can capture the propagating wave that carries only information of feature sizes larger than the wavelength. Recovering the rapidly decaying evanescent wave that carries much smaller signatures of structures should be necessary. In 2000, John Pendry ingeniously derived a solution that can in

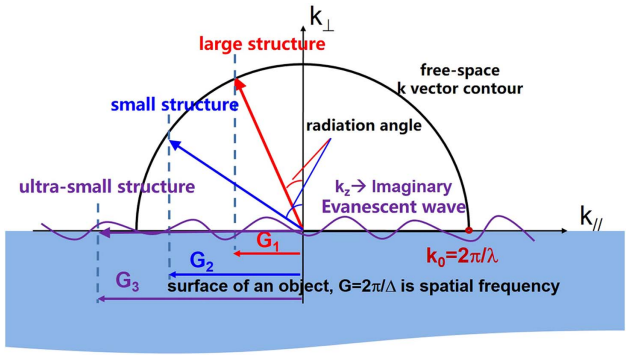

Fig. 2 Schematic (k space) of light radiation from a structured surface that carries information from details of different spatial frequencies.

principle perfectly recover the unlimited small features of a certain object, which is made of a slab NIM and so-called perfect lens[17]. For a brief interpretation, when light is normally incident from a vacuum (or air with $n = 1$) into a NIM slab with $n = -1$ (with simultaneous ε and μ, both of -1), the transmission coefficient in the NIM can be deduced as[17]

$$\lim_{\substack{\mu\to-1\\ \varepsilon\to-1}} T_P = \lim_{\substack{\mu\to-1\\ \varepsilon\to-1}} \frac{2\varepsilon k_z}{\varepsilon k_z + k_z'}\frac{2k_z'}{k_z' + \varepsilon k_z} \times \frac{\exp(ik_z' d)}{1 - \left(\frac{k_z' - \varepsilon k_z}{k_z' + \varepsilon k_z}\right)^2 \exp(2ik_z' d)} = \exp(-ik_z d), \tag{2}$$

where d is the propagation distance inside the NIM. From Eq. (2), one can find that when k_z is a purely imaginary value, the transmittance will get an exponential increase inside the NIM, implying a recovery of the super-resolution information decaying in free space. Therefore, a NIM slab works well as a perfect lens when the impedance matching condition is satisfied: $\sqrt{\varepsilon_1/\mu_1}/\sqrt{\varepsilon_2/\mu_2} = 1$.

However, how to implement a NIM with simultaneous negative ε and μ is still a big problem. In fact, the concept of NIM should be traced back to a bold thought experiment by Viktor G. Veselago half a century ago. In 1968, he published a paper to

demonstrate fancy phenomena of negative refraction by defining a material with simultaneous negative ε and μ[33]. Although it was not worked out even in a theoretical design until the new century, it illuminates the dawn of a new kind of material that does not exist in nature, which was later termed as metamaterial. Fortunately, the difficult problem was resolved by John Pendry, who first proposed a 3D metal wire mesh with an effective diluted electron density to control the permittivity to a suitable negative value in the microwave frequency region in 1996[34], and then a split ring resonator (SRR) was proposed to access a controlled negative permeability in 1999[35]. Based on these designs, the David Smith group from University of California San Diego successfully demonstrated the first negative refractive index material in the microwave region in 2001. It therefore triggered numerous researches for high-performance NIM at higher frequencies, even to the optical region in the following decade[15,16]. During this period, researches even bloomed into several sub-branches, for example, transformation optics[36] and metasurfaces[37], and extended to other wave-functional regimes, such as acoustic metamaterials[38], elastic wave metamaterials[39], and even water wave metamatierials[40]. In a more generalized sense, the research of material is gradually merging with other artificial micro/nano-structured materials such as photonic crystals and plasmonic crystals[41,42]. There have been a number of good review articles about the development of metamaterials that would be good choices for readers[11,43,44]. In this review, we mainly focus our topic from the viewpoint of lens imaging, and will not get into many details about the development of metamaterials. Nevertheless, it should be mentioned that although remarkable progress has been made in both design and fabrication techniques, the performances of negative index metamaterials in the optical region are quite poor due to the huge intrinsic loss and fabrication-induced imperfections. Moreover, the extreme difficulty in nanofabrication of such a 3D NIM prevents it from being an attractive and feasible route in development of optical instruments or techniques. So, when we ask whether the perfect lens has been developed to an applicable level based on the NIM with simultaneous negative ε and μ, the answer seems to be negative.

In fact, John Pendry's calculation in 2000[17] has revealed that for polarized light, it needs only one condition of either negative permittivity or negative permeability for such perfect lensing. Taking TM (p-polarized) light as an example, Eq. (2) gives the same result when only $\varepsilon = -1$ is satisfied[45]. It significantly brings convenience for verifying the feasibility of whether single-negative material can achieve super-resolution imaging. Reference [17] provides theoretical proof by employing a lossy metal (silver) with negative permittivity for calculation. According to the nonnegligible damping loss of the metal, a perfect image identical to the object cannot be achieved even in theoretical calculation; nevertheless, super-resolution has been accomplished by distinctly resolving slits with good subwavelength separation; see Figs. 3(c) and 3(d). Hence, such a non-ideal perfect lens is termed as a superlens.

2.2 Superlenses and Hyperlenses

The first experimental verification of a superlens was performed in 2005. Fang *et al.* elaborately fabricated an ultra-smooth silver film with proper thickness to enable it to work as a superlens for p-polarized light. In their experiments, a higher resolution of 89 nm was achieved, which is much smaller than the wavelength

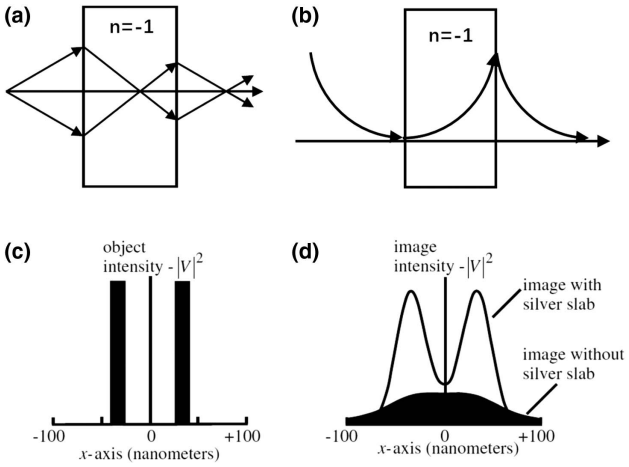

Fig. 3 (a) Schematic of light focusing (propagating wave) with a slab of NIM; (b) schematic of amplitude evolution of the evanescent wave, showing the recovery inside NIM of the decaying field intensity; (c) electrostatic field of two opaque slits with distances far smaller than the wavelength in the object plane, to be imaged by a silver lens; (d) electrostatic field in the image plane with and without the silver slab in place[17].

of illumination light ($\lambda = 365$ nm); see Fig. 4[19]. Although this super-resolution imaging was implemented in a very limited near-field region recorded by a photoresist, it is undoubtedly the first experimental demonstration of optical superlens imaging based on John Pendry's innovative concept. Unfortunately, this superlens cannot recover a super-resolution image far away from the lens interface, unless the NIM (with $n = -1$) has thickness identical to the imaging distance according to John Pendry's theory. It almost prohibits the possibility of using a single-layer metallic film to do so.

According to the discussion in Section 2.1, it has been proved that the implementation of a bulk NIM with simultaneous negative ε and μ by subwavelength nano-inclusions is extremely challenging at optical wavelengths. So using more continuous structures to compose the superlens would be a more feasible way. Theoretical studies on an optical hyperlens have been proposed by the use of an anisotropic medium with hyperbolic dispersion. Consider an anisotropic medium with its permittivity tensor of

$$\varepsilon = \begin{pmatrix} \varepsilon_x & 0 & 0 \\ 0 & \varepsilon_y & 0 \\ 0 & 0 & \varepsilon_z \end{pmatrix}. \tag{3}$$

Here, we define it as a uniaxial medium with the axis along the z direction; then we rewrite $\varepsilon_z = \varepsilon_\parallel$, $\varepsilon_x = \varepsilon_y = \varepsilon_\perp$. Substituting Eq. (3) into the Maxwell equation, we have an eigen function of

$$\left(\frac{\omega^2}{c^2}\varepsilon_\perp - k^2\right)\left[\frac{\omega^4}{c^4}\varepsilon_\perp\varepsilon_\parallel - \frac{\omega^2}{c^2}\varepsilon_\perp(k_x^2 + k_y^2) - \frac{\omega^2}{c^2}\varepsilon_\parallel k_z^2\right] = 0, \tag{4}$$

which indicates two solutions as

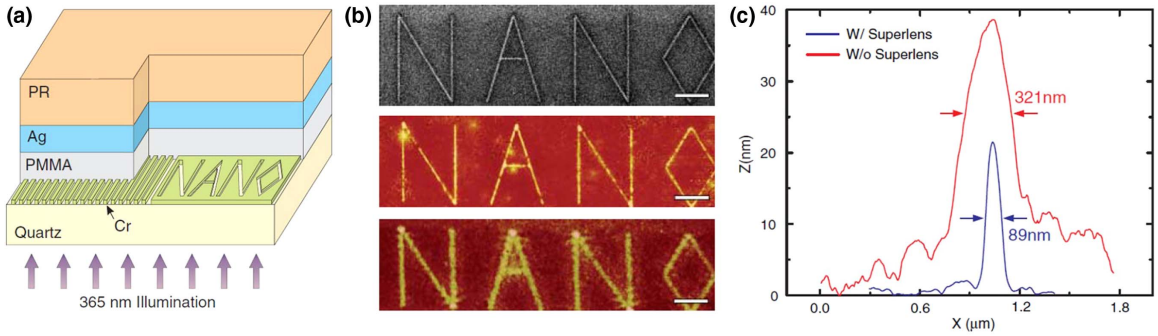

Fig. 4 (a) Schematic of the experiment of superlens imaging with 35-nm-thick silver film. (b) An arbitrary object, "NANO," was imaged by a silver superlens, where the upper panel is the object fabricated in Cr film, middle shows images by Ag superlens, and bottom is the projection results as the Ag superlens is replaced by a PMMA spacer. (c) Detailed line information of the feature size captured by the Ag superlens and without it[19].

$$\frac{\omega^2}{c^2}\varepsilon_\perp - k^2 = 0, \tag{5a}$$

$$\frac{\omega^4}{c^4}\varepsilon_\perp\varepsilon_\parallel - \frac{\omega^2}{c^2}\varepsilon_\perp(k_x^2 + k_y^2) - \frac{\omega^2}{c^2}\varepsilon_\parallel k_z^2 = 0. \tag{5b}$$

Equation (5a) is an ordinary wave equation with respect to TE polarization, while Eq. (5b) implies an extraordinary wave of TM polarization with a dispersion relation of

$$\frac{\omega^2}{c^2} = \frac{k_x^2}{\varepsilon_\parallel} + \frac{k_z^2}{\varepsilon_\perp}, \tag{6}$$

which is a well-defined hyperbolic dispersion if $\varepsilon_\parallel$ and $\varepsilon_\perp$ have opposite signs. It can be further classified into two types, depending on which component is negative as Fig. 5 shows.

From Fig. 5, we find that both the phase and group velocity inside the hyperbolic metamateial can be carefully engineered by merely setting its negative permittivity components without any magnetic components involved. It significantly reduces the difficulty in realization of NIM. Thereafter, several kinds of negative refraction and super-resolution imaging at optical wavelengths were successfully implemented, where flat lenses based on such hyperbolic NIMs are called hyperlenses. For example, Jie Yao *et al.* fabricated a silver nanowire array in a dielectric matrix by employing the anodic alumina template technique[47], and successfully demonstrated negative refraction at an optical wavelength of 780 nm. According to Eq. (5), this negative refractive index depends on the polarization (e.g., TM polarization); the authors even demonstrated a negative index of −4.0 for TM polarized light by analyzing the refraction angle, which is distinctively different from TE-polarized light with an effective refractive index of +2.2 [see Fig. 6(a)]. Another typical NIM was demonstrated in 2013 by Ting Xu *et al.*[48]. They reported the experimental implementation of a negative metamaterial with a working wavelength to even ultraviolet ($\lambda_0 \sim 363.8$ nm). It was implemented by stacked plasmonic waveguides as the scheme in Fig. 6(c), yielding an omnidirectional negative refraction for TM-polarized light. Moreover, the authors demonstrated flat lensing in free space of 2D objects

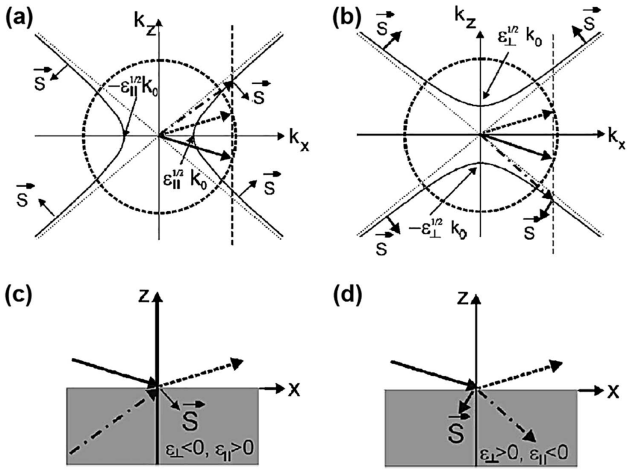

Fig. 5 Schematics of light propagations and wave vectors in uniaxial media with principal dielectric constants of different signs[46]. (a) Wave vector diagram (k space) for a uniaxial medium with $\varepsilon_\perp < 0$, $\varepsilon_\parallel > 0$. The solid hyperbola represents wave vectors of all propagating waves in the medium. The long solid arrow and dashed arrow identify the wave vector incident on the surface of the medium and reflected wave vector, respectively. The dashed-dotted arrow is the transmitted wave vector. The short solid arrow indicates the Poynting vector (S) of the transmitted wave indicating the direction of energy flow. (b) Wave vector diagram for a uniaxial medium with $\varepsilon_\perp > 0$, $\varepsilon_\parallel < 0$. (c), (d) Waves in real space for $\varepsilon_\perp < 0$, $\varepsilon_\parallel > 0$, and $\varepsilon_\perp > 0$, $\varepsilon_\parallel < 0$, respectively.

beyond the near field[48]. Though this kind of multilayered NIM demonstrates the flat-lens function as predicted by Viktor G. Veselago, it still lacks super-resolution capability due to the non-ideal implementation in both sample fabrication and optical characterization. Nevertheless, achieving a super-resolution image in the far field has been previously circumvented by Zhaowei Liu *et al.*, where a cylindrical metamaterial-composed hyperlens has been developed to image a sub-diffraction resolution of 130 nm with respect to a working wavelength of 365 nm[21]. This cylindrical hyperlens is constructed by multilayered metal/dielectric units in a curved form, which can magnify the object by transforming scattered

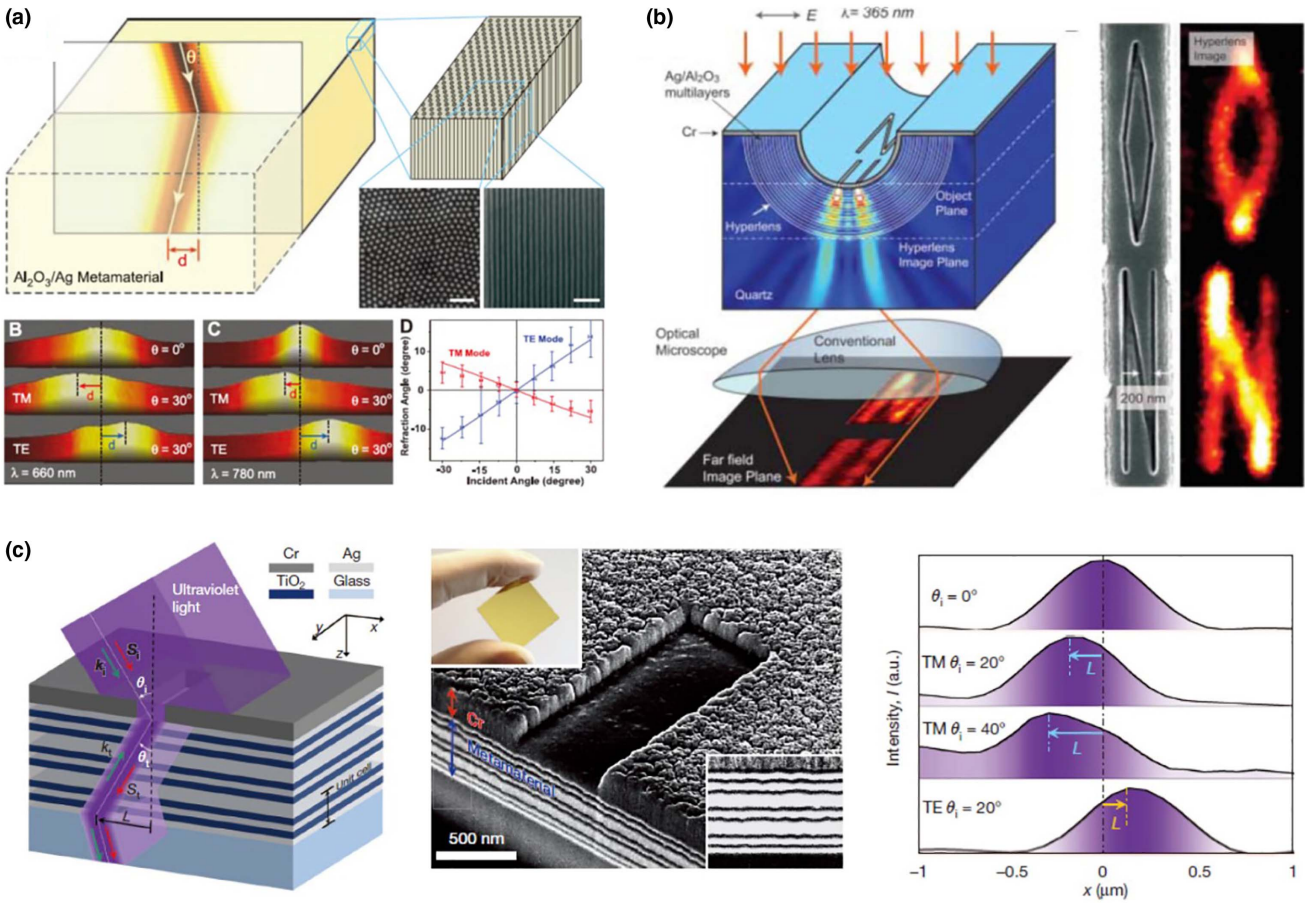

Fig. 6 Several kinds of hyperbolic metamaterials. (a) Negative index material for TM-polarized light realized by silver nanowire array[47]. (b) Hyperlens formed by cylindrical multilayered nanostructures for far-field super-resolution imaging[21]. (c) Multilayered negative index materials working in thin UV wavelength region, where negative refraction properties are measured for TM polarization (right panel)[48].

evanescent waves into propagating waves, and thus project a high-resolution image into the far field[21] [see Fig. 6(b)]. This design was further extended by Zhaowei Liu's group in the following years, and has been summarized in a review article[49].

2.3 In-plane Lensing

By reviewing the researches on negative index metamaterials for the past two decades, it is not difficult to find that with the increase of working frequency from the initial microwave to optical regime, the design with double/single-negative EM parameters (ε and μ) has been gradually replaced by more continuously hyperbolic dispersive metamaterials. It is not only due to easier nanofabrication, but also because more continuous components have lower loss, which is vital in real applications. Nevertheless, the huge fabrication difficulties, inevitable and nonnegligible large loss, and very limited and strict application scenarios significantly prohibit the further development of optical superlenses and hyperlenses. Interestingly, there were some 2D counterparts proposed and demonstrated in negative refraction and even superlens imaging in the planar dimension, which might illuminate some new dawn for future feasible applications.

In fact, in Ref. [48], the authors attributed it to the negative dispersion of plasmonic waveguides, which has been demonstrated by the same group in planar negative refraction in a metal/dielectric/metal waveguide system[50]. In 2007, Henri J. Lezec *et al.* demonstrated the first negative refraction at the visible frequency by employing a plamsonic waveguide. Negative indices were achieved with the use of an ultrathin $Au/Si_3N_4/Ag$ waveguide sustaining a surface plasmon polariton (SPP) mode with antiparallel group and phase velocities. All-angle negative refraction was observed at the interface between this bimetal waveguide and a conventional $Ag/Si_3N_4/Ag$ slot waveguide (see Fig. 7). Although manipulating the SPP wave in a metal surface has been intensively studied by versatile strategies before and after this work, none of them clearly demonstrated the negative fraction behaviors of a guided mode. Unfortunately, even in Ref. [48], the authors did not show superlens (or hyperlens) imaging with a subwavelength function. The difficulty lies not only in the complicated construction of such kind of negative dispersion waveguides, but also the challenge to form a proper interface for negative and positive index materials with impedance matching. Otherwise, a big impedance mismatch will obscure the performance of super-resolution imaging by in-plane superlenses/hyperlenses.

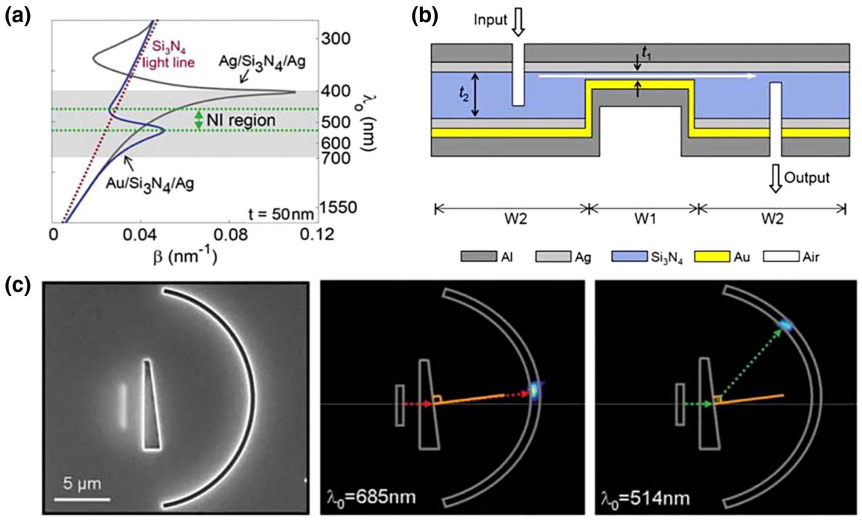

Fig. 7 Negative refraction in the plasmonic slot waveguide system at visible frequency[50]. (a) SPP dispersions in $Ag/Si_3N_4/Ag$ and $Au/Si_3N_4/Ag$, where the regions of opposite dispersions within two waveguides are marked. (b) Schematic of the hybrid waveguide system, where the negative refraction area is controlled by the waveguides with gap size of t_1. (c) SEM image of sample (left panel); experimental results of the positive refraction at $\lambda_0 = 685$ nm (middle panel) and negative refraction at $\lambda_0 = 685$ nm (right panel).

Alternatively, with the development of dispersion management of waveguide arrays, many exotic light propagations have been realized in both plasmonics and dielectric waveguide systems[51–54]. From the viewpoint of effective media, when the lattice period is smaller than $\lambda/2$, this waveguide array can be regarded as a continuous 2D metamaterial or metasurface (note that this is not identical to the metasurface proposed in 2011[22]) with its dispersion determined by the coupling among waveguides. Both theoretical and experimental results have shown that positive and negative couplings give rise to the positive and negative dispersions of an effective medium, respectively. Therefore, it is possible to achieve a 2D version of superlens/hyperlens imaging with super-resolution by carefully tailoring the coupling among waveguides.

In 2013, Liu *et al.* theoretically proposed and analyzed the dispersion of a plasmonic metasurface constructed by a metal-groove waveguide array[55]. It was observed that the metasurface can drastically modify the dispersion of surface plasmons, giving rise to flat or hyperbolic frequency contours that have the capability to diverge/converge the in-plane SPP wave. As a result, an explicit correspondence relationship was established between the dispersion and refraction, where negative refraction is vividly simulated with inverse hyperbolic dispersion[55]; see Fig. 8(a). More importantly, this work demonstrated that the plasmonic ridge waveguide can tune the coupling between each, which indeed gives rise to a tailorable dispersion that is very difficult in 3D metamaterials. The underlying physics lies in two competitive coupling mechanisms from the electrical field between the upward surfaces and side walls [see Fig. 8(b)], which was later elucidated in a plasmonic simulation on massless Fermion with linear dispersion[56]. It was implemented by employing a positive coupling and negative coupling with proper structural parameters in a ridge plasmonic waveguide array[56].

In principle, these negative hyperbolic dispersions can give rise to in-plane superlens imaging based on the above plamonic designs[57–59]. Unfortunately, they are very difficult to realize in experiments since the huge loss will cover up the phenomena[57–59]. Then, a low-loss dielectric counterpart would be a good choice. However, different from the plasmonic system, negative coupling is an obstacle in dielectric waveguides although there much diffraction management has been investigated[51–53]. Interestingly, in 2012, the Alexander Szameit group proposed a dielectric waveguide array with a sinusoidally curved trajectory along the propagation direction to experimentally simulate massless Dirac particles and conical diffraction, as shown in Fig. 8(c). Therein, the effective coupling coefficient is revealed following a zeroth-order Bessel function as

$$c_{\text{eff}} = c_j J_0\left[A\frac{4\pi^2 n_0}{P\lambda}(x_j - x_{j-1})\right], \tag{7}$$

which can be tailored to be positive, negative, or even zero by carefully adjusting the bending amplitude or lattice period[60]. Although this work itself was implemented in weakly coupled waveguides with large lattices far from an effective medium region (i.e., metasurface), it undoubtedly indicates the possibility to access effective negative coupling by bending the dielectric waveguides.

In 2020, Wange Song *et al.* successfully demonstrated an in-plane superlens by arranging a closely packed silicon waveguide with a lattice smaller than $\lambda_0/2$ ($\lambda_0 = 1550$ nm, the working wavelength in free space)[61]. It was implemented by cascading two segments of waveguide arrays (one straight and the other curved) with the same subwavelength lattice. Although in such a densely packed waveguide system the simulated effective coupling coefficient deviates from the predicted Bessel function (which was later clarified due to deviations from the paraxial approximation[62]), it still undergoes the regions from positive to negative and even reveals a very strongly negative value, which indeed helps to find an identical coupling

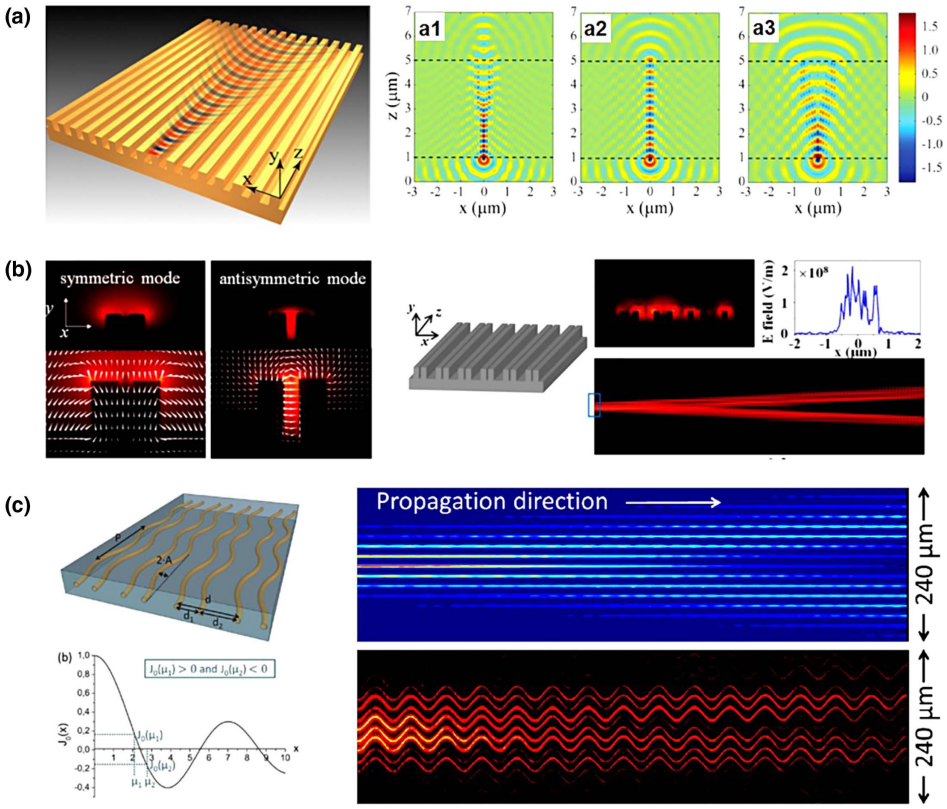

Fig. 8 (a) Waveguide array constituting metallic metasurface for manipulating the surface plasmon wave with (a1) positive dispersion, (a2) zero (flat) dispersion, and (a3) negative dispersion[55]. (b) Simulated symmetric and antisymmetric modes of coupled plasmonic ridge waveguide that gives rise to positive and negative dispersions for the simulation of massless Dirac Fermion[56]. (c) Curved dielectric waveguides in coupling with Bessel type of effective coupling coefficient that gives rise to the simulation of massless Dirac Fermion[60].

strength for both positive and negative ones [see Fig. 9(a)]. Therefore, the positive and negative couplings among waveguides give rise to positive and negative hyperbolic dispersions, respectively, and thus a perfect interface of a NIM superlens adjacent to a normal medium can be constructed by cascading two kinds of waveguide arrays. Figure 9(b) shows the theoretical calculations of light propagation within the waveguide array of totally straight, curved, and cascaded forms. It is easy to find the spreading field because discrete diffraction converges into the subwavelength singlet waveguide in the cascaded case, showing in-plane point-to-point focusing, while the purely straight or curved ones display only discrete diffractions. A further experiment was carried out in a silicon waveguide array, and the design scheme and fabricated samples are shown in Fig. 9(c), in which fan-out gratings are attached to the major waveguides for coupling in and out. Figure 9(d) displays measured optical results that clearly reveal the point-to-point subwavelength imaging from two opposite ports (the period of the waveguide array is 700 nm, which is smaller than half the working wavelength of 1550 nm). On the contrary, the results from totally straight and curved samples show an obviously spreading field in multiple output ports (more details in Ref. [61]). The subwavelength refocusing performance demonstrates the implementation of in-plane superlen/hyperlens imaging. Note that both straight and curved waveguides almost have the same propagating constant, which significantly gives rise to perfect impedance matching and results in good imaging performance in the optical region.

It should be mentioned that most previous superlenses and hyperlenses usually suffered from limited incident angles due to the anisotropic design. Very recently, a new approach[63] based on a topological photonic design has been proposed to realize all-angle reflectionless negative refraction for all incident angles, as shown in Fig. 10[63]. The proposed metamaterial possesses two Weyl points of opposite topological charges. By interfacing the metamaterial with a perfect electric conductor (PEC) or a perfect magnetic conductor (PMC), the Fermi arc connecting the two Weyl points can take the form of a half-circle possessing a positive or negative refractive index. Importantly, due to the topological protection, there is no reflection at the interface between the PEC and PMC covered areas, giving rise to all-angle negative refraction without reflection at the boundary. It provides a new platform for manipulating the propagation of surface waves, which would possibly find new applications in the construction of integrated photonic devices.

As a short summary for this section, we have witnessed the remarkable research progress in metamaterials ranging from the NIM, superlens, and hyperlens, to even in-plane lensing. In fact, the researches of bulk metamaterials are far beyond these, for example, the sub-branch of transformation optics including invisible cloaking[64–66], illusion optics[67,68], mimicking celestial

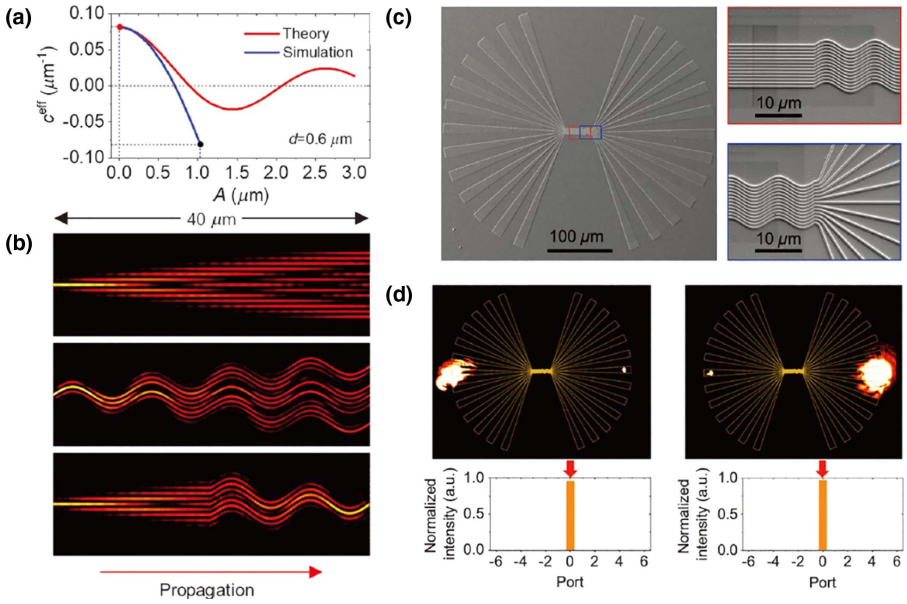

Fig. 9 (a) Simulated effective coupling coefficient in densely arranged Si waveguides with a comparison of theoretical Bessel function. (b) Simulated light propagations in all straight waveguides (positive dispersion, top panel), all curved waveguides (negative dispersion, middle panel), and the cascaded one (superlens, bottom panel). (c) Fabricated Si waveguides with ample cascaded segments and fan-out input and output couplers. (d) Experimentally recorded in-plane superlens imaging input from two opposite ports[61].

mechanics[69–71], etc. From the perspective of revolutionary imaging technology, super-resolution imaging is one of the biggest motivations for researchers, although there have been huge obstacles to face to date. From the discussion in this section, it is not hard to conclude that the original perfect/superlenses proposed by John Pendry have been demonstrated in various systems in both simulation and experiments. Although a direct application in feasible and valuable scenarios (e.g., mass-nanolithography) seems to still have many technical challenges, clues for new possible applications have emerged. For example, for the in-plane superlens, we are aware of the possibility to use superlens waveguides to transfer the optical signal in a subwavelength scheme, which would be very useful in high-density photonic integrations[62]. The very recent example of a Weyl

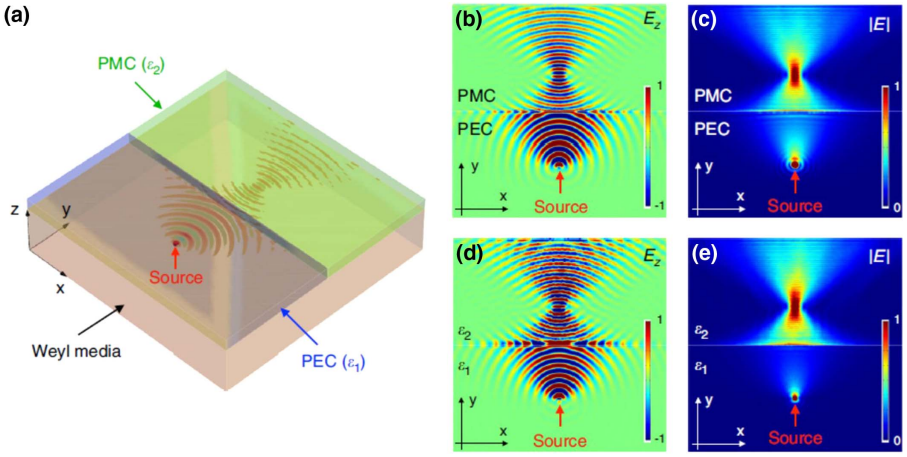

Fig. 10 Numerical confirmation of all-angle reflectionless negative refraction[63]. (a) Schematic configuration of all-angle negative refraction, where half of the top surface of the Weyl metamaterial is covered by a PEC layer, while the other half is covered by a PMC layer. A point source (electric dipole in z direction) is placed at the PEC/metamaterial interface. (b), (c) Imaging due to the AREN. The distributions of electric field Re(E_z) and magnitude $|E|$ at the frequency 25 GHz are plotted, respectively. (d), (e) Distributions of the electric field and the magnitude obtained by replacing the PEC and PMC layers with two different dielectric layers ($\varepsilon_1 = -10$ and $\varepsilon_2 = -0.01$), respectively.

metamaterial superlens also indicates a new platform for exploration of intriguing new physics in current photonic advances[63].

3 Metasurfaces and Metalenses

3.1 Metasurfaces and Working Principle

As discussed in detail in the previous section, super-resolution imaging by a superlens/hyperlens in feasible application scenarios still faces great challenges, though the function has been demonstrated in very limited circumstances (e.g., in the near-field regime). Researchers have turned their sights to new schemes of meta-designs and imaging frameworks. Metasurfaces, as planar-structured metamaterials with lower transmission losses and easier fabrication, have attracted great attention due to their ability to arbitrarily manipulate EM waves in an ultra-compact form[22,72,73]. Many applications of metasurfaces have been demonstrated, including metalenses[23,74–76], holograms[77,78], absorbers[79,80], cloaking[23,81], etc. As a newly emerging technology, metalenses have great potential in miniaturized and functionalized imaging systems, and have attracted much attention from both academia and industry. Many functionalities enabled by the flexible design of metalenses have been demonstrated, indicating a new era for building multitudinous fascinating optical technologies[82–84]. In this part, we will first illustrate the working principles of metasurfaces and corresponding metalens designs. Then, the progress and challenges of metalenses with enhancement of typical performances are discussed, including correcting chromatic and monochromatic aberrations, improving efficiency, facilitating manufacturing. At the end of the section, we summarize this part with a roadmap for metalens development towards high-quality imaging applications.

When light is incident into a metasurface composed of subwavelength meta-atoms, there are abrupt changes in phase, polarization, or amplitude or a combination of these properties for light in a local dimension, which gives rise to powerful capabilities in rearranging the light wavefront and its propagations. Based on Fermat's principle, Federico Capasso's group derived the generalized Snell's law to describe the reflective and refractive behavior of light [see Fig. 11(a)] when impinging on the metasurface as[22]

$$\begin{cases} \sin\theta_{\mathrm{r}} - \sin\theta_{\mathrm{i}} = \frac{\lambda_0}{2\pi n_{\mathrm{i}}}\frac{\mathrm{d}\phi}{\mathrm{d}x}, \\ n_{\mathrm{t}}\sin\theta_{\mathrm{t}} - n_{\mathrm{i}}\sin\theta_{\mathrm{i}} = \frac{\lambda_0}{2\pi}\frac{\mathrm{d}\phi}{\mathrm{d}x}, \end{cases} \tag{8}$$

in which n_{i} and n_{t} are the refractive indices on the two sides of the interface, θ_{i}, θ_{r}, and θ_{t} are angles of incidence, reflection, and transmission, respectively, λ_0 is the designed wavelength, and $\mathrm{d}\phi/\mathrm{d}x$ is the introduced phase gradient along the interface. In addition, this can also be understood from the perspective of the conservation of momentum in the direction parallel to the interface, where $\mathrm{d}\phi/\mathrm{d}x$ is equivalent to a valid wave vector. By elaborately tailoring the gradient of phase discontinuity along the interface, one can fully steer light with anomalous reflection and refraction. Gradient-index metasurfaces can also behave as a bridge linking propagating waves and surface waves. Lei Zhou's group from Fudan University theoretically and experimentally demonstrated a conversion from a freely propagation wave to a surface wave with efficiency near 100%[85], and the findings pave the way for many following applications based on on-chip integrations.

According to the phase modulation mechanism, metasurfaces can be categorized into two types: resonant metasurfaces[22,85–87] and non-resonant metasurfaces[88–90]. The early studies of metasurfaces mainly focused on phase manipulation with plasmonic resonance[22,85,86]. For example, the implementation of the generalized Snell's law was accomplished with V-shaped gold nanoantennas[22] [see Fig. 11(b)]. This kind of V-shaped resonator supports two intrinsic modes as symmetric and antisymmetric, which can be excited by electric field components parallel and perpendicular to the symmetric axis, respectively. In the case of arbitrary polarization incidence, both antenna modes are excited yet have different amplitude and phase responses due to the distinctive resonance conditions. The hybrid mode results in two polarization states in the scattered field, corresponding to ordinary reflection/refraction occupying a large amount of energy and anomalous reflection/refraction with limited efficiency. Later, a metal–insulator–metal (MIM) structure consisting of a metallic nanoantenna array separated from a metallic ground film with a dielectric spacer[85] [see Fig. 11(c)] was proposed to improve efficiency. The gap–surface plasmon mode can be excited due to the strong coupling between the top and ground metallic planes and achieve a phase shift covering 0–2π. However, this kind of metasurface can work in only reflection mode.

To achieve high efficiency in transmission mode, several promising strategies have been proposed. For plasmonic metasurfaces, one is to introduce a pair of orthogonal gratings while the metallic meta-atoms are sandwiched in between to form a Fabry–Pérot-like resonance[91,92]. Due to the multi-reflection process, the linearly cross-polarized light transmission can be dramatically enhanced. The other method is the generalized Kerker condition with radiation based on the contribution of excited EM multipoles[93]. Pin Chieh Wu's group reported a hybrid plasmonic meta-atom featuring a toroidal-assisted generalized Huygens' source with state-of-the-art circular polarization conversion efficiency beyond 50%[94]. In more general cases, researchers have started to turn their sights from metal to dielectric. For instance, meta-atoms made of dielectric nanodiscs were found to support Mie resonances. By tailoring the dimensions of the nano-disc, electric and magnetic dipole moments can be excited and tuned to meet the Kerker condition to support a 2π phase shift and near-unity transmission, known as Huygens' metasurfaces[87] [see Fig. 11(d)]. Nevertheless, the working bandwidth of such a resonant metasurface is narrow due to modulation sensitivity to structural parameters. Also, the resonance mode coupling between neighboring nanodisks could be remarkable under large phase gradients, resulting in limited applications.

The nano-discs of the aforementioned Huygens' metasurface usually have thicknesses much smaller than the wavelength; when dielectric nanoposts have heights (h) comparable to the wavelength, they can be regarded as truncated waveguides[88,89] [see Fig. 11(e)]. In this case, the phase modulation is based on the propagation phase, which is a non-resonant phase modulation mechanism. By adjusting the cross sections of the nanoposts or the lattice periodicity, different effective propagation constants (n_{eff}) can be obtained to realize different phase shifts ($\phi = \frac{2\pi}{\lambda_0} n_{\mathrm{eff}} h$) with high transmittances. It was first proposed by Andrei Faraon's group, in which a metalens with a high NA and high efficiency was demonstrated utilizing Si nanofins with a large aspect ratio[88]. Generally, metasurfaces based on a propagation phase have a broader band of working wavelengths than

resonant ones, and the polarization sensitivity depends on the anisotropy of the nanofins' cross sections.

Another non-resonant phase modulation method is the geometric phase, also known as PB phase[95]. It was first investigated by Erez Hasman's group[96]. When circularly polarized light illuminates on a dipole antenna, the scattered light partially converts into opposite circular polarization with a phase shift related to the rotation angle. Afterwards, Shuang Zhang's group and other researchers systematically described the phase modulation mechanism, and since then, PB phase metasurfaces[90] [see Fig. 11(f)] have been widely utilized for various applications[97]. Specifically, for circularly polarized incidence $|\sigma\rangle$, the output electric field through an anisotropic nanopost can be expressed as[98]

$$E_t = \hat{t}(\varphi)|\sigma\rangle = \frac{t_o + t_e}{2}|\sigma\rangle + \frac{t_o - t_e}{2} e^{\mp i2\sigma\theta}|-\sigma\rangle, \tag{9}$$

in which θ is the azimuthal rotation angle of the nanopost, and t_o and t_e are complex transmission coefficients along the two main axes of the nanopost. The first term on the right side represents co-polarization light with the incidence, and the second term indicates cross-polarization light with an extra phase modulation of $\pm 2\sigma\theta$. The modulation efficiency for cross-polarization can be maximized when the nanopost acts as a half-wave plate, where the amplitude of the original polarization state $|\sigma\rangle$ equals zero [i.e., $(t_o + t_e)/2 = 0$]. Adjusting the rotation angle from 0 to π, the modulated phase shift can easily cover 0–2π with broadband performances.

Different from PB phase, which is regarded as a global effect for circular polarization light, Chen Chen *et al.* proposed a local phase manipulation for metasurfaces with planar chiral meta-atoms[99] [see Fig. 11(g)]. Planar chiral meta-atoms break the mirror symmetry and n-fold ($n > 2$) rotational symmetries, which induces the non-diagonal term of the electric polarizability tensor. The nonzero values of the cross components of polarizability further enable the diversified phase shifts for orthogonal circular polarization lights, in which no rotation of meta-atoms is needed. Furthermore, if these kinds of dielectric meta-atoms have wavelength-scale height, a propagation phase would also come into play, and the hybrid effect can break the fundamental symmetry restrictions of PB phase and easily

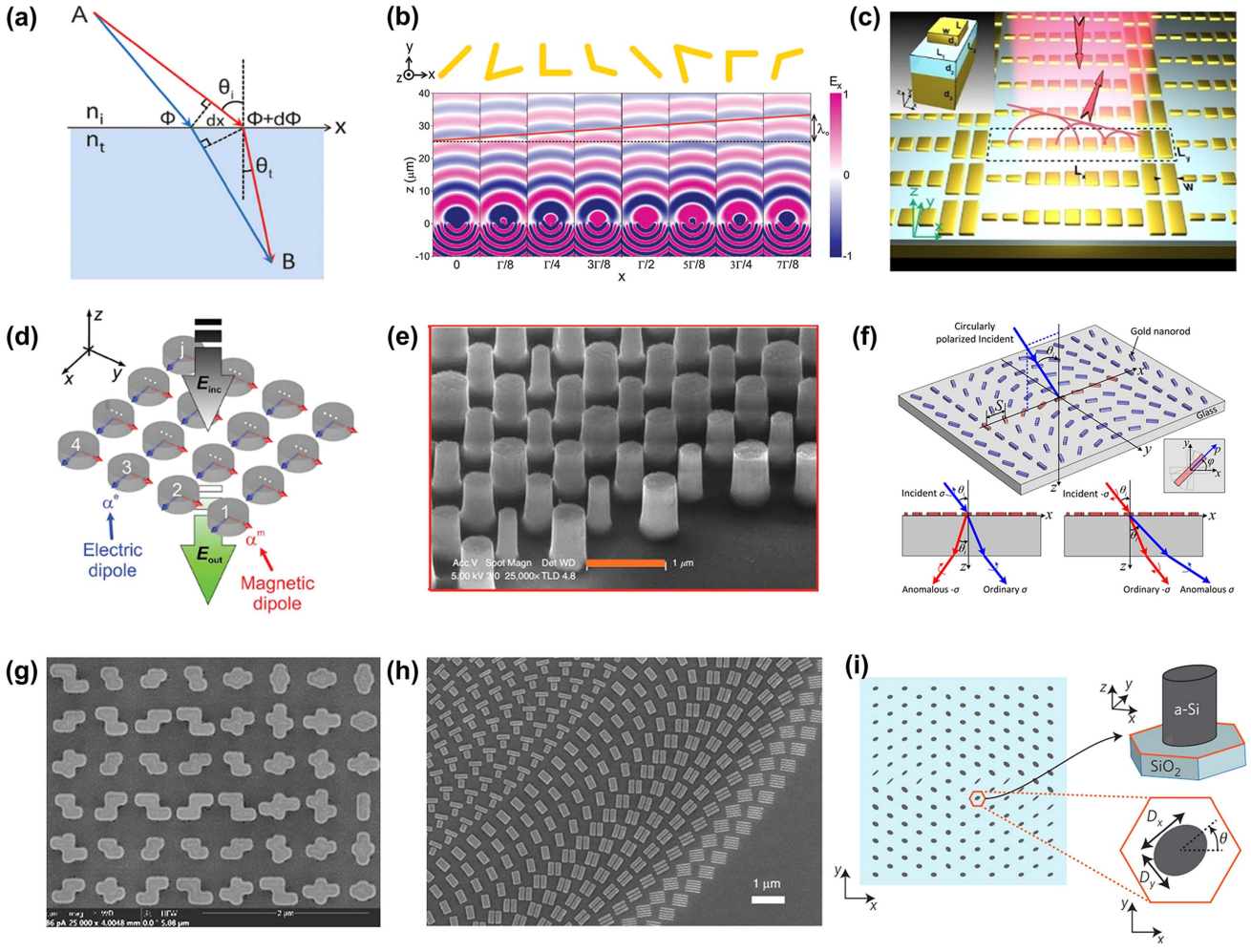

Fig. 11 Design principles of metasurfaces. (a) Schematics of the generalized Snell's law of refraction[22]. (b) Metasurface with V-shaped antenna array[22]. (c) Gap–plasma metasurface[85]. (d) Huygens metasurface[87]. (e) Propagation phase metasurface[88]. (f) PB phase metasurface[90]. (g) Metasurface with planar chiral meta-atoms[99]. (h) Metasurface with combination of resonant phase and PB phase[26]. (i) Metasurface with combination of propagation phase and PB phase[89].

realize the independent functionalities of circular polarization lights. As indicated by the metasurfaces with planar chiral meta-atoms, different phase modulation methods work in a joint mode with extended degrees of freedom (DoFs) for implementation of more complex functions and better performances[22,26,27,100,101].

As early as 2011, the PB phase was combined with a resonance phase to extend the phase delay range of V-shaped antenna arrays from π to 2π[22] [see Fig. 11(b)]. Dispersion modulation of the metalens was also demonstrated when integrating the resonant phase and PB phase[26] [see Fig. 11(h)], which will be discussed later. The aspect ratios of nanoposts can be reduced as well to ease the fabrication with the combination of PB phase and Huygens' metasurface[100]. The propagation phase and PB phase are also merged for the independent phase modulation of orthogonal polarizations[89] [see Fig. 11(i)].

3.2 Metalenses for Achromatic Imaging

Based on the working principles of metasurfaces, a metalens can be constructed with a focusing phase profile as[102]

$$\varphi(R) = \frac{2\pi}{\lambda}\left(f - \sqrt{R^2 + f^2}\right), \tag{10}$$

where f is the focal length, and R is the radial position from the center. Unlike the refractive lens that possesses a continuous phase distribution, a metalens is imparted with discrete phase levels (0–2π) by locally designed meta-atoms. Increasing the number of phase discretization levels, the envelope wavefront will be closer to the ideal spherical wavefront, but with more challenges in fabrication. In general cases, no fewer than four levels of phase discretization are required to meet the Marèchal criterion for negligible aberrations[103,104]. On the other hand, the period of the meta-atom unit cell (p) should be sub-wavelength to avoid high orders of diffraction and satisfy the Nyquist sampling criterion $p < \frac{\lambda}{2\mathrm{NA}}$, in which NA is the maxinum NA for focusing or imaging[105].

The historical development of metalenses in the early years is closely related to that of metasurfaces. Plasmonic materials were widely used for the construction of metalenses early on[102,106]; however, large intrinsic losses hinder metalens performance and limit efficiency to at most 25%[107]. Now the dielectric has become the mainstream material choice for higher efficiency. In 2016, Federico Capasso's group proposed a metalens constructed by titanium dioxide (TiO_2) nanofins with a diameter of 2 mm and focal length of 0.725 mm[23] (see Fig. 12). With diffraction-limited focusing and high efficiencies at RGB wavelengths (86% for $\lambda = 405$ nm, 73% for $\lambda = 532$ nm, 66% for $\lambda = 660$ nm), this metalens is comparable to commercial lenses at a single wavelength. Since then, continuous efforts have been made for implementation of metalenses and improvement of performances towards high-quality imaging in different working bands[108–112]. Overall, the high refractive index and low absorption coefficient are two key factors for the material choice of metalenses. In the visible band, besides TiO_2, gallium nitride (GaN) and silicon nitride (SiN_x) are also widely selected. Hafnium oxide (HfO_2) and aluminum nitride (AlN) are generally chosen for the UV band. Cheng Zhang *et al.* designed and fabricated a HfO_2 metalens with NA = 0.6 and efficiency of nearly 55%[108]. In the infrared band, germanium (Ge) and silicon (Si) are the most suitable choices, for example, Qingbin Fan *et al.* demonstrated a linear-polarization multiplexing Si metalens at $\lambda = 10.6$ μm with efficiency of about 72%[109].

As can be found in Fig. 12, images obtained by the same metalens at different wavelengths have different magnifications. More severely, the quality of the image degrades with the broadening illumination bandwidth, which is due to the effect of chromatic aberration. Inheriting diffraction dispersion[113], metalenses usually have larger chromaticity than bulky refractive lenses, which significantly limits imaging applications. To address this issue, multi-wavelength achromatic metalenses with different strategies have been demonstrated[114–117]. Avayu *et al.* designed a multilayer structure by vertically stacking metalenses constructed with different plasmonic materials for multispectral achromatic focusing in the visible band (450 nm, 550 nm, and 650 nm)[114] [see Fig. 13(a)]. Due to the optical loss of metal materials, the efficiency of the metalens is lower than 10%. Besides cascading lenses vertically, spatial multiplexing in-plane is also a popular approach to correct chromatic aberrations at discrete wavelengths. Specifically designed metalenses at different operational wavelengths are interleaved together to provide the same focal length, as shown in Fig. 13(b) for RGB achromatism[115]. This method is straightforward yet has low efficiency and serious cross talk. Polarization can also be utilized as a DoF for encoding phase requirements to realize multi-wavelength achromatic metalenses. Ehsan Arbabi *et al.* proposed a double-wavelength (822 nm and 600 nm) metalens for two-photon microscopy with two orthogonal linear polarization multiplexings[116] [see Fig. 13(c)]. In addition, coupled dielectric nanoresonators with an aperiodic arrangement can also be utilized to compensate for phase dispersion at discrete wavelengths (1300 nm, 1550 nm, and 1800 nm), as shown in Fig. 13(d)[117]. It is worth mentioning that most multi-wavelength achromatic metalenses can operate only under discrete wavelength illumination. For broadband illumination, there are remarkable background noises arising from the light with unwanted wavelengths, which severely degrades achromatic imaging performance[31]. To solve this problem, Tao Li's group incorporated a well-designed bandpass filter into an RGB achromatic metalens optimized by the Hooke–Jeeves algorithm, as illustrated in Fig. 13(e)[118]. An obvious improvement has been made in the signal-to-noise ratio (SNR) and imaging performance under white light illumination, by comparing it with a controlled sample without a filter, indicating the advantages in integrated imaging systems.

In general cases, multi-wavelength achromatism is not sufficient for full-color imaging, and broadband achromatic metalenses are in high demand and attract great attention in both academia and industry. Normally, considering a bandwidth around ω_d, the frequency-dependent phase profile can be expressed as a Taylor series expansion[27]:

$$\varphi(R,\omega) = \varphi(R,\omega_\mathrm{d}) + \left.\frac{\partial\varphi(R,\omega)}{\partial\omega}\right|_{\omega=\omega_\mathrm{d}}(\omega-\omega_\mathrm{d}) + \left.\frac{\partial^2\varphi(R,\omega)}{2\partial\omega^2}\right|_{\omega=\omega_\mathrm{d}}(\omega-\omega_\mathrm{d})^2 + \ldots. \tag{11}$$

The first term on the right side represents the relative phase for a spherical wavefront at the central target frequency. The second and third terms indicate the group delay and group delay dispersion, respectively. To correct chromatic aberrations, the

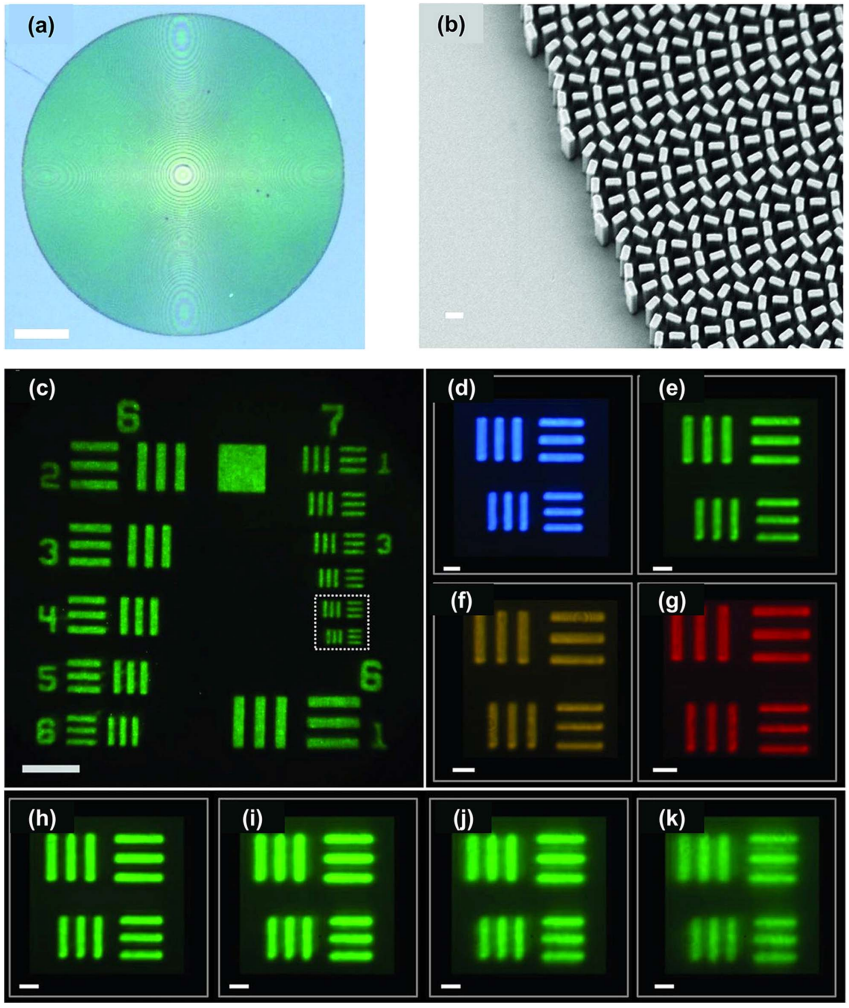

Fig. 12 TiO_2 metalens[23]. (a) Optical image of the metalens. Scale bar: 40 μm. (b) SEM micrograph of the fabricated metalens. Scale bar: 300 nm. (c) Image of 1951 USAF resolution test chart formed by the metalens at 530 nm. Scale bar: 40 μm. Images of the highlighted region in (c) at wavelengths of (d) 480 nm, (e) 530 nm, (f) 590 nm, and (g) 620 nm. Images of the highlighted region in (c) at a center wavelength of 530 nm and with different bandwidths: (h) 10 nm, (i) 30 nm, (j) 50 nm, and (k) 100 nm. Scale bar: 5 μm.

group delay ought to vary as the frequency departs from ω_d to compensate for the difference in wave packet arrival times at the focus, and the group delay dispersion guarantees identical outgoing wave packets. For the hyperbolic phase profile [see Eq. (10)], the group delay is the main factor to obtain achromatic imaging. Mohammadreza Khorasaninejad *et al.* achieved a reflective achromatic focusing at green wavelengths (490 nm to 550 nm) with a diameter of 200 μm and NA of 0.2 through optimizations[119]. Ehsan Arbabi *et al.* also demonstrated an achromatic metalens with an operation bandwidth from 1450 nm to 1590 nm with a diameter of 500 μm and NA of 0.28 in a similar way[120].

Afterwards, Shuming Wang *et al.* developed a new strategy to realize broadband achromaticity that divides the focusing phase [Eq. (10)] into two parts including the reference phase $\varphi(R, \lambda_{max})$ determined by the geometric phase, and the phase difference between other wavelengths and this reference, which writes $\Delta\varphi(R,\lambda) = -[2\pi(\sqrt{R^2+f^2}-f)](\frac{1}{\lambda}-\frac{1}{\lambda_{max}})$. This wavelength-dependent phase compensation for $\Delta\varphi(R, \lambda)$ can be fulfilled by so-called integrated resonances from particularly designed versatile meta-atoms with linear phase dispersion to $1/\lambda$. For a proof-of-concept experiment, the working wavelength is chosen within the near-infrared region (1200–1680 nm), and metallic nano-rods and their assemblies are selected as the basic building blocks with a metal–dielectric–metal structural configuration to enhance the operating efficiency[26]. As shown in Fig. 14(a), this kind of metalens works in reflection mode and has a relatively small size with a diameter of 55.55 μm and NA = 0.217. Thereafter, the same group realized a transmission achromatic metalens in the visible (400–660 nm). This metalens is constructed by geometric phase and propagation phase (regarded as guided mode resonances), in which wavelength-dependent phase modulation is tailored through solid and inverse GaN nanoposts. Nearly at the same time, Wei Ting Chen *et al.* also demonstrated a broadband achromatic metalens for focusing and imaging in the visible (470–670 nm) with coupled TiO_2 nanofins, as shown in Fig. 14(b)[27].

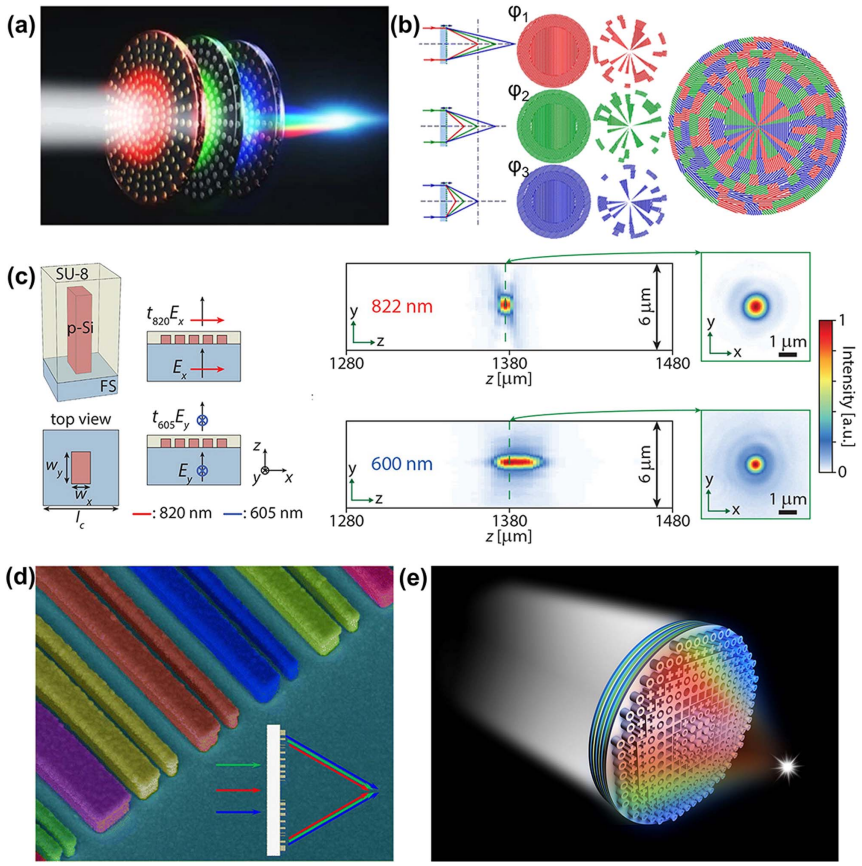

Fig. 13 Multi-wavelength achromatic metalenses. (a) Multispectral achromatic metalens with stacked layers[114]. (b) Spatial segmented achromatic metalens at RGB wavelengths[115]. (c) Dual-wavelength achromatic metalens with polarization manipulation[116]. (d) Achromatic metalens based on waveguide resonance[117]. (e) Bandpass-filter-integrated multiwavelength achromatic metalens[118].

However, the aforementioned broadband achromatic metalenses are both polarization sensitive due to the PB phase design and have limited apertures. To address the polarization sensitivity, researchers have provided more geometric DoFs with the reference phase also achieved by propagation phase[29,121–123]. Sajan Shrestha *et al.* achieved an achromatic polarization-insensitive metalens across the bandwidth from 1200 nm to 1650 nm[29]. The proposed nanostructures have complex shapes with fourfold symmetry to provide enough parameter space with phase and dispersion [see Fig. 14(c)]. Zhi-Bin Fan *et al.* also demonstrated a polarization-insensitive silicon nitride metalens with an effective achromatic refractive index distribution from 430 nm to 780 nm[121].The diameter of the achromatic metalens is 14 μm with a measured focal length of about 81.5 μm, yielding an experimental NA of 0.086.

Reviewing the reported results on achromatic metalenses, it is not difficult to find that there is a trade-off among the bandwidth, diameter, and NA of achromatic metalenses from previous works, and therefore the fundamental bounds for achromatic imaging are further investigated. Figure 15(a) shows previously published achromatic metalens designs against the bandwidth limits reported in 2020[30]. The lower solid blue curve indicates the upper bound for ideal metalenses with no aberrations. From the view of time–bandwidth products, this limit can be derived as

$$\Delta\omega \le \Delta\omega_{\max} = \frac{\kappa c}{\left(\sqrt{f^2+R^2}-f\right)} = \frac{\kappa c\sqrt{1-(\mathrm{NA}/n_\mathrm{b})^2}}{f\left[1-\sqrt{1-(\mathrm{NA}/n_\mathrm{b})^2}\right]}, \tag{12}$$

in which n_b is the background refractive index, and κ is a dimensionless quantity dependent on the meta-atoms' properties. With the increase in radius (R) and NA of the metalens, the achievable achromatic bandwidth will shrink ($\Delta\omega_\mathrm{d}$). Considering a metalens with required R and NA, the way to broaden the bandwidth is to enlarge κ. For a resonant-type metasurface with deep subwavelength thickness, coupled-mode theory provides a geometry- and material-independent value ($\kappa = 2$) for a single resonator, which severely limits the bandwidth of achromatism. Meta-atoms with multiple resonances are not expected to significantly improve the value of κ either[124]. For non-resonant metasurfaces with inclusions acting as truncated waveguides, Tucker *et al.* derived the value of the upper bond κ as[125]

$$\kappa = \frac{\omega_\mathrm{d} h}{c}(n_{\max} - n_{\min}), \tag{13}$$

where $n_{\max}$ and $n_{\min}$ are the maximum and minimun effective refractive indices, respectively, and h is the thickness of the

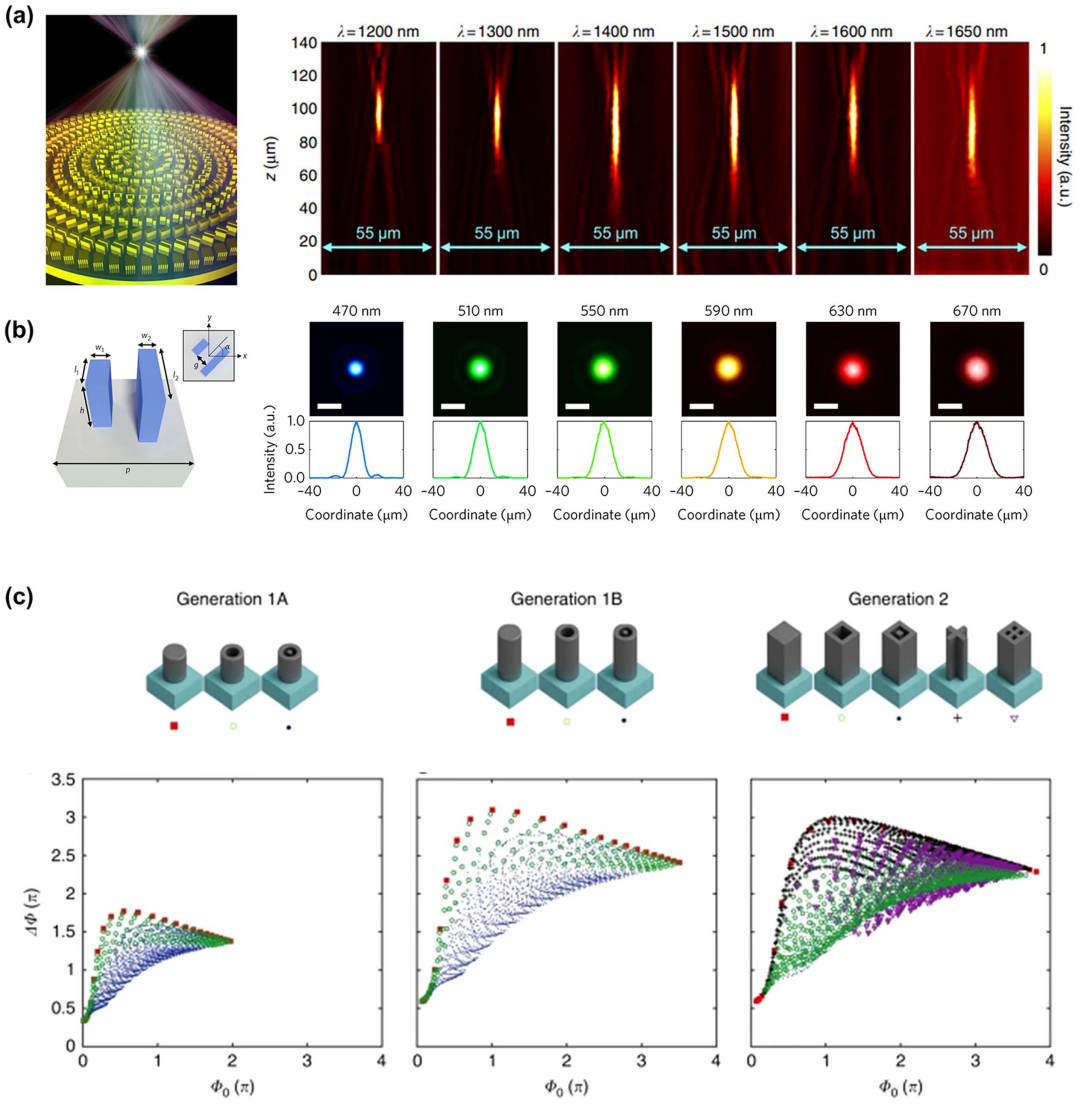

Fig. 14 Broadband achromatic metalenses. (a) Achromatic metalens in reflection mode with a bandwidth from 1200 nm to 1650 nm, $D = 55.55$ μm, and NA = 0.217, working under circular polarizations[26]. (b) Achromatic metalens in transmission mode in the visible band (470–670 nm), $D = 25$ μm, and NA = 0.2, working under circular polarizations[27]. (c) Meta-atoms of polarization-insensitive achromatic metalens in the near-infrared region[29].

meta-atoms. For more generic cases (not necessarily dielectric) of larger thicknesses, there is

$$\kappa = \frac{\omega_d h}{2\sqrt{3}c}|(n_{max}^2 - n_b^2)/n_b^2|, \tag{14}$$

where n_b is the refractive index of the background. These equations provide us with some clues to extend the structual dispersion, that is, increasing the refractive index constrast and thickness of meta-atoms. For example, Shuming Xiao's group fabricated TiO_2 nanopillars with a height of 1.5 μm to achieve achromatism [see Fig. 15(b)][126]. The developed metalens operates in the wavelength range of 650–1000 nm with efficiency of 77.1%–88.5% and NA of 0.24–0.1, which is a very high efficiency among reported achromatic metalenses. The extended broad bandwidth ensures applications in biological imaging. However, this highly efficient achromatic metalens is still very small in diameter (<30 μm), undoubtedly limiting its application. To enlarge the lens size, its thickness needs to further increase (i.e., heights of the meta-atoms of nanoposts), which would pose a great fabrication challenge due to the high aspect ratio, though the authors have claimed they have achieved a record high aspect ratio of 37.5 in this work. In this regard, how to access extremely large aspect ratio nanoposts for phase compensation in achromatic metalens designs on large scales is still a big challenge to date.

In addition to the thickness increase with a single-layer metalens, layered structures could possibly surpass the aforementioned bounds in non-ideal cases. Figure 15(c) illustrates a unit structure of a merged hybrid achromatic metalens consisting of a phase plate and nanopillars[127]. Combining recursive ray-tracing and phase libraries, the metalens has an average focusing efficiency greater than 60% over a broad band from 1 μm to 1.8 μm. With manipulation of the effective Abbe number,

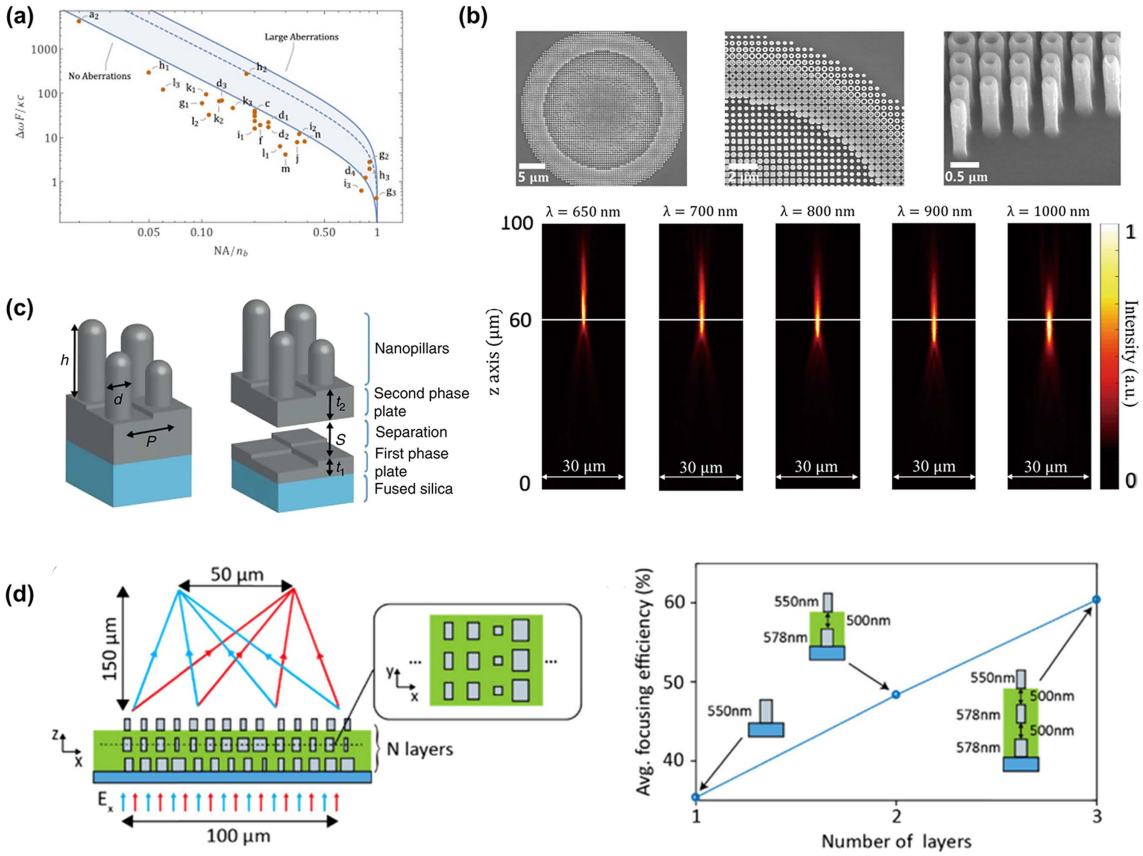

Fig. 15 Fundamental bound of the achromatic metalens[30]. (a) Solutions to extend or break the limits. (b) TiO_2 nanopillars with height of 1.5 μm to achieve achromatism from 650 nm to 1000 nm[126]. (c) Hybrid achromatic metalens with broadband from 1 μm to 1.8 μm[127]. (d) 2.5D metalens with efficiency enhancement[129].

Mengmeng Li *et al.* also proposed a dual-layer achromatic metalens with average efficiency of 42% in the visible (400–700 nm)[128]. Mahdad Mansouree *et al.* proposed the concept of a 2.5D metasurface composed of multilayer metasurfaces[129]. An adjoint optimization technique is utilized to design metastructures with nonlocal interactions. As shown in Fig. 15(d), the efficiency of the meta-device can be increased with the number of layers, which might be promising for achromatic metalens design in the future[130,131].

3.3 Metalenses for Wide-field Imaging

Besides chromatic aberrations, monochromatic aberration is another important issue degrading imaging performance, which includes spherical aberration, coma aberration, astigmatism, field curvature, and distortion. For a metalens with a well-designed hyperbolic phase profile, there are no spherial aberrations at normal incidence. For a point source, especially in a microscopy case, light rays will no longer converge at the same point, resulting in the decrease in resolution in both transverse and longitudinal directions. Thus, the phase profile should be redesigned to remove spherical aberrations for high resolution[132]. Also, off-axis aberrations increase as the incident angle θ increases, especially the coma aberration. Nonnegligible aberrations undoubtedly affect the FOV of metalenses and limit applications such as landscape imaging and microscopy.

The ideal phase profile for a metalens free of both spherical and coma aberrations simultaneously is expressed as[133]

$$\varphi(r,\lambda,\theta) = -\frac{2\pi}{\lambda}\left[r\sin\theta + \sqrt{(r - f\tan\theta)^2 + f^2} - \frac{f}{\cos\theta}\right]. \tag{15}$$

It is a function of incident angle, which requires an angle-dispersion phase for meta-atoms. However, the phase delays of different types of meta-atoms are generally angle independent, which poses challenges in achieving wide-angle imaging of high quality. Recently, several types of metalens configurations have been proposed for wide-angle imaging[134], including metalens doublets[25,135], optimized multi-parametric geometries[136,137], monolayer quadratic metalenses[138], air-gapped landscape quadratic metalenses[139], and dielectric-gapped landscape quadratic metalenses[140]. The schematic of metalens doublets is shown in Fig. 16(a), in which the first metasurface is encoded with a phase profile similar to a Schmidt plate and results in converging chief rays and diverging marginal rays[25]. The other metasurface is imparted with a focusing phase profile, which has a stronger phase gradient at the edge than the hyperbolic phase. Andrei Faraon's group realized a metalens doublet with a small f-number of 0.9, viewing angle larger than 60° × 60°, and operating at 850 nm wavelength with 70% focusing efficiency[25]. Subsequently, Federico Capasso's

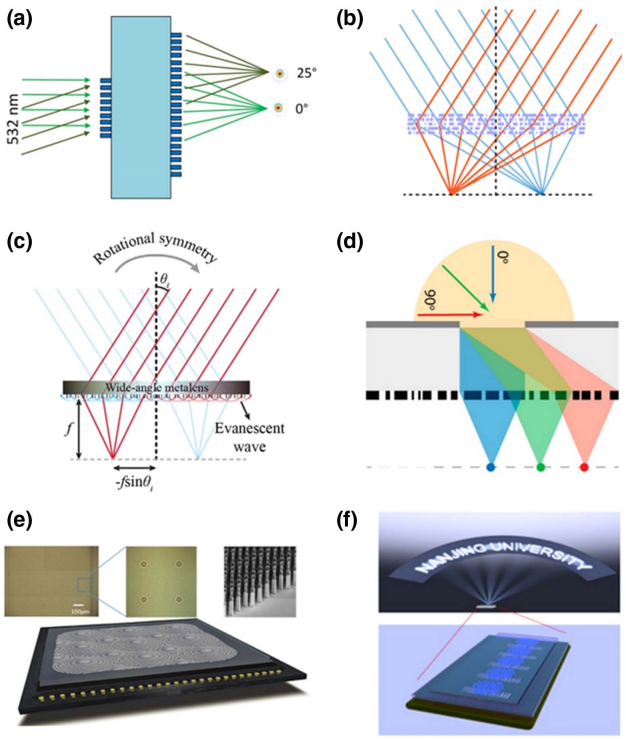

Fig. 16 (a) Metalens doublet[25]. (b) Optimized multi-parametric geometries[134]. (c) Monolayer quadratic metalens[141]. (d) Double-layer metalens incorporated with a quadratic metalens and an aperture stop[138]. (e) Extended FOV for microscopy with a metalens array[142]. (f) Wide-angle-imaging camera enabled by a metalens array[143].

group fabricated a metalens doublet with NA of 0.44, focal length of 342.5 μm, and viewing angle of 50°, which enables diffraction-limited monochromatic imaging at a wavelength of 532 nm[135]. Multilayer topological optimization is designed to improve DoFs for angular phase control, as shown in Fig. 16(b)[134]. Zin Lin *et al.* proposed a topology-optimization framework for inverse design of multilayered wide-angle metalenses with an effective NA of 0.35 and viewing angle of 40°[136]. Chenglong Hao *et al.* optimized the multistep flat lens with an epsilon-greedy algorithm and demonstrated that the lens has an effective NA of 0.45 and viewing angle of 32° at the wavelength of 633 nm[137]. The other three types are all based on quadratic phase designs. This kind of quadratic metalens transforms the rotational symmetry of obliquely incident light to the translational symmetry of the focusing beam, as shown in the following:

$$\varphi(r,\theta) = -\frac{k_0}{2f}r^2 - k_0 x \sin\theta = -\frac{k_0}{2f}[(x + f\sin\theta)^2 + y^2] + \frac{k_0 f \sin^2\theta}{2}, \quad (16)$$

in which $kx \sin\theta$ is the gradient phase introduced by oblique incidence. Light with an incident angle θ converges to the designed focal plane with an offset of $-f \sin\theta$ [see Fig. 16(c)]. Fourier analysis and imaging properties were further analyzed and indicated a reduction in the effective aperture and barrel distortion[141]. In addition, the spherical aberration of the quadratic metalens becomes obvious and results in strong background noise. To address the issue, an aperture stop can be incorporated with the quadratic metalens to minimize the aberrations, which is similar to the classical Chevalier landscape lens [see Fig. 16(d)][138]. The aperture stop can be placed in front of the metalens with an air gap d, while supporting only a diffraction-limited FOV due to the mismatch of the actual position $(-d \tan\theta)$ and ideal position $(-f \sin\theta)$[139]. If the aperture stop is placed with a high-index ($n > 1$) material gap with optimized thickness, the FOV can be significantly enhanced with a record FOV of 178° × 178°. As the diameter of the aperture stop decreases, the imparted phase is closer to the hyperbolic phase, while the aperture becomes smaller.

Another strategy to achieve wide-field or wide-angle imaging is constructing a metalens array. For instance, Tao Li's group developed a metalens array with a polarization-multiplexed dual-phase design for wide-field microscope imaging[142] [see Fig. 16(e)]. This method expands the FOV without sacrificing resolution and promises a non-limited space–bandwidth product for wide-field microscopy. Ji Chen *et al.* proposed a metalens array for wide-angle imaging in a similar way[143] [see Fig. 16(f)]. Each metalens is introduced with a phase term related to different incident angles to minimize distortion and aberrations. A range of >120° imaging is demonstrated and indicates the advantages of metalens arrays for miniature and high-quality imaging. It should be noted that in conventional single-axis optical settings, the FOV has a rigid correspondence to the view of angle (VOA); however, in the lens array system with multiple optical axes, they are quite different. For example, in Ref. [142], the large FOV is composed of multiple equally-sized images, while its VOA is not extended in the microscope system. Therefore, it is an equivalent expansion of the FOV.

With the angle of modulated light rays increasing, efficiency generally decreases. The same situation happens when adding functionalities. Thus, improving the efficiency of metalenses with high NAs or multifunctions is in high demand. Much attention has been paid to address the efficiency issue[144–147]. For example, Ramón Paniagua-Domínguez *et al.* demonstrated a metalens with near-unity NA, which is composed of an array of asymmetric dimers producing energy concentration into the T_{+1} diffraction order [see Fig. 17(a)]. The measured diffraction efficiency is about 35% with the light bending at 82° at normal incidence[144]. In addition to optimization of the unit cell, Federico Capasso's group proposed a modified design technique that allows the pillars to be at arbitrary locations, but repeats the pattern of pillars every 2π period of the phase [bottom part of Fig. 17(b)]. A metalens with a diameter of 1 mm and focal length of 200 μm was demonstrated with focusing efficiency of about 79%[145]. With a fabrication-related constraint, this kind of metalens can also be fabricated by one-step deep-UV (DUV) photolithography, which is more scalable than typical electron-beam lithography. Andrea Alù's group proposed a hybrid metalens constructed by a gradient metasurface located in the center of the lens and a metagrating on the edge. The reported metalens offers a measured efficiency of 0.479 with NA of 0.98 [see Fig. 17(c)][146]. An aperiodic metasurface based on a grating averaging technique was also proposed for increasing the efficiency of the metalens with high NA. As shown in Fig. 17(d), meta-atoms vary rapidly between unit cells but slowly between extended cells. Thus, the extended cell can be approximately considered as a period of a blazed grating, which shows great advanteges in efficiency compared with

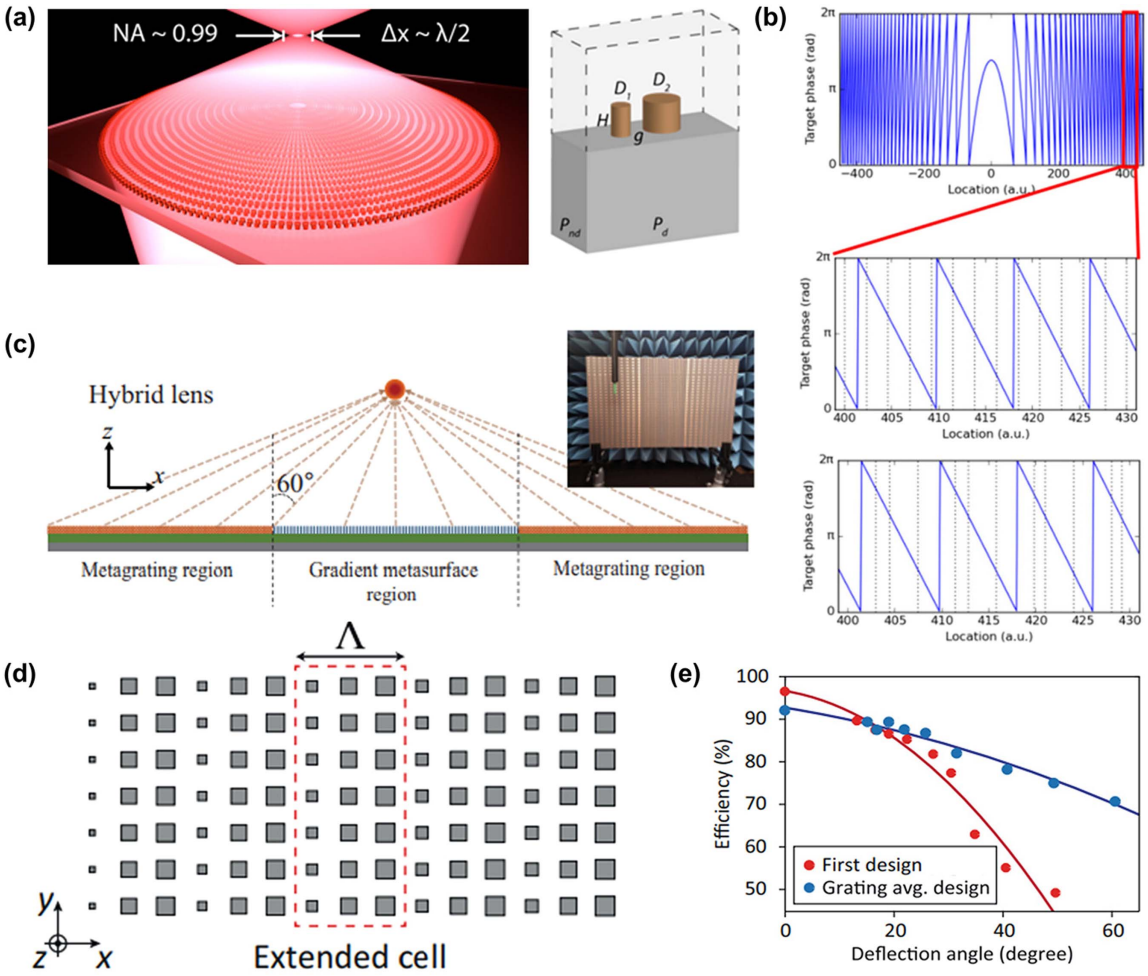

Fig. 17 (a) Metalens with NA = 0.99 and corresponding unit cell of the asymmetric dimers[144]. (b) Modified design method for high-NA and high-efficiency metalens design[145]. (c) Hybrid lens with gradient metasurface and metagrating[146]. (d) Extended cell design for high-NA optics and (e) its efficiency advantages over classical periodic metasurface design[147].

classical periodic metasurfaces [see Fig. 17(e)][147]. A metalens with NA of 0.78 and a focusing efficiency of 77% was demonstrated and indicated the potential applications in implementing high-NA devices.

As mentioned above, most phase responses of dielectric meta-atoms (not including supercells or superpixels[148]) are angle independent under some conditions [e.g., in small incident angle regions (<30°), where no other mode is excited[149]], while the phase profile for an ideal metalens free of monochromatic aberrations needs to vary with incident angles. Thus, the manipulation of angular dispersion is also of importance for realizing better imaging performance and is suggested to be given more attention. For terahertz metasurfaces, Lei Zhou's group showed that the plasmonic couplings among meta-atoms dictate angular dispersion and established a theory to quantitatively describe it. They proposed a more general and systematic strategy to guide the design of optical metasurfaces with fully controlled angular dispersions. Besides the near-field couplings between meta-atoms, the radiation pattern of a single constituent meta-atom also contributes to angular dispersion[150]. Different angle-dependent meta-devices (e.g. incident-angle-selective absorbers) in the near-infrared regime were demonstrated for proof of concept. However, the realization of an ideal metalens with the required angular dispersion still remains challenging.

3.4 Metalenses for Super-resolution Imaging

As discussed above, a superlens or hyperlens, although with the ability to overcome the diffraction limit, suffers from the complexity of near-field optical manipulations, while with the optical super-oscillatory phenomenon, lens focusing can go beyond the diffraction limit in the far field. Super-oscillation arises from the delicate interference of light generated from specifically designed structures, which forms a mask with spatially varying absorption and retardance[82,151]. Due to the fragility of the super-oscillatory light field, the super-resolution lens usually suffers from a very narrow working wavelength band. To address this issue, Xiangang Luo's group utilized the PB-phase-based metasurface to achieve ultra-broadband super-resolution. The phase profile is a combination of a hyperbolic phase and an extra binary phase that is optimized to achieve super-resolution, as shown in Fig. 18(a), in which sample A is the normal metalens while B and C are optimized metalenses. The final focal FWHMs are 0.843 and 0.674 times the spot size of the Abbe

diffraction limit, respectively. The focal patterns show similar optical-field distributions and retain super-resolution except for the chromatic focus shift and the change in focusing intensity[152]. To overcome the chromatic aberration, Nikolay I Zheludev's group optimized the amplitude or phase mask with a multi-objective particle swarm optimization algorithm to generate several discrete foci. For different wavelengths, the designed super-oscillatory lens can be regarded as achromatic or apochromatic if the foci of two or three wavelengths can overlap each other[153]. A white-light super-oscillation imaging system was also demonstrated with the combination of a metasurface filter and a normal achromatic refractive lens. The proposed metasurface filter is based on PB phase and has optimized positions with perfect zero and π phase-only manipulation. Resolving ability of about 0.64 times the Rayleigh criterion (RC) is obtained for wavelengths ranging from 400 nm to 700 nm. Figure 18(b) shows comparisons of imaging results with a normal lens (middle) and a super-oscillatory lens (right)[154]. Despite the considerable achievements[155], realization of a compact achromatic super-oscillatory metalens with high efficiency still faces challenges due to the complicated light field.

As an alternative method, a supercritical lens (SCL) was proposed as a trade-off between resolution and other performances, such as energy proportion and working distance. As shown in Fig. 18(c), by RC and a super-oscillation criterion (SOC), focal spots with possible intensity patterns can be categorized into three regions[156]. From the range of above-resolution to super-oscillation, the size of the main lobe decreases smoothly with gradually increased sidelobes. Fei Qin *et al.* demonstrated SCL composed of a series of concentric transparent belts at 405 nm. A pattern with a minimal feature size of 65 nm can be recognized, and the working distance is up to 55 μm, nearly one order improvement compared to previously reported super-oscillatory lenses. Figure 18(c) also shows the image of a

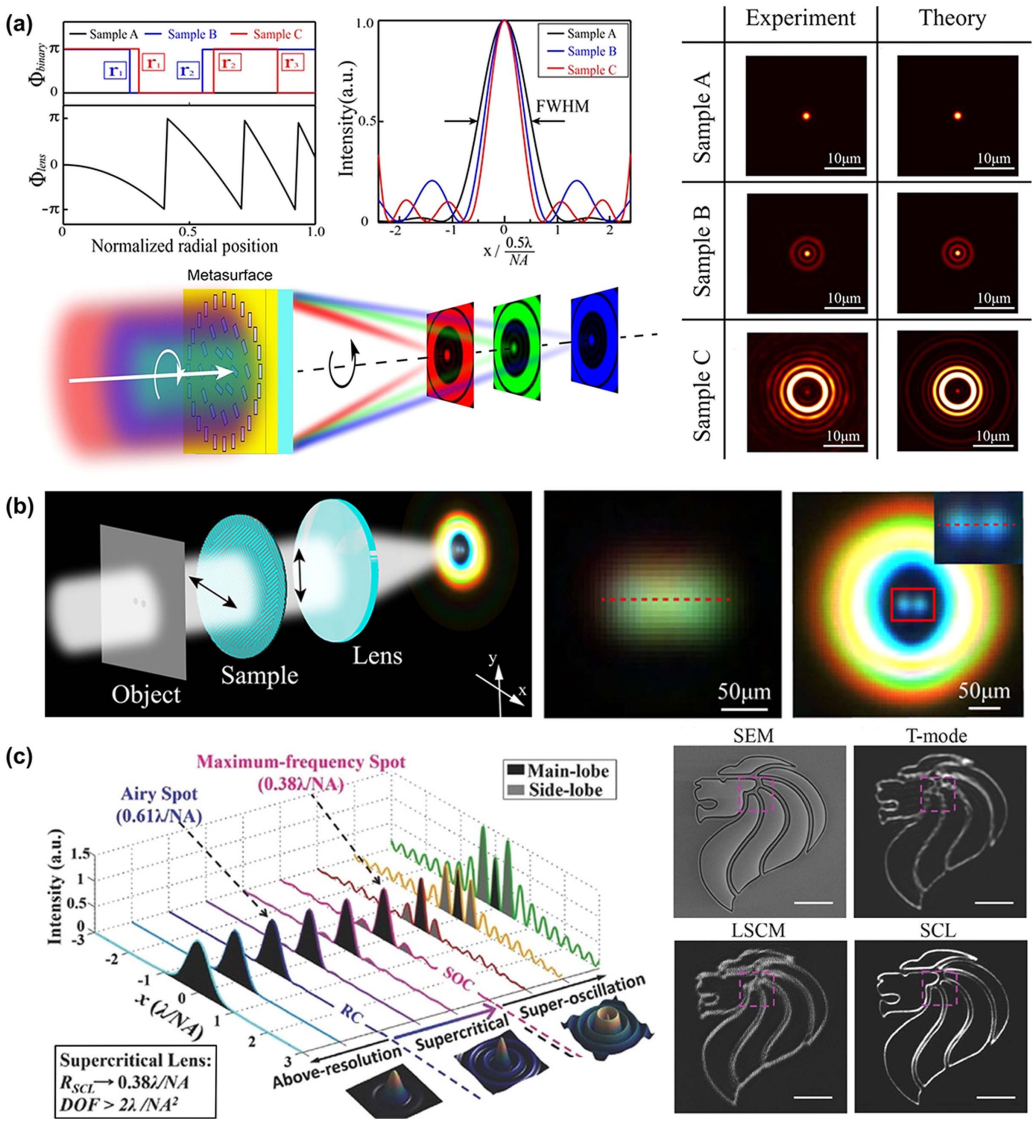

Fig. 18 (a) Ultra-broadband super-oscillatory metalens with sub-diffraction light focusing with focal shift due to dispersion[152]. (b) Achromatic broadband super-resolution imaging with a combination of the metasurface filter and achromatic lens[154]. (c) Supercritical lens with sub-diffraction resolution and corresponding comparison imaging results[156].

large-scale non-periodic pattern (13.5 μm × 13.5 μm) and the comparison imaging results with scanning electron microscopy (SEM), transmission mode microscopy (T-mode), and laser scanning confocal microscopy (LSCM), indicating sub-diffraction resolution. It should be noted that this kind of super-resolution imaging is based on the scanning process, which is quite different from the superlens/hyperlens imaging as mentioned in Section 2, since it cannot directly recover information from the evanescent wave of objects.

3.5 Computation-empowered Metalens Imaging

Recently, inverse design and artificial intelligence (AI) algorithms have developed rapidly in various fields and also play vital roles in the design and optimization of meta-devices. As the requirements for performances and functions of meta-devices increase, the construction of meta-atoms with common physical models is insufficient to meet the demand. Inverse design methods were gradually introduced to search for proper parameters of a metasurface to exhibit the desired functions. Here, inverse design is an algorithmic technique for discovering optical structures (such as height distribution) based on desired functional characteristics. Compared to conventional design methods, where the phase profile is fixed everywhere on the lens surface (such as a parabolic or hyperbolic phase profile), inverse design is more flexible and thus can generate lenses with more functionalities. The design goal of inverse design is usually set as finding the maximum (or minimum) of an objective function [also called figure of merit (FoM)] under some constraints. Different optimization strategies or a combination has been reported for different problems[157–159]. Among them, topology optimization is an efficient technique for handling extensive design spaces, which considers the modulation of dielectric permittivity at every spatial point[160]. Through penalization and filter projection methods[161], one can further obtain a binary structure. Zin Lin *et al.* proposed a general topology-optimization framework for metasurface inverse design that can discover highly complex multilayered structures[136]. A multilayered 2D metalens with aberration corrected under incident angles of 0°, 7.5°, 15°, and 20° was demonstrated for proof of cencept [see Fig. 19(a)]. However, the optimized metalens has a small size (23λ) due to limited computation sources. To achieve a metalens with a large area and high efficiency, Jonathan A. Fan's group divided the desired phase profile into linear sections with wavelength scale and utilized topology optimization to design each section individually [left part in Fig. 19(b)][162]. This method can obviouly save computation time compared with the optimization of a full device. The efficiency of a metalens with high NA can also be enhanced, as shown in the right part of Fig. 19(b). With fabrication technology improving, inverse design methods will enable metalenses with more complex functions and better performances.

Intelligent methods also help in metalens design and aberration correction. For instance, Ethan Tsenga *et al.* proposed a fully differentiable learning architecture and demonstrated a high-quality, polarization-insensitive nano-optic imager for full-color (400–700 nm), wide-FOV (40°) imaging with an f-number of 2[163]. As shown in Fig. 19(c), the end-to-end imaging pipeline is composed of an efficient metasurface image formation model and feature-based deconvolution algorithm. From the optimizable phase profile, the differentiable model produces saptially varying point spread functions (PSFs), which are then patch-wise convolved with the input image to form the sensor measurement. The sensor reading is then deconvolved using the algorithm to produce the final image. This approach can be extended towards flexible imaging with reconfigurable nanophotonics for various applications. Qingbin Fan *et al.* also developed a neural-network-based reconstruction algorithm to obtain high-quality imaging with metalens arrays[164]. They first generated a set of trainging data from the physically calibrated optical aberrations of the imaging system, then built a multiscale convolution neural network for aberration correction, and reconstructed the image from the experimentally captured data. Figure 19(d) displays the directly captured subimages (top row) and aberration-corrected images (bottom row), indicating the powerful abilities of the intelligent methods.

In addition to the enhancement of normal metalens imaging, intelligent methods play an important role in other imaging systems as well, such as light-sheet fluorescence microscopy. Din Ping Tsai's group implemented a GaN-based metalens with a genetic-algorithm-generated prism-like yet non-analytical phase profile[165]. It can significantly suppress the sidelobe intensity of the light sheet and also extend the depth of focus (DOF). Thus, it can exhibit an enhanced axial resolution and SNR when applied under two-photon excitation. Combined with a metalens array, this group also demonstrated a meta-device for intelligent depth perception[166], which indicates the advantages of intelligent methods in various applications[167].

3.6 Advances in Metalens Design and Fabrication

In previous years, most metalenses demonstrated are in micrometer-scale and have limited applications for practical imaging devices. Recently, some metalenses with millimeter scale have been demonstrated in experiments[168–171]. These large-scale metalenses, especially with nearly centimeter-scale, are in high demand in scenarios such as augmented reality/virtual reality (AR/VR) and landscope imaging, while the corresponding implementation faces challenges such as limited computational sources for simulation demonstration, the layout file with extremely high data density, and the diffculty of low-cost mass manufacturing.

Full-wave simulations can give an accurate picture of device performances. Simulations of metalenses with simple functions or with forward design can be scaled down to micrometer scale to reduce computing resources (i.e., memory space and run time). However, metalenses with complex functions (i.e., achromatism) or inverse design cannot be scaled down for proof-of-concept simulations. To address this issue, besides the optimization method illustrated in Fig. 19(b), Tyler W. Hughes *et al.* developed a GPU-based hardware-accelerated finite difference time domain (FDTD) solver titled "Tidy3D," which can perform simulations of large-area metalenses with a turnaround time on the minute scale[172]. A fully 3D, large-area metalens of size $100\lambda \times 100\lambda$, including focal length (46λ), is simulated in 5 min, indicating the advantages and necessities of this technique.

Taking a 5-cm-diameter metalens as an example comprising over 6 billion nanoscale meta-atoms, the corresponding size of the layout file is over 200 GB[173]. To reduce the file size, Federico Capasso's group proposed a scalable metasurface layout compression algorithm for devices with rotational symmetry, coined METAC[173]. A library of self-referenced structures is generated by using multiple layers to represent increasingly doubled copies of a primitive structure. At each

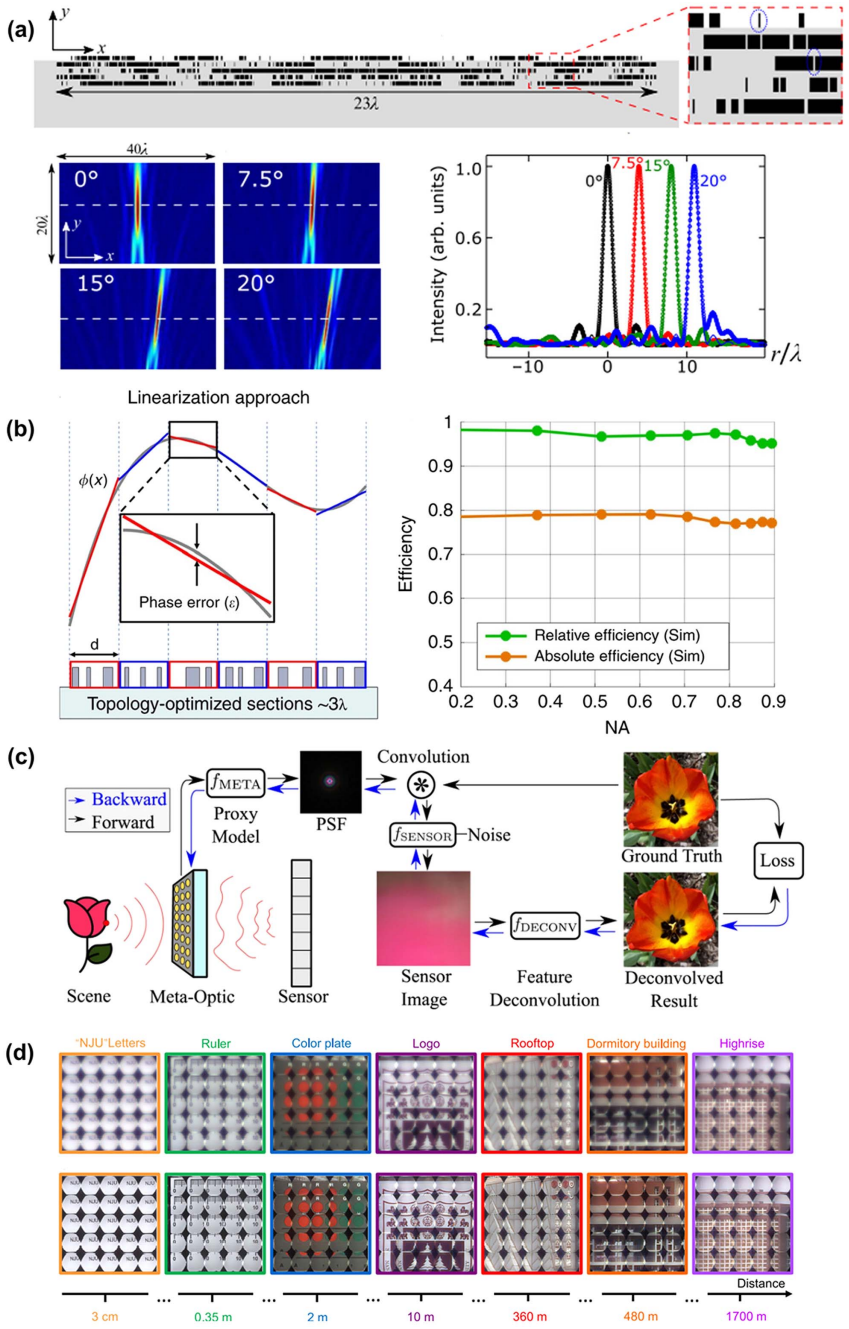

Fig. 19 Inverse design and AI algorithms in the metalens design and optimization. (a) Multilayered 2D metalens with aberration corrected under incident angles of 0°, 7.5°, 15°, and 20° based on topology optimization[136]. (b) Dividing the desired phase profile into linear sections with topology optimization for the design of metalens with large area and high efficiency[162]. (c) End-to-end neural imaging pipeline for full-color and wide-FOV imaging[163]. (d) Directly captured images (top row) and aberration corrected images (bottom row) based on AI methods for light-field imaging[164].

radial position, the core algorithm then efficiently assembles appropriate library elements to create the desired structure and form a ring. The aforementioned design file size is efficiently compressed by three orders of magnitude and reduced to approximately 131 MB, while for a metalens layout file with no radial symmetry, a similar efficient algorithm is urged to be developed.

Most reported metalenses, especially those working in the visible region (including the millimeter scale), were fabricated through electron beam lithography (EBL) or focused ion beam (FIB) techniques, which is quite time consuming with high cost. To achieve the requirements for mass production, several other techniques have been employed for metalens manufacturing[174–178]. For example, utilizing DUV projection stepper

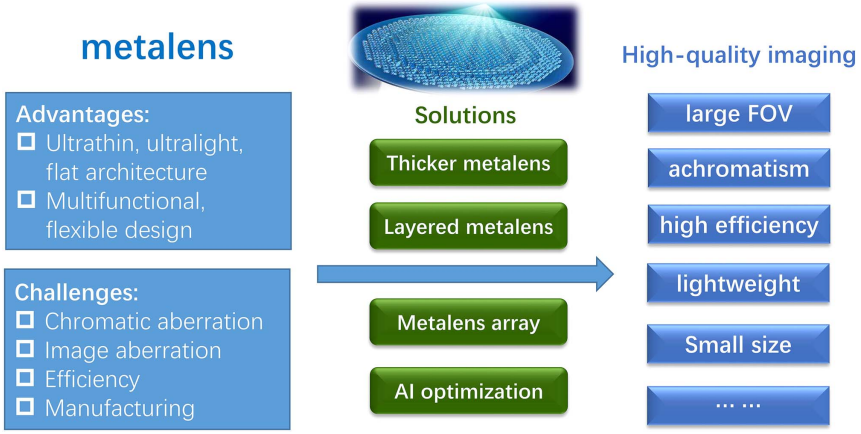

Fig. 20 Schematics of metalens roadmap towards high-quality imaging applications.

lithography[174,175], Federico Capasso's group demonstrated a centimeter-scale, all-glass metalens capable of focusing and imaging at visible wavelength[174]. Nanoimprint lithography (NIL) is also a promsing technology for mass production with high throughout and low cost[176–178]. Junsuk Rho's group developed printable metalenses composed of a Si nanocomposite synthesized by dispersing Si nanoparticles in a printing resin[177]. A metalens with a diameter of 4 mm and operating at 940 nm was demonstrated, and has only 10% uniform volume shrinkage compared with the initial master mold. Although these methods are more cost effective than EBL, their limitation in resolution and available materials hinders the fabrication of metalenses with complex functions (corresponding to small feature sizes) and efficient focusing in the visible.

In this section, we interpreted the concept and design principles of the metasurface and metalens. With the advantages of miniaturization and flexible design, metalenses have attracted great attention in both academia and industry, while transferring metalens technology from the laboratory to industry for practical applications still faces many challenges including design (correcting aberrations and enhancing efficiency) and manufacturing. By reviewing the development of the metalens, we can conclude several representative solutions (see Fig. 20) towards high-quality imaging (large FOV, achromatism, high efficiency, etc.), that is, providing thicker or layered metalenses for wider parameter space and more DoFs, constructing metalens arrays to break the function limitation of a single metalens, and utilizing AI optimization for performance improvement.

4 Multilevel Diffractive Lenses

4.1 Development of Diffractive Lenses

Conventional diffractive lenses have been the main technology to implement flat lenses for many years[179]. The earliest versions of diffractive lenses are Fresnel zone plates and Fresnel lenses. Fresnel zone plates consist of a set of radially symmetric rings (called Fresnel zones) alternating between being opaque and transparent, as shown in Fig. 21(a). The radius of each ring is chosen such that the distance from the edge of each zone to the focal point is an integral multiple of a half-wavelength longer than the axial focal length[180]. Then the transmission light diffracted from the transparent zone will constructively interfere at the desired focus, creating a focal spot like a focusing lens. However, a Fresnel zone plate designed for a nominal focal length f will generate multiple foci with corresponding focal lengths equaling $f/m, m = \pm 1, \pm 2, \pm 3, \ldots$ and the intensity of the mth-order image as a function of incident intensity, also known as the diffraction efficiency of the mth order, is given by[180]

$$\eta_m = \left[\frac{\sin\,(m\pi/2)}{m\pi}\right]^2. \tag{17}$$

The diffraction efficiency of the design order (first order) is $\eta_1 = 10.1\%$, which is shown in Fig. 21(f). Although a Fresnel zone plate is extremely thin and lightweight, relatively low diffraction efficiency, unwanted multiple images, and almost half-power blockage by the opaque area limit its practical use. Fresnel lenses also consist of a set of concentric annular sections, as shown in Fig. 21(b). Unlike Fresnel zone plates, each section of a Fresnel lens is made up of a prism, which can manipulate the phase profile $\varphi(r, \lambda)$ of transmission light based on accumulation of the optical path[179]:

$$\varphi(r, \lambda) = \frac{2\pi}{\lambda}[n(\lambda) - 1]h(r), \tag{18}$$

where λ is the wavelength, $n(\lambda)$ is the refractive index, and $h(r)$ is the height profile of the prism. The height profile is usually decided by the target phase φ_0 [such as hyperbolic phase in Eq. (10)] at a particular wavelength λ_0 in the design process:

$$h(r) = \frac{\lambda_0}{2\pi[n(\lambda_0) - 1]}(\varphi_0 \bmod 2\pi), \tag{19}$$

where mod means modulus. Thus, h ranges from zero to $\lambda_0/(n-1)$ for a conventional Fresnel lens. Generally speaking, the phase profile provided by a prism can deflect transmission light more efficiently than the Fresnel zone. Therefore, Fresnel lenses have much higher efficiency than that of Fresnel zone plates. The diffraction efficiency of the mth order of such a Fresnel lens at design wavelength λ_0 can be expressed as[180]

$$\eta_m = \left\{\frac{\sin[\pi(m-1)]}{\pi(m-1)}\right\}^2. \tag{20}$$

Based on Eq. (20), the diffraction efficiency of first order can reach 100% at λ_0, as shown in Fig. 21(g). The height profile of each prism in Fresnel lenses varies continuously, which can be fabricated by direct writing (laser or e-beam), gray-scale lithography, diamond turning, etc., as shown in Fig. 21(k)[179]. However, it is difficult to fabricate such smooth profiles for components working in the visible and near infrared precisely. Taking diamond turning as an example, the accuracy of the surface profile relies heavily on the size of the stylus tip used in diamond turning, and there often exist some fabrication errors such as an imperfect deep valley at the edge of each prism due to the finite size of the stylus tip [closed dashed lines in Fig. 21(k)][179,181]. The unavoidable fabrication error will significantly decrease the diffraction efficiency of Fresnel lenses in real applications.

Thus, a compromise has to be made between achieving high diffraction efficiency and ease of fabrication. With the development of binary optics in the 1980s, multilevel approximation provides a strategy to solve this problem[182]. Multilevel approximation means substituting the previous continuous height profile of the diffractive lens with discrete levels, as shown in Fig. 21(c). Such a diffractive lens is the earliest version of the multilevel diffractive lens (MDL). The two-level MDL, where the height profiles provide only zero or π phase shift, is the simplest form of MDLs and can be fabricated precisely

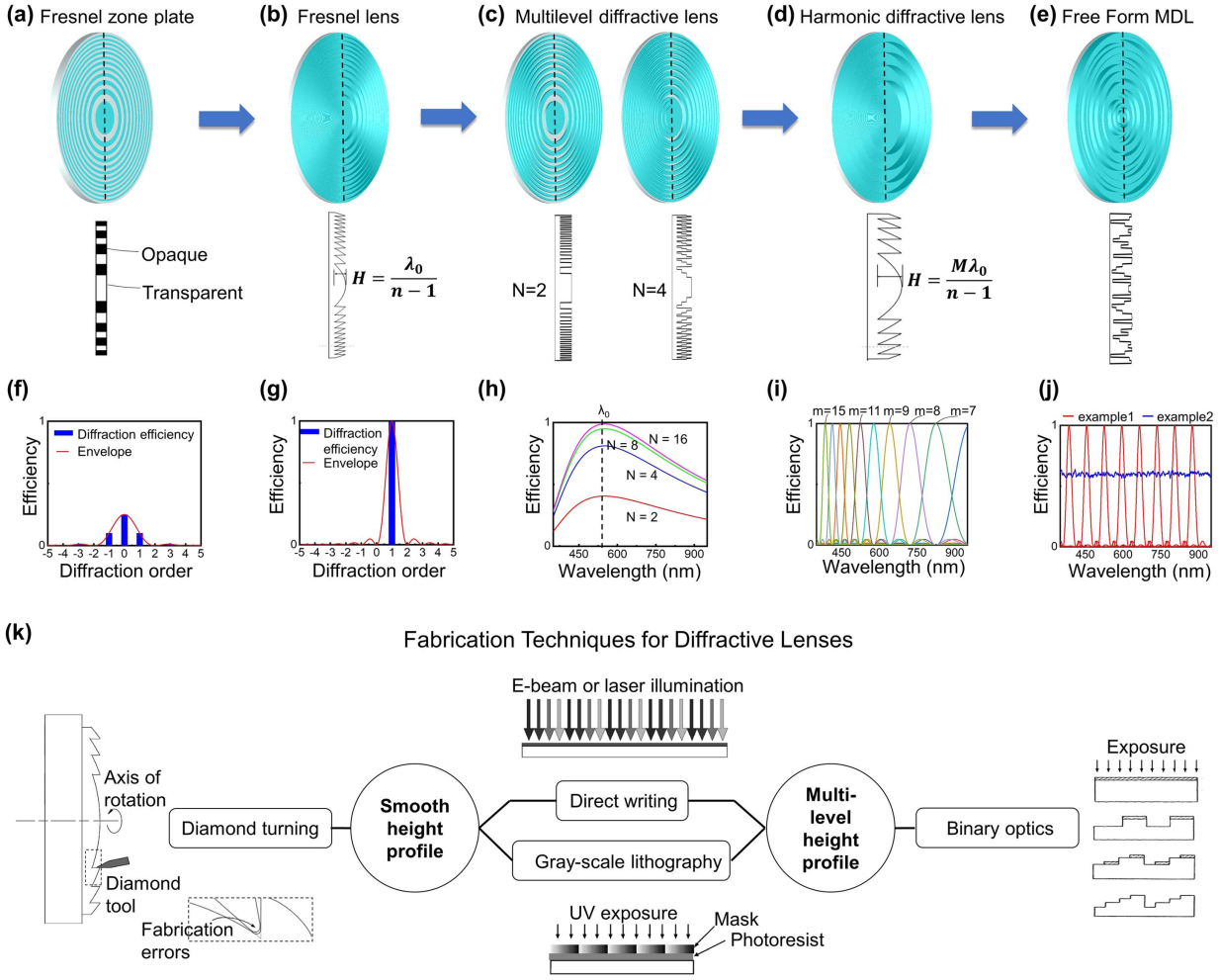

Fig. 21 (a)–(e) Development of conventional diffractive lenses. The top row shows the schematic of each diffractive lens. The bottom row denotes the height profile of each lens along the black dashed lines. (f) Diffraction efficiency with respect to the diffraction order for a Fresnel zone plate at design wavelength. (g) Diffraction efficiency with respect to the diffraction order for a Fresnel lens at design wavelength. (h) Diffraction efficiency with respect to wavelengths and gray levels for an MDL at first diffraction order. The black dashed line denotes the design wavelength λ_0. (i) Diffraction efficiency with respect to wavelengths and diffraction orders for a harmonic diffractive lens. (j) Diffraction efficiency with respect to wavelengths for two free-form MDLs, where example 1 denotes the achromatic MDL working at several discrete wavelengths with the same interval, and example 2 denotes the achromatic MDL working in broadband spectra. (k) Some fabrication techniques for diffractive lenses[179,181].

by binary optics as well as direct writing and gray-scale lithography. However, the diffraction efficiency of two-level MDLs is relatively low (for first order). The diffraction efficiency of an MDL at the mth order with N levels is given by[180]

$$\eta_m^N = \left\{\frac{\sin[\pi(1-m)]}{\pi(1-m)}\right\}^2 \left[\frac{\sin(\pi/N)}{\pi/N}\right]^2, \tag{21}$$

which means the diffraction efficiency of first order with two levels reaches only 41%. Increasing level N is an effective way to increase diffraction efficiency based on Eq. (21). Thus, in a practical application, the level is usually set as eight or higher, where diffraction efficiency can reach more than 95% at a designed wavelength λ_0.

The above discussion considers only the situation when the diffractive lens is operating at a designed wavelength λ_0. In fact, all the diffractive lenses mentioned above (including Fresnel zone plates, Fresnel lenses, or MDLs, and metalenses) have large chromatic aberrations due to intrinsic diffraction dispersion[179]. On one hand, in the same diffraction order, the focus length f will decrease as the wavelength λ increases. On the other hand, diffraction efficiency will decrease when the wavelength deviates from the designed one. For example, the diffraction efficiency for an MDL operating at other wavelengths λ is given by

$$\eta_m^N = \left\{\frac{\sin\{\pi[\alpha(\lambda)-m]\}}{\pi(\alpha(\lambda)-m)}\right\}^2 \left[\frac{\sin(\pi/N)}{\pi/N}\right]^2, \tag{22}$$

where α is the detuning parameter, defined as $\alpha = \lambda_0[n(\lambda)-1]/\lambda[n(\lambda_0)-1]$[181]. Figure 21(h) shows the distribution of the first-order η_1 with respect to wavelength λ and level N. The efficiency reaches maximum at λ_0 and decreases quickly as λ deviates from λ_0. Such a chromatic aberration will degrade the quality of images taken from these diffractive lenses under broadband illumination, which severely leads to harmful color blur, low SNR, low resolution, etc.

To reduce the chromatic aberration and improve the average diffraction efficiency of diffractive lenses in a certain broad bandwidth, harmonic diffractive lenses were proposed in 1995[183,184]. The harmonic diffractive lens is a diffractive imaging lens for which the optical path length transition between adjacent facets is M multiples (M is an integer) of the design wavelength λ_0, which means the total thickness of the lens is $H = M\lambda_0/(n-1)$, as shown in Fig. 21(d). Harmonic diffractive lenses have hybrid properties of both refractive and diffractive lenses and can reach very high diffraction efficiency at several wavelengths (called harmonic wavelengths) rather than one, while the focus lengths of these harmonic wavelengths remain the same. The diffraction efficiency of mth order for a harmonic diffractive lens is given by[183]

$$\eta_m = \left\{\frac{\sin\{\pi[M\alpha(\lambda)-m]\}}{\pi[M\alpha(\lambda)-m]}\right\}^2. \tag{23}$$

The mth harmonic wavelength $\lambda_m = M\lambda_0[n(\lambda)-1]/m[n(\lambda_0)-1]$, as shown in Fig. 21(i). The diffraction efficiency of the mth harmonic wavelength λ_m will reach 100% at the corresponding mth diffraction order. As the height index M increases, the number of harmonic wavelengths will increase, which improves diffraction efficiency in the working bandwidth. Nevertheless, harmonic diffractive lenses have two disadvantages. First, the harmonic wavelengths are fixed and the interval between two adjacent wavelengths cannot be manipulated flexibly for a given thickness. Second, diffraction efficiency will also decrease if the lens is operated at the interval wavelengths (wavelength between two adjacent harmonic wavelengths). Thus, harmonic diffractive lenses seem not to be the ultimate solution to realize broadband focusing and imaging.

To further increase the DoF in design, a new class of diffractive lenses, denoted free-form MDLs, has been proposed in recent years[185–197]. The height profile of the free-form MDL is irregular and quite different from that of conventional diffractive lenses, as shown in Fig. 21(e). Free-form MDLs can realize many more functionalities, such as achromatism in broadband [blue line in Fig. 21(j)] or at several discrete wavelengths with the same interval [red line in Fig. 21(j)][185–197]. The free-form MDL is designed by inverse design as introduced in Section 3.4. Specifically, there are two constraints in the design of free-form MDL—the height of each ring should be discrete and in the interval $[0, H]$. Thus, the design problem can be expressed as[185,190]

$$\max\ F(H) \quad \text{s.t.} \quad 0 \le h(r) \le H \quad 0 \le r \le R, \tag{24}$$

where F is FoM, and R is the lens radius. By setting FoMs as different types of functions, MDL with different functionalities (achromatism, etc.) can be realized. Next, we will review recent works on several types of free-form MDLs, such as achromatic MDLs, an MDL with a long DOF, and an MDL with a large FOV.

4.2 Achromatic MDL for Imaging

The achromatic MDL (AMDL) is a typical free-form MDL to realize discrete or continuous band achromatism, first proposed by Rajesh Menon's group in 2016[185]. The AMDL can be regarded as a combination of harmonic diffractive lenses and MDLs with free-form height profiles. To achieve achromatism, the light of different wavelengths diffracted from the AMDL needs to constructively interfere at the same focus. Thus, the FoM can be directly set as the intensity at the focus (denoted as I_0):

$$F = \frac{1}{N_\lambda}\sum_\lambda I_0(\lambda), \tag{25}$$

where N_λ is the number of wavelengths optimized in achromatic design. Equivalently, the maximization of light intensity at the focus can be translated to maximization of the power in the focus disc. Therefore, the FoM could also be set as a power ratio:

$$F = \frac{1}{N_\lambda}\sum_{N_\lambda}\frac{\int_0^{1.5w} I(r,\lambda)r\mathrm{d}r}{\int_0^R I(r,\lambda)r\mathrm{d}r}, \tag{26}$$

where w is the full width at half maximum (FWHM), and $I(r,\lambda)$ is the light intensity distribution on the focus plane. More details about other FoMs, such as the difference between real and ideal light intensity distributions at the focal plane or the difference between real and ideal phase profiles at lens surfaces, are presented in Refs. [185,190,191].

The optimal height profile $h(r)$ can be yielded by solving Eq. (24). Generally speaking, Eq. (24) is a nonlinear optimization problem of which the global optimal solution cannot be derived easily. In previous works, several optimization algorithms have been proposed to address this difficult problem. A direct binary search (DBS) is one of the most used algorithms[185]. DBS is a pattern searching method[192,193], where a perturbation δh will be added on the height profile h to get a trial solution in one iteration. If the FoM of the trial solution is better than the previous one, the height profile will be updated as $h + \delta h$. If not, the height profile will remain as h. The optimal height profile h^* will be yielded based on this method after several iterations. Other algorithms such as brute-force search or gradient-descent are also applied to solve Eq. (24) in some related works[190,191]. It should be mentioned that almost all of these methods are local optimization algorithms and cannot achieve the optimal height profile by just one trial. In fact, random initialization is necessary in the optimization. The application of some global optimization algorithms, such as a genetic algorithm or particle swarm optimization[194], may be helpful to get a better result.

Based on inverse design, several examples of AMDLs operating in various regions of the EM spectrum, ranging from the visible to the microwave, are demonstrated experimentally, as illustrated in Fig. 22. In the visible and near-infrared regions, Peng Wang *et al.* demonstrated a 2D AMDL (focusing incident light to a line, akin to conventional cylindrical lenses) that can work on large bandwidths with super-achromatic performance over the continuous visible band (450–750 nm) in 2016[185]. The AMDL is made up of SC1827 (a kind of photoresist). The length and total thickness of such an AMDL reach 7.5 mm and 2.6 μm, respectively, which is much larger than that of achromatic metalenses[26,27,29,122,126,127,198–200]. However, this AMDL is just a first trial, and its NA is only 0.013. Different from conventional diffractive lenses, the diffraction efficiency of the AMDL is usually defined as the ratio of optical power within three times FWHM of PSF over the whole transmitted optical power, while another metric, focusing efficiency, is defined as the ratio of optical power within three times FWHM of PSF over the whole incident optical power[195]. The overall focusing efficiency of the AMDL in this work is around 10%, as shown in Fig. 22(a). Yifan Peng *et al.* demonstrated an AMDL by equalizing the spectral focusing performance within the whole visible spectrum in the same year, as shown in Fig. 22(b)[190]. The AMDL is made of silica with working spectra over 410–690 nm, diameter equal to 8 mm, thickness equal to 1.195 μm, and

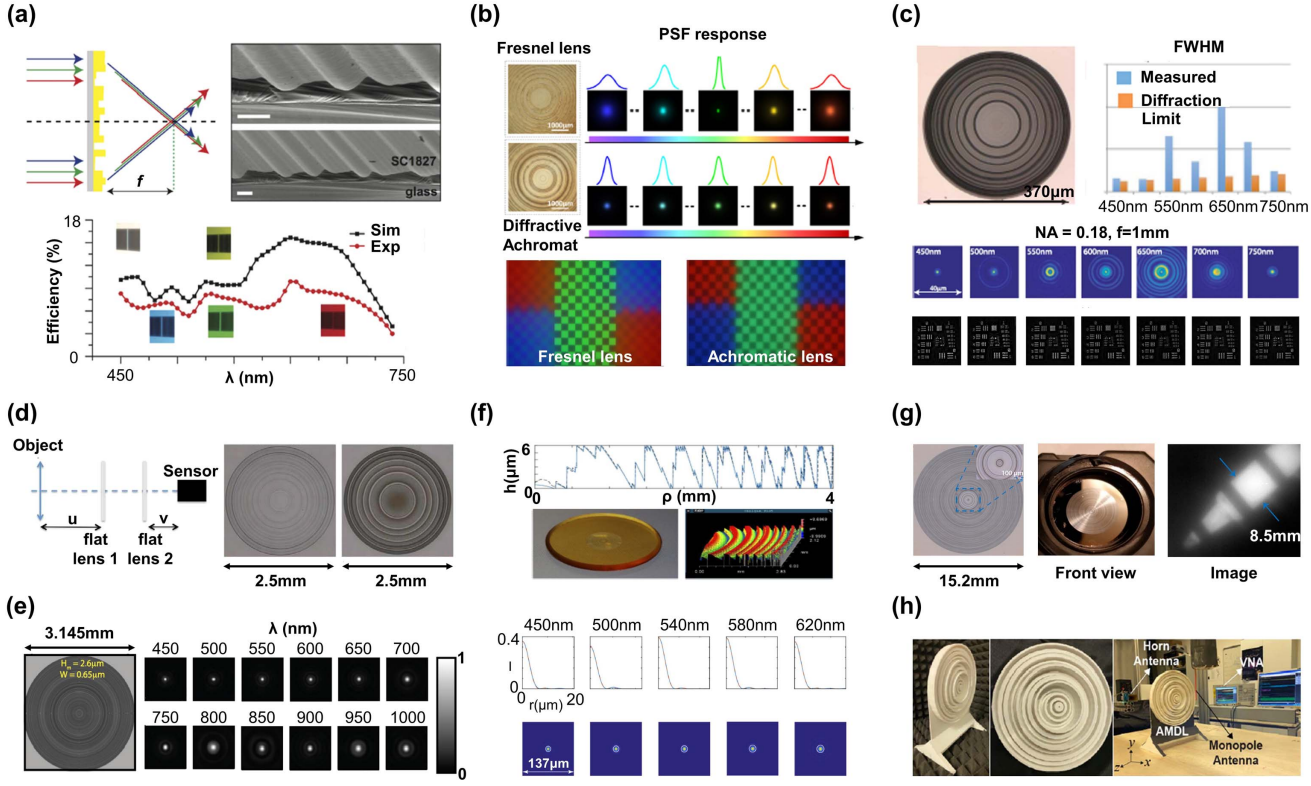

Fig. 22 Typical examples of achromatic MDLs. (a) 2D broadband AMDL working in the visible region[185]. (b) Broadband AMDL over the visible range from 410 nm to 690 nm with NA = 0.04 and diameter equal to 8 mm[190]. (c) Broadband AMDL working in the visible region with NA = 0.18 and diameter equal to 370 μm[196]. (d) Schematic of an imaging system composed of two AMDLs[197]. (e) Broadband AMDL over the visible and near-infrared range from 450 nm to 1000 nm with NA = 0.3 and diameter equal to 3.145 mm[187]. (f) Multiwavelength AMDL working over 450 nm to 620 nm[186]. (g) Broadband AMDL over the long-wave infrared region (8–12 μm) with NA = 0.45 and diameter equal to 15.2 mm[28]. (h) Broadband AMDL over the microwave region (10–14 GHz) with NA = 0.99 and diameter equal to 186 mm[191].

NA = 0.04. They also made a comparison between images taken by the AMDL and a conventional Fresnel lens. The performance of the AMDL is a little bit worse than that of the Fresnel lens at the design wavelength (550 nm), but the overall performance of the AMDL under broadband illumination is better, which demonstrates the achromatism of the AMDL. In 2018, Nabil Mohammad *et al.* proposed an AMDL working in 450–750 nm, as shown in Fig. 22(c)[196]. Although the diameter of such an AMDL is only 370 μm, its NA reaches 0.18 and overall efficiency increases to 22.1%. They also demonstrated a simple imaging system composed of two AMDLs in the same year, as shown in Fig. 22(d)[197]. In 2020, Monjurul Meem *et al.* demonstrated an AMDL working at 450–1000 nm, with diameter of 3.145 mm, thickness of 2.6 μm, NA of 0.3, and overall focusing efficiency of 12%, as shown in Fig. 22(e)[187]. In the same year, Leonid L. Doskolovich *et al.* demonstrated an AMDL working at several discrete wavelengths (450–620 nm), with diameter equal to 8 mm, thickness equal to 6 μm, and NA = 0.04, as shown in Fig. 22(f)[186]. The average focusing efficiency of this AMDL reaches 39.6% (simulation) and 16.4% (experiment).

In the long-wave infrared region to microwave region, a polymer AMDL with a relatively high NA of 0.371 and working at 8 μm to 12 μm was proposed by Monjurul Meem *et al.* in 2019, as shown in Fig. 22(g)[28]. The diameter and total thickness of this AMDL are 15.2 mm and 10 μm, respectively, and the average focusing efficiency in the range of 8–12 μm reaches 43% experimentally. The AMDL exhibits aberrations comparable to or better than those seen in conventional refractive lenses, which shows great potential in applications in the long-wave infrared region. In 2021, Bumın K. Yildirim *et al.* demonstrated an AMDL working at 10 GHz to 14 GHz with ultrahigh NA = 0.99, as shown in Fig. 22(h)[191]. A multi-objective differential evolution algorithm was incorporated with the 3D finite-difference time-domain method to optimize both the heights and widths of each concentric ring of the AMDL. The diameter and total thickness of this AMDL are 186 mm and 26 mm, respectively, with average focusing efficiency of around 35%. They also numerically demonstrated an AMDL working in the visible (380–620 nm) with diameter of 3.3 μm, thickness of 0.46 μm, NA of 0.985, and overall efficiency of around 44%.

All the above works demonstrated the feasibility of the AMDL to realize achromatism, but none of these AMDLs simultaneously achieve a large diameter, high NA, small thickness, and high focusing efficiency, which indicates that there may exist a fundamental physical bound for the AMDL like that for the achromatic metalens. To work out the physical bound would provide an important guidance for us to realize AMDLs (as well as achromatic metalenses) with better performance. However, most previous theoretical works analyze such a physical bound based on the group delay of the ideal achromatic flat lens, of which an important assumption is that the phase profile of the lens always follows hyperbolic distribution [Eq. (10)]. In fact, the focus and image performances of most reported AMDLs are below the diffraction limit, which indicates that such AMDLs are non-ideal achromatic flat lenses, or equivalently, there will exist distortion $\Delta\varphi$ in the phase profile of such AMDLs:

$$\varphi(\rho,\omega) = -\frac{\omega}{c}\left(\sqrt{\rho^2+F^2}-F\right)+\Delta\varphi(\rho,\omega). \tag{27}$$

The general form of group delay $\partial\varphi/\partial\omega$ cannot be derived in this case, for the specific form of phase distortion $\Delta\varphi$ remaining unknown. Thus, it is very hard to work out a quantitative restriction relation for non-ideal achromatic flat lenses based on the previous method. Considering that the effect of phase distortion is in fact to decrease the coherence of a light field at both the lens surface and focus, Xingjian Xiao *et al.* introduced light frequency domain coherence into the analysis[188]. The coherence function at a lens surface is defined as

$$J_\omega(\rho_1,\rho_2) = \langle e^{i\Delta\varphi(\rho_1,\omega)}e^{-i\Delta\varphi(\rho_2,\omega)}\rangle_\omega, \tag{28}$$

where $\langle\rangle_\omega$ means frequency-averaging operation, and ρ_1 and ρ_2 are two radial coordinates on the lens surface. Based on the propagation of coherence and several approximations, the restriction relations between the upper bound of the coherence function at the focus [denoted as max $J_\omega(F)$] and other parameters can be derived:

$$D_{\max} \approx \frac{4(n_{\max}-1)H}{\left[1-\sqrt{1-\max J_\omega(F)}\right]\mathrm{NA}}, \tag{29}$$

where $n_{\max}$ is the maximum refractive index over the whole spectrum, and $D_{\max}$ is the maximum diameter of a non-ideal achromatic flat lens with given thickness H, NA, $n_{\max}$, and max $J_\omega(F)$. Additionally, max $J_\omega(F)$ is approximately proportional to the maximum average diffraction efficiency that an achromatic flat lens with given parameters can reach. Thus, even though Eq. (29) is just a rough approximation, it gives us intuitive insight into the design trade-offs for non-ideal achromatic flat lenses. It reveals that to realize an achromatic flat lens with a large diameter, high NA, and high focusing efficiency, the thickness of the lens must be relatively large. Based on Eq. (29), the comprehensive performance of an achromatic flat lens, which includes lens aperture, NA, and focusing efficiency, can be defined using an index of product $P = D[1-\sqrt{1-J_\omega(F)}]\mathrm{NA}$. The comprehensive performances of some reported AMDLs and achromatic metalenses with respect to the effective thickness $H_{\mathrm{eff}} = (n_{\max}-1)H$ are summarized in Fig. 23(a) and Table 1, where P indeed displays a strong positive correlation with H_{eff}. Under the guidance of this theory, they further demonstrated several AMDLs with diameters ranging from 1 mm to 1 cm and thickness ranging from 1 μm to 15 μm. Figure 23(b) shows the top view and side view of a typical AMDL with $D = 1$ cm, $H = 15$ μm, with working wavelength ranging from 400 nm to 1100 nm, while Fig. 23(c) exhibits the achromatic focusing performance of this lens in the visible. The advantages in imaging performance of the AMDL are also evaluated by comparing it with a conventional refractive lens (LE1234) and a commercial Fresnel lens, as shown in Figs. 23(d) and 23(e). Although the images taken from the AMDL are a little bit dark due to the relatively lower efficiency, there is no color blurring effect that is obvious for the Fresnel lens or the refractive lens. Considering it is thin and lightweight, such an AMDL is very promising for portable and convenient applications in the near future.

As a summary for the state-of-the-art performances of achromatic flat lenses (including AMDLs and achromatic metalenses), Table 1 presents the major parameters with an assessment of the comprehensive performances[188]. The references in Table 1 are sorted into two categories. The first category

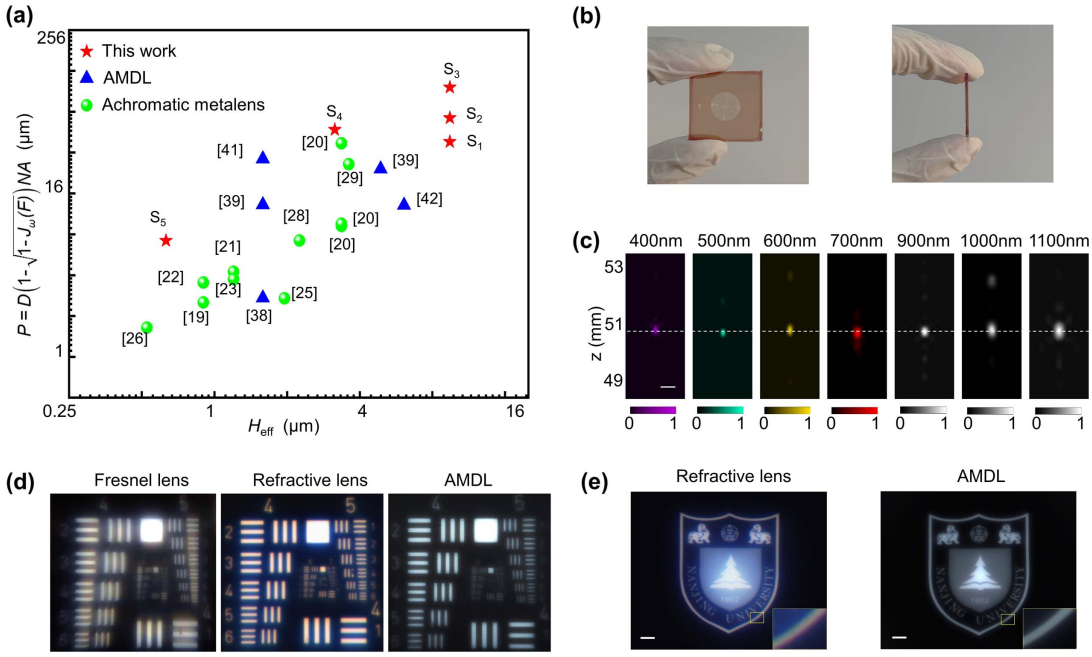

Fig. 23 Large-scale achromatic flat lens by light coherence optimization[188]. (a) Comprehensive performance P of reported achromatic metalenses and AMDLs with respect to effective thickness H_{eff}. (b) Photographs of a fabricated AMDL; left and right are top and side views, respectively. (c) Experimental light intensity profiles for AMDL at seven different incident wavelengths in the visible. Scale bar: 15 μm. (d) Image of 1951 USAF resolution test chart taken from the Fresnel lens, refractive lens, and AMDL. (e) Image of Nanjing University logo taken from the refractive lens and AMDL. Zoom-in image shows the edge details of the logo.

contains several works on achromatic metalenses, denoted by the superscript ○. The second category contains several works on achromatic MDLs, denoted by the superscript Δ. All references in each category are sorted by publishing time. The measured efficiency in most reported works is the total efficiency (including focusing efficiency and transmittance). Here, to normalize them for comparison, we calculated them according to their detailed structural parameters and retrieved their diffraction efficiency, $J_\omega(F)$, and P with respect to the effective height H_{eff}. As details indicate in Ref. [188], the effective height H_{eff} is equal to $(n-1)H$, diffraction efficiency is equal to the total efficiency/[transmittance × polarization conversion ratio] (PCR), and $J_\omega(F)$ is equal to the average diffraction efficiency/FWHM^2. It should be noted that only the diffraction efficiency can be calculated theoretically, which would be reasonably a little bit larger than the total efficiency according to the non-unity transmittance. For some high-transmittance cases, these two values are very close. However, for some metalens cases with polarization rotation (i.e., based on the PB phase design), it needs to take the PCR into account besides the transmission efficiency. Therefore, the diffractive efficiencies retrieved purely from diffraction would be much higher than the measured data, which is indicated by asterisks (*) in the column "Diffraction efficiency." From the data, we can clearly observe the strongly positive correlation between the comprehensive performance [diffraction efficiency, $J_\omega(F)$, and P] and the effective height (H_{eff}), which further proves that increasing the height is an effective means to further improve the comprehensive performance of the achromatic lens even to an applicable level.

4.3 MDLs with Function Extensions

By setting different FoM forms in Eq. (24), the free-form MDL with other novel functionalities can also be realized based on the inverse design, such as an MDL with a long DOF and an MDL with a large FOV.

MDL with long DOF. A photoresist MDL working at 0.85 μm with an extremely long DOF was demonstrated by Sourangsu Banerji *et al.* in 2020, as shown in Fig. 24(a)[189]. Such an MDL is realized by setting FoM as the focusing efficiency along the propagation axis. The diameter and total thickness of this MDL are 1.8 mm and 2.6 μm, respectively, while its DOF reaches 1195 mm (focal length f ranges from 5 mm to 1200 mm). As a comparison, the diffraction-limited DOF for a common lens with the same parameters is only 26 μm, which means the enhancement in DOF is about four orders of magnitude for this MDL. The imaging ability of objects spread as far apart as almost 6 m is also demonstrated where all such objects were in focus. This work shows the potential to substitute the conventional imaging module with a single flat lens. However, the modulation transfer function (MTF) of this MDL is relatively low compared to the diffraction limitation, and thus, the SNR of images taken by this lens is low as well, which may limit its practical use. An alternative method to improve the MTF is to increase the thickness of the MDL as well as to change the design goal from focusing at every point along the propagation axis to focusing at just several discrete points on the propagation axis, which was proposed by Fengbin Zhou *et al.* in 2022 and is shown in Fig. 24(b)[202]. The MDL works at RGB channels (658 nm, 532 nm, 450 nm) with large DOF to

Table 1 State-of-the-Art Performances and Related Parameters of Reported Achromatic Flat Lens.

	Reported Data						Calculated Data			
Ref.	D (μm)	H (μm)	λ (μm)	NA	Refractive Index n	Measured Efficiency	H_{eff} (μm)	Diffraction Efficiency	$J_\omega(F)$	P
[27]○	25.72	0.6	0.47–0.67	0.2	2.5	~30%	0.9	~72%*	0.7	2.5
[29]○	100	1.4	1.2–1.4	0.88	3.5	~50%	3.36	~71%	0.67	37.4
[29]○	100	1.4	1.2–1.65	0.24	3.5	~39%	3.36	~56%	0.62	9.2
[29]○	200	1.4	1.2–1.65	0.13	3.5	~38%	3.36	~55%	0.55	9.6
[26]○	50	0.8	0.4–0.66	0.106	2.4	~40%	1.2	~94%*	0.93	4.2
[122]○	26.4	0.6	0.46–0.7	0.2	2.4	~35%	0.9	~84%*	0.84	3.5
[198]○	21.6	0.8	0.4–0.66	0.216	2.4	~40%	1.2	~94%*	0.92	3.7
[127]○	20	3.9	1–1.8	0.27	1.5	~68%	1.95	~72%	0.71	2.7
[199]○	20	0.35	0.64–1.2	0.12	2.4	~70%	0.53	~85%	0.85	1.6
[126]○	30	1.5	0.65–1	0.24	2.4	~78%	2.25	~95%	0.95	7.2
[200]○	490	1.5	1.3–1.7	0.238	3.5	~25%	3.6	~37%	0.34	26.3
[130]○	20	2.5	0.45–1.7	0.27	1.57	~65%	1.42	~69%	0.65	2.7
[130]○	200	2.5	0.45–1.7	0.04	1.57	~42%	1.42	~45%	0.44	2.5
[196]△	370	2.6	0.45–0.75	0.18	1.61	~22%	1.59	~23%	0.08	2.7
[197]△	2500	2.6	0.44–0.66	0.05	1.61	~60%	1.59	~63%	0.2	13.2
[197]△	2500	8	0.44–0.66	0.05	1.61	~38%	4.88	~40%	0.35	24.2
[187]△	3145	2.6	0.45–1	0.3	1.61	~12%	1.59	~12%	0.06	28.7
[201]△	992	10	0.45–15	0.0275	1.61	~85%	6.1	~90%	0.73	13.1
[188]△	1024	15	0.4–1.1	0.1	1.63	~64%	9.45	~68%	0.61	38.2
[188]△	3072	15	0.4–1.1	0.1	1.63	~40%	9.45	~42%	0.34	58.2
[188]△	10,240	15	0.4–1.1	0.1	1.63	~29%	9.45	~31%	0.18	97.0
[188]△	10,240	5	0.4–1.1	0.1	1.63	~17%	3.15	~18%	0.09	44.0
[188]△	10,240	1	0.4–1.1	0.1	1.63	~5%	0.63	~5%	0.014	7.2

realize a vector light field display. The diameter and total thickness of this MDL are 10 mm and 5 μm, respectively. The DOF ranges from 20 mm to 110 mm. This MDL exhibits much higher image quality. By integrating the MDL with a liquid crystal display (LCD), a smooth horizontal parallax with cross talk below 26% over a viewing distance from 24 cm to 90 cm is demonstrated. The proposed display system has the advantages of a thin form factor, high efficiency, high color fidelity, and large viewing distance, showing potential applications including portable electronics, 3DTVs, and tabletop displays.

MDL with large FOV. In 2019, Yifan Peng *et al.* proposed a diffractive lens with a large FOV (=53°), which provides almost an order of magnitude increase compared to a conventional aspherical lens[182]. Such a lens is designed in two steps. The first step is to generate an ideal phase profile for spatially invariant PSFs over the full FOV, which ensures a large FOV. The second step is to generate a height profile to approximately provide such an ideal phase profile. The FoM in this optimization problem is set as the difference between the phase profile provided by the lens and the ideal phase profile, and corresponding inverse design is performed on Zemax. Strictly speaking, the diffractive lens does not apply multilevel approximation and is more like a harmonic diffractive lens with a smooth free-form height profile in each zone. The diameter, effective modulation thickness, and NA of this lens are 23.4 mm, 120 μm, and 0.2625, respectively. Figure 24(c) shows the spatial distribution of the PSF under different incident angles and example captures of a checkerboard target across the full sensor. The experimentally measured PSF of this lens preserves high-frequency details and is almost spatially invariant, while the PSF of a conventional aspheric lens exhibits large aberrations when the incident angle is large. The image results demonstrate that this lens balances the contrast detection probability (CDP) across the full FOV. CDP is a probabilistic measure to characterize the ability of a higher-level processing block to detect a given contrast between two reference points after the full imaging chain. For this diffractive lens, a significant CDP floor of almost 50% is preserved across the full FOV, ranging from 40% at on-axis angular direction to above 80% at the most tilted angle. In contrast, the CDP of an aspherical lens drops drastically and approaches 0% at view directions larger than 0.5× half-FOV. Both focus results and imaging results demonstrate the ability of the diffractive lens to realize a large FOV.

4.4 Computation-enhanced MDL Imaging

Although free-form MDLs show great potential in extending working spectra, FOV, and DOF of optical imaging while

reducing the volume of an imaging system, the quality of images taken from most free-form MDLs is relatively low due to the low focusing efficiency and MTF. As discussed above, focusing efficiency is limited by the generalized restriction relations, which means low focusing efficiency is an intrinsic problem and cannot be solved just by applying more advanced design methods (if thickness of MDL is fixed). Therefore, it is difficult to directly apply free-form MDLs in practical imaging systems to provide performance comparable to state-of-the-art imaging modules composed of conventional refractive lenses.

One possible solution is to combine free-form MDLs with advanced image processing technology. Yifan Peng *et al.* introduced a two-step deconvolution algorithm to improve the image quality of the AMDL in 2018, as shown in Fig. 24(d)[190]. The first step is the deconvolution on a down-sampled image to deblur large edges and remove strong color corrupted noise. The second step is to apply a cross-scale prior in our regularization term, which borrows the relatively sharp and denoised edge information from the up-sampled image of the first step's result to benefit the deconvolution at full scale. The AMDL combined with the deconvolution algorithm is able to image natural scenes with competitive resolution and color fidelity.

The deep neural network (DNN) is another powerful tool to improve image quality. In 2019, Yifan Peng *et al.* introduced a learned generative adversarial network (GAN) to recover high-quality images taken by a diffractive lens[182]. The structure of the GAN is shown in Fig. 24(e). Data used to train the network are generated by a display-capture laboratory setup composed of an LCD monitor, the diffractive lens, and image sensor. Such a setup omits the manual acquisition of the dataset in the wild and reduces difficulties in alignment. After training, the GAN was able to map captured blurry images to clean reconstructed images. This work made a significant step towards the quality of commercial compound lens systems with just a single free-form diffractive lens.

5 Application Scenarios

We have reviewed the progress of three types of lenses based on or related to meta designs: superlens, metalens, and MDL. It is undoubted that the concept of the superlens proposed by John Pendry has tremendous significance in scientific innovation, though it still suffers from massive applications in either sub-wavelength bio-imaging or nano-lithography[203]. Under some special conditions, it has been developed to SPP lithography,

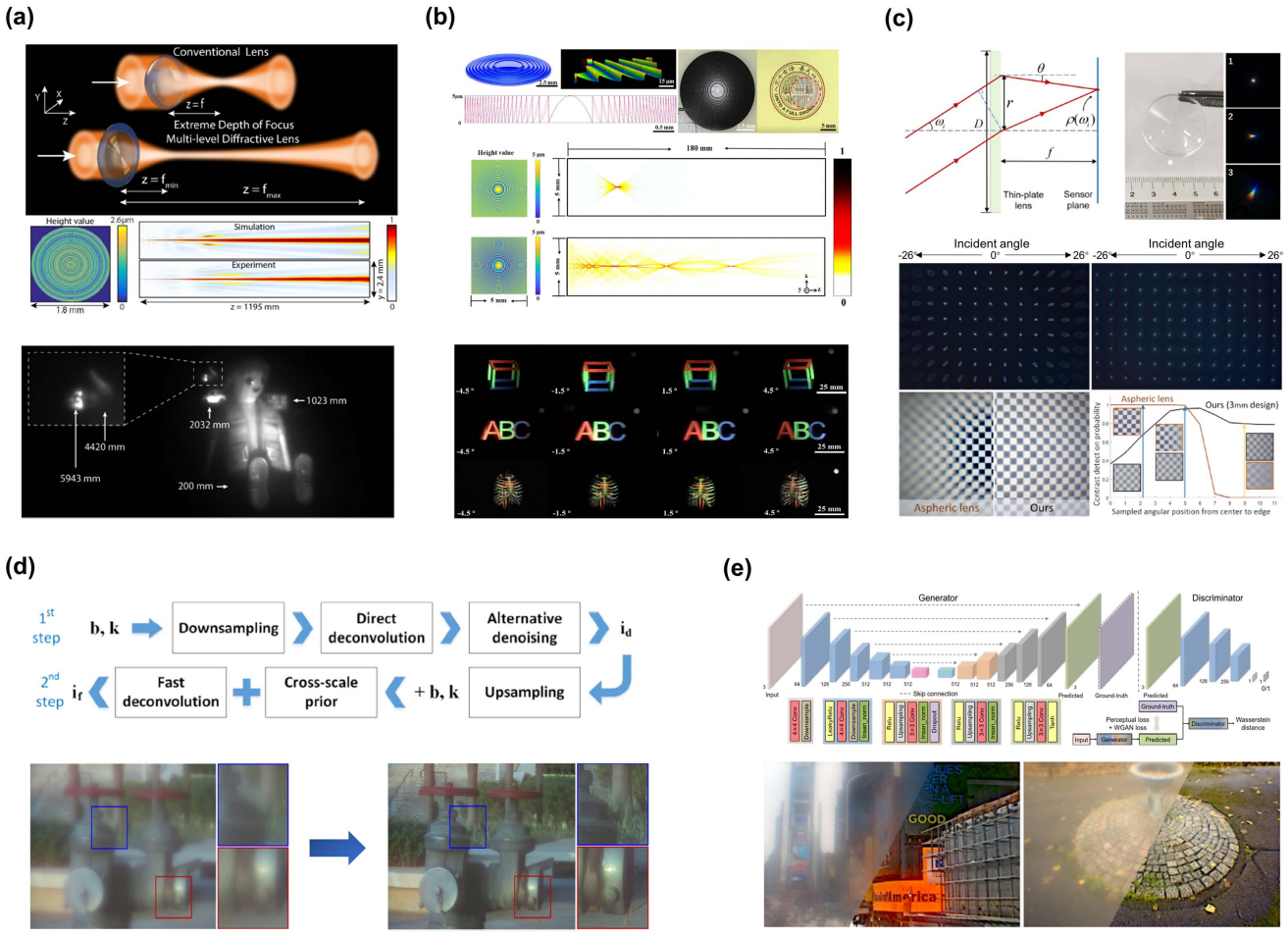

Fig. 24 Typical examples of free-form diffractive lenses applied in other areas. (a) Free-form MDL working at 850 nm with extremely long DOF (5–1200 mm)[189]. (b) Free-form MDL working at RGB (658 nm, 532 nm, 450 nm) with long DOF (2–10 mm)[202]. (c) Free-form diffractive lens over the visible region with large FOV (53°)[182]. (d) Combination of diffractive lenses with deconvolution algorithm[190]. (e) Combination of diffractive lenses with GAN[182].

which could be possibly generalized for wider applications. For example, Xiangang Luo *et al.* built an SPP lithograph system to realize sub-22-nm half-pitch lithography, providing a viable alternative to traditional costly and complex optical lithography systems[204,205]. Moreover, the innovative concept also illuminates possible applications in other fields, such as photonic chips with signal transmission in subwavelength scales[61] and new platforms revealing novel physics such as photonics Weyl media[63].

5.1 Zoom Imaging

Zoom imaging is a noteworthy functionality of lenses when dealing with complex scenarios. Tunable and varifocal metalenses, which break the limits of bulky refractive optical zoom systems, have attracted great attention among researchers. The key point to obtain different focal lengths is to empower metalenses with distinct phase profiles under different external stimuli. Several strategies have been proposed to realize efficient modulation. Among them, referencing conventional optics, mechanical deformation or displacement-enabled zoom is the most widely utilized method. For instance, as shown in Fig. 25(a), by mechanically stretching the polydimethylsiloxane substrate, the lattice constant of a complex Au nanorod array fabricated on the substrate can be changed, and with the reconfigurable phase profile, a 1.7× zoom metalens in the visible was demonstrated[206]. Kentaro Iwami *et al.* also reported an experimental demonstration of a moiré metalens that shows focal length tunability in ranges between ±1.73 and ± 5 mm by mutual angle rotation between ±90° at the wavelength of 900 nm [207] [see Fig. 25(b)]. Yuan Luo *et al.* also implemented a dielectric moiré metalens for fluorescence imaging, with variable focal length ranging from ∼10 to ∼125 mm at 532 nm by tuning mutual angles[208]. Inspired by an Alvarez lens, Shane Colburn *et al.* built a 1-cm aperture varifocal metalens system at 1550-nm wavelength and demonstrated a nonlinear change in focal length by minimally actuating two cubic phase metasurfaces laterally [see Fig. 25(c)], with focusing efficiency as high as 57% and a wide focal length change of more than 6 cm (>200%)[209].

The required mechanical displacement can also be modulated electrically. Incorporated with microelectromechanical systems (MEMS), Andrei Faraon's group demonstrated tunable metasurface doublets with more than 60 diopters (about 4%) change in optical power upon a 1-μm movement of one metasurface, and a scanning frequency that can potentially reach a few kHz [see Fig. 25(d)][210]. This kind of MEMS-integrated metasurface performs as an applicable platform for tunable and reconfigurable optics. Reconfigurable materials with optical properties changed by external actuation can be utilized to realize multi-focus metalenses as well. The most representative material is the so-called optical phase change materials (OPCMs). As shown in Fig. 25(e), the OPCM-based metalens is optimized by a generic design methodology at 5.2-μm wavelength, and the corresponding focal length can be switched between 1.5 mm and 2 mm with the tuned amorphous and crystalline state[211]. Zoom metalenses can also be realized through polarization switching with meta-atoms carrying polarization-dependent phase shifts. Rao Fu *et al.* reported a step-zoom metalens with dual focal lengths based on double-sided polarization-dependent metasurfaces[212]. By carefully assigning the focal power and balancing the aberrations, the step-zoom metalens has a large FOV (±20°) and unchanged image plane. Furthermore, the above-mentioned manipulation methods can be incorporated together to implement more complex functions. For instance, Shumin Xiao's group developed and combined two types of TiO_2 metalenses with polarization independence and polarization sensitivity into a doublet[213]. As shown in Fig. 25(f), by controlling the polarization of incidence and the separation distance between the two metalenses, the doublet can show three distinct zoom effects, i.e., camera lens, compound microscope, and Galileo telescope.

5.2 3D Imaging

Most optical zoom imaging is suitable only for several discrete object planes, while for 3D scenes or objects, the depth information is of great importance as well. A light-field camera is one of the promising techniques to address this issue. Microlens arrays, as its vital inclusion, are utilized for acquisition of the intensity and direction of incoming light. However, the inherent aberrations, especially chromatic aberration, hinder the camera from obtaining high-quality images. Combining PB phase and dynamic phase, Ren Jie Lin *et al.* designed a polarization-dependent achromatic GaN metalens array (60 × 60) to capture light-field information, and reconstructed the depth of every object in a full-color scene [see Fig. 26(a)][198]. Combined with a differentiated and rendering algorithm, they also demonstrated edge detection from 1D to 3D with the light-field imaging system[214]. Moreover, this metalens array even enables a compact framework in generating entangled photons. Lin Li *et al.* successfully integrated a GaN metalens array (10 × 10) with a nonlinear crystal, and demonstrated a 100-path spontaneous parametric downconversion photon-pair source. 2D, 3D, and 4D two-photon path entanglement with different phases encoded by metalenses was demonstrated in experiments with fidelities of 98.4%, 96.6%, and 95.0%, respectively[215]. The same group even extended the metalens to work in the nonlinear optics and push the focusing function at the vacuum UV regime[216].

Recently, Qingbin Fan *et al.* demonstrated a nanophotonic light-field camera incorporating a spin-multiplexed bifocal metalens array [see Fig. 26(b)] capable of capturing light-field images over a record DOF ranging from centimeter to kilometer scale. Different from previous work[198], the metalens array is not designed with achromatism. Yet with a multi-scale convolutional-neural-network-based reconstruction algorithm, the camera can simultaneously enable macro and telephoto modes with high quality, correcting imaging aberrations in a snapshot[164]. As well known, longitudinal chromatic aberrations will undoubtedly blur images. In contrast, transverse chromatic aberration, with images of different wavelengths being spread out across the imaging plane, can greatly facilitate the extraction of spectral information. Xia Hua *et al.* combined the light-field technique with a transversely dispersive metalens array, and with only one snapshot, they demonstrated advanced 4D imaging with a 4 nm spectral resolution and near-diffraction-limit spatial resolution[217]. Different objects can be well imaged in terms of both spatial positions and colors. They also demonstrated an imaging case beyond the ability of the naked eye and light-field imaging with a trained spectrum reconstruction algorithm. As illustrated in Fig. 26(c), two kinds of materials, "I" shaped magenta chemical fabric cloth and "O" shaped water-color-painted paper, with close spectral peaks at

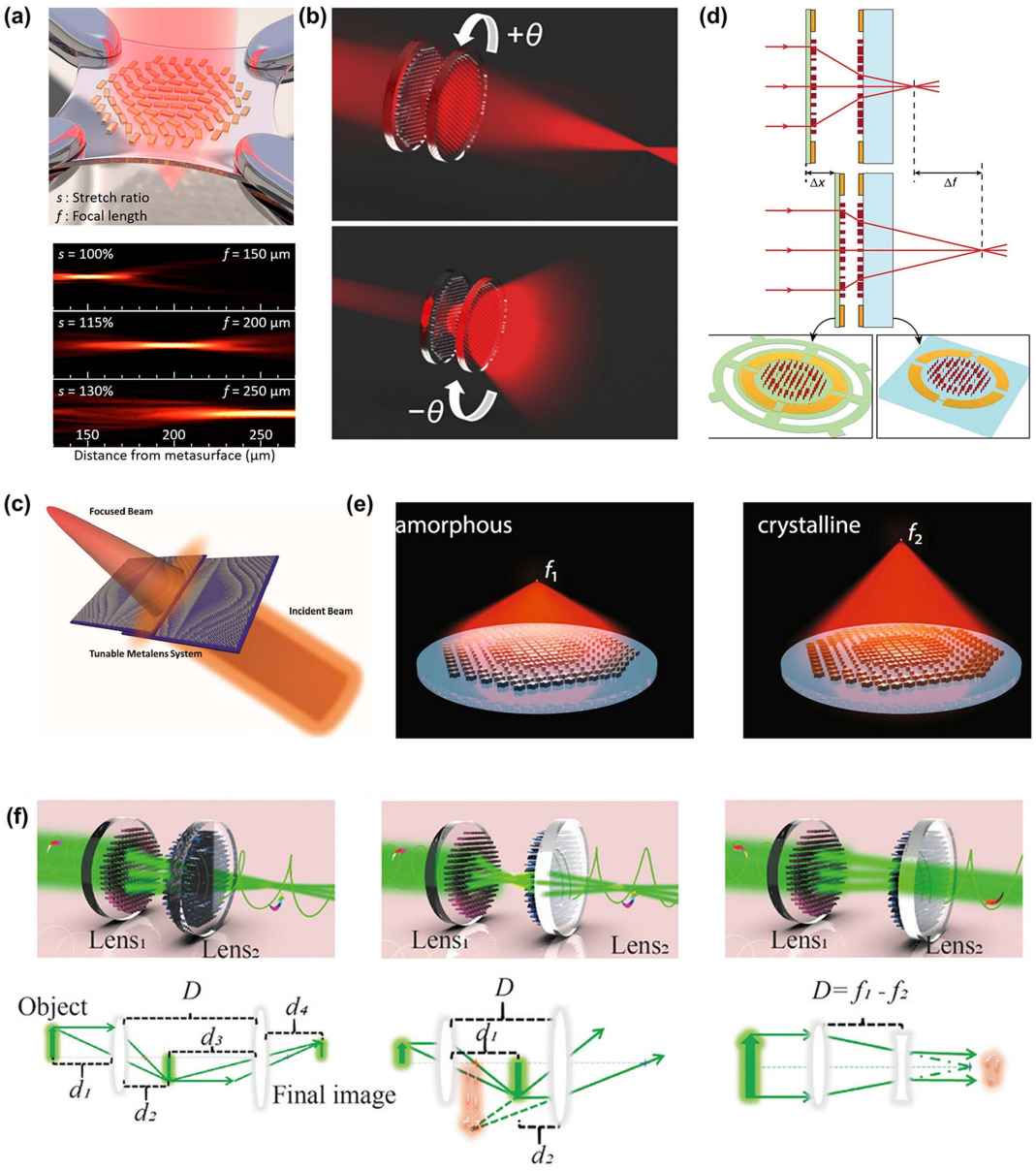

Fig. 25 Zoom metalens. (a) Tunable metalens on a stretchable substrate and its experimental zoom effect[206]. (b) Focal length tuning with rotational varifocal moiré metalens[207]. (c) Varifocal zoom Alvarez metalens with two cubic metasurface phase plates actuated laterally[209]. (d) MEMS-enabled tunable metalens doublets[210]. (e) Reconfigurable varifocal metalens with optical phase change material[211]. (f) Metalens doublet with functions including camera lens, compound microscope, and Galileo telescope enabled by polarization and distance manipulation[213].

618 nm and 626 nm can be distinguished evidently using their methods.

Despite the achievements of light-field imaging, there is still a trade-off between spatial and angular resolutions, which are in positive correlation with the spatial density of the lens array and the aperture of each lens, respectively. To mitigate this issue, Min-Kyu Park *et al.* proposed a virtual-moving metalens array based on a multifunctional dielectric metasurface. By tailoring the incident polarization, the sampling position can be laterally shifted without physical movement, and thus, a fourfold enhanced spatial resolution can be achieved through algorithms without sacrificing the angular resolution[218].

Nature provides various intriguing solutions to depth sensing. The above-mentioned light-field technique is actually similar to the compound eyes of insects. Inspired by the jumping spider, Qi Guo *et al.* also introduced a compact depth sensor combined with metalens optics. As illustrated in Fig. 26(d), the metalens splits the light that crosses an aperture and simultaneously forms two differently defocused images at distinct regions of the photosensor[219]. The distance can be decoded from these images with relatively little computation, and a system that deploys a 3-mm-diameter metalens to measure depth over a 10-cm distance range was demonstrated for proof of concept. Another method for 3D imaging based on a single metalens

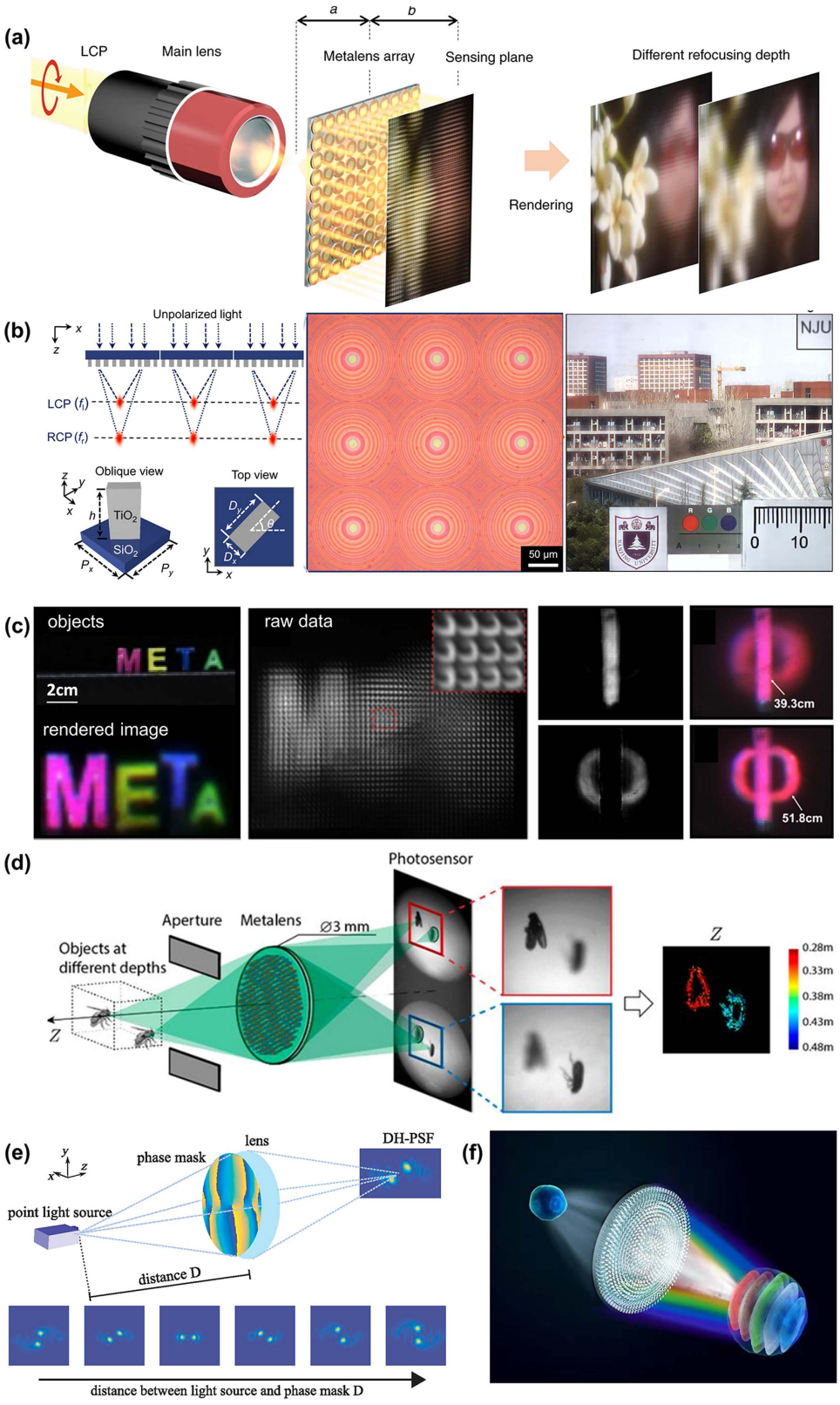

Fig. 26 3D imaging. (a) Light-field imaging with GaN metalens array and rendered full-color images[198]. (b) Light-field camera with extreme depth of field enabled by spin-multiplexed bifocal metalens array[164]. (c) Ultra-compact snapshot spectral light-field imaging[217]. (d) The metalens depth sensor estimates depth through defocused images by mimicking the jumping spider[219]. (e) Metasurface with engineered point spread function for distance measurements and three-dimensional imaging[220]. (f) Spectral tomographic imaging with aplanatic metalens[132].

was also proposed by Chunqi Jin *et al.* They designed a Huygens metasurface with a phase mask implementing a rotating PSF, and encoded the depth information from the shifted distance in the images [see Fig. 26(e)][220].

Tomography is an informative imaging modality in the biomedical domain, in which mechanical scanning is usually implemented for the acquisition of images with different depths. Chen Chen *et al.* utilized the large diffractive chromatic dispersion of the metalens to access spectral focus tuning without mechanical movement [see Fig. 26(f)][132]. They designed and fabricated an aplanatic GaN metalens with NA = 0.78, ensuring high resolutions both transversely and longitudinally. Microscopic tomography of frog egg cells was demonstrated, and from the clear evolution of the defocus–focus–defocus process, one can clearly distinguish the depths of the cell membrane and nucleus.

5.3 Polarization Imaging

Metalenses with wavefront engineering together with polarization manipulation not only enrich the functionalities of metasurface devices, but also benefit image quality with polarization analysis and decompress the burden of auxiliary optical elements. The widely designed PB-phase-based metalens actually acts as a half-wave plate, and with a related polarization analyzer, it can obtain image quality superior to lenses without polarization modulation[132]. Similarly, Chen Chen *et al.* proposed a highly efficient metalens concurrently acting as a quarter-wave plate[221], as shown in Fig. 27(a). By combining the propagation phase and PB phase, the superposition of co-polarized and cross-polarized light can be controlled precisely, and arbitrary wave plates and more complex wave manipulation were demonstrated as well.

Moreover, polarization properties of scattered light during the imaging process can reveal some valuable information such as texture, orientation, and constituent materials[222]. Especially, for some biologically active compounds, the intrinsic handedness results in distinct imaging chiral properties. Mohammadreza Khorasaninejad *et al.* presented a multiplexed metalens based on PB phase that simultaneously forms two images with opposite helicity of an object within the same FOV, and mapped the circular dichroism of the exoskeleton of a chiral beetle for application demonstration [see Fig. 27(b)][223].

The Stokes vector $S = [S_0, S_1, S_2, S_3]$ is defined to determine the polarization of incoming light in a more general case, where $S_0 = I$, $S_1 = I_{0°} - I_{90°}$, $S_2 = I_{45°} - I_{135°}$, $S_3 = I_{\mathrm{RCP}} - I_{\mathrm{LCP}}$, I is the total intensity, $I_{0°}$, $I_{90°}$, $I_{45°}$, and $I_{135°}$ are the intensity of light in linear polarization bases along 0°, 90°, 45°, 135°, respectively, and I_{RCP} and I_{LCP} are the intensities of circularly polarized light. To measure the polarization state of light in a compact manner, Zhenyu Yang *et al.* proposed a generalized Hartmann–Shack array based on dielectric metalenses[224]. As shown in Fig. 27(c), each pixel of the array consists of six tailored polarization dependences [0°, 90°, 45°, 135°, RCP (right-handed circular polarization), LCP (left-handed circular polarization)]; the polarization state can thus be calculated through the measured focus amplitudes, and the focus shifts can also indicate the phase gradients. Ehsan Arbabi *et al.* presented a more compact imaging polarimetry based on metalens arrays. As illustrated in Fig. 27(d), the superpixel of the polarization camera contains three metalenses, each designed with two orthogonal polarization dependences, e.g., 0° and 90°, 45° and 135°, and RCP and LCP[225]. Besides the pure polarization state, a complicated polarization object was also correctly imaged and analyzed with the metasurface polarimetry.

Most polarimetry works are based on determination of the full-Stokes vector, which necessitates at least four (normally six) individual measurements, and it undoubtedly results in limited efficiency and spatial resolution. To address this issue, Noah A. Rubin *et al.* reported a new strategy for a compact, snapshot, full-Stokes polarization imaging system with no specially patterned camera pixels. They introduced matrix Fourier optics and developed an optimization scheme to design the diffraction orders as polarizers for an arbitrarily selected set of polarization states. By analyzing the intensity of light on a set of diffraction orders, the polarization of the imaging scene can be reconstructed readily. They also packaged the imaging system into a practical, portable prototype with adjustable focus, as shown on the left of Fig. 27(e)[226]. Different from traditional intensity images, the polarization imaging of 3D glasses, a stressed laser-cut acrylic piece, and an injection-molded plastic part shows fruitful properties [right panel in Fig. 27(e)] indicating powerful applications in machine vision and other areas.

5.4 Microscopy Applications with Enhanced Functionalities

In the application of microscopes, super-resolution is undoubtedly the ultimate goal, and it has been significantly promoted by electronic microscopes [i.e., scanning electron microscope (SEM) and transmission electron microscope (TEM)] and luminescence optical microscopes. However, in principle, the superlens based on NIM should be the revolutionary solution as intensively discussed in Section 2. Although incapable of achieving super-resolution imaging, ultrathin, lightweight, and multi-functional metalenses show unlimited potential in compact and miniature imaging systems. There has been much progress towards the compacted microscopes implemented by incorporation with CMOS chips[142,143,227].

It is well known that microscope imaging cannot reach a high resolution and large FOV simultaneously due to the constraint from the space–bandwidth product. A lens array provides an alternative solution to break the constraint to cover a large imaging area and enlarge the effective FOV. Unlike light-field imaging with a micro-lens array that works in telescope or landscape imaging modes[164,198], this wide-field microscope should work in an equal-size (4f) imaging mode with the scene area rightly mapped to the image plane and recorded by a CMOS detector. However, conventional micro-lens arrays cannot provide a complete image by stitching sub-images, because the arrangement of refractive lens arrays always has blind areas at the boundaries of lenses, which makes a complete stitching image impossible. Interestingly, Tao Li's group from Nanjing University proposed a polarization multiplexed silicon metalens array with two sets of focusing phase profiles intersecting each other for two orthogonal circular polarizations [see Fig. 28(a)]. Based on this, two groups of sub-images can be obtained to compensate for the blind areas of each other and provide a complete wide-field microscope image after a certain stitching process [see Figs. 28(b) and 28(c)][142]. More recently, Xin Ye *et al.* from the same group further expanded the metalens array (made of SiN_x) from 6×6 to 16×16, which covers a whole image area to 4 mm × 4 mm [see Figs. 28(d) and 28(e)] and changes the working wavelength to blue light ($\lambda = 470$ nm)[227]. More importantly, they adopted a co- and cross-polarization

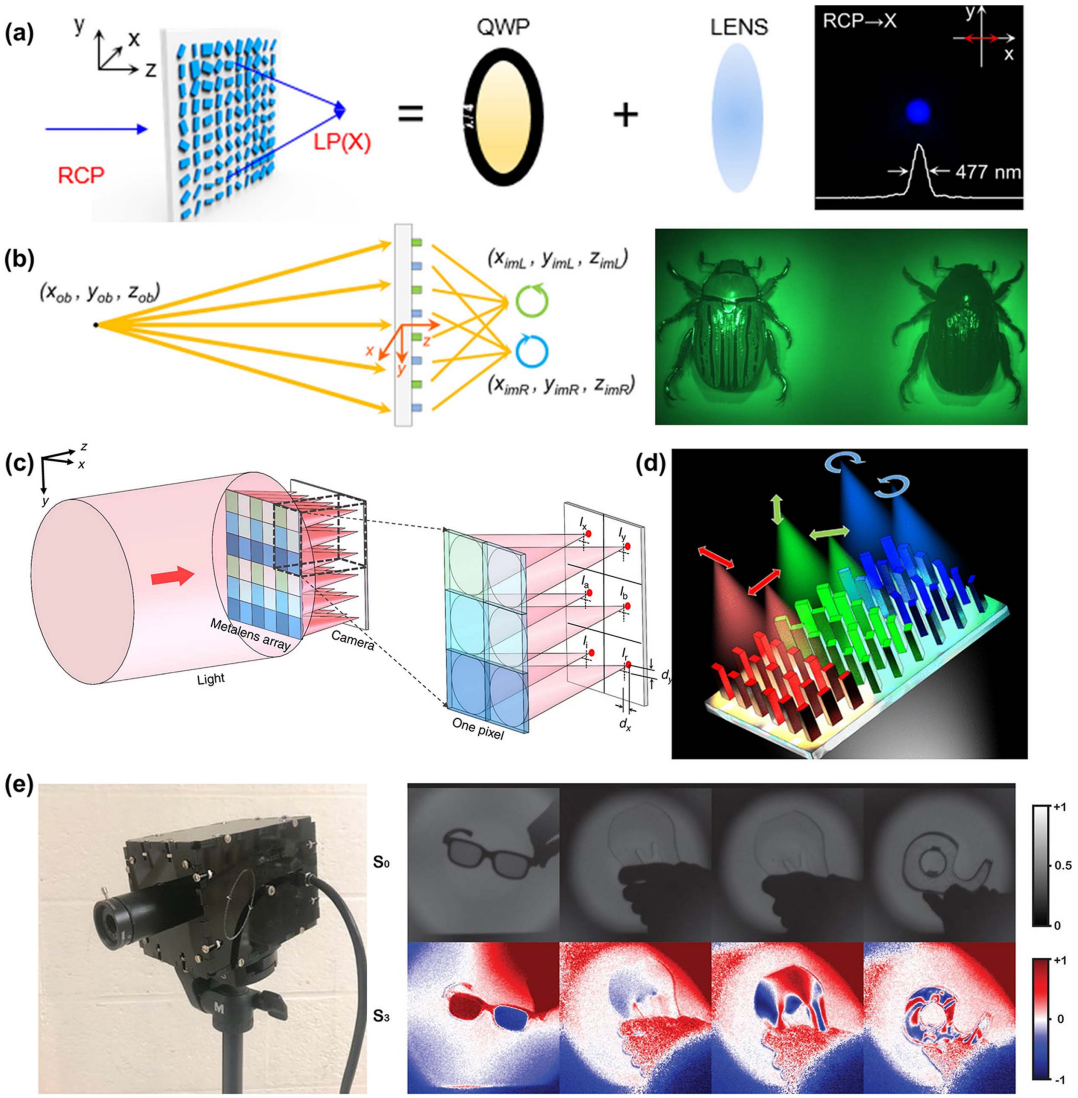

Fig. 27 Polarization imaging. (a) Metalens concurrently acting as a quarter-wave plate[221]. (b) Chiral imaging with a metalens[223]. (c) Generalized Hartmann–Shack array of dielectric metalens sub-arrays for polarimetric beam profiling[224]. (d) Polarimetric imaging based on polarization multiplexed metalenses[225]. (e) Portable prototype of the polarization imaging systems enabled by matrix Fourier optics, and the exemplified imaging results[226].

multiplexed metalens array that enables a fixed polarizer [termed CPF in Fig. 28(d)] to work embedded in an encapsulated imaging device. It therefore greatly improves the image quality in both contrast and SNR. Finally, a compact meta-microscope was implemented with a very small size [3 cm × 3.5 cm × 4 cm, see Fig. 28(f)] that enables a wide field (4 mm × 4 mm) and relatively high resolution (1.74 μm). As a result, Fig. 28(g) shows the wide-field microscope image of a bio-specimen obtained by the meta-microscope, where the blue boxed area is the FOV obtained by a commercial Olympus microscope with the same resolution, and insets (g1) and (g2) are zoom images from the meta-microscope and Olympus one, respectively, showing almost identical image quality.

Endoscope imaging is another important scenario that is in high demand of miniaturization. In particular, endoscopic optical coherence tomography (OCT) is a promising tool for diagnosis and detection, but still with shortcomings (mostly the trade-off between transverse resolution and DOF), limiting applications in routine clinical practice. Harvard University and Harvard Medical School together developed a nano-optic endoscope integrated with a metalens for high-resolution OCT *in vivo*. As shown in Fig. 29(a), the metalens, fiber, and prism are assembled with precise alignment at the distal end of the catheter[228]. With tailored chromatic dispersion, the metalens enables the maintenance of high-resolution imaging significantly beyond the Rayleigh range of incident light and thus brings in the large DOF. Compared with images of a swine airway using a ball lens catheter, the proposed nano-optic endoscope shows superior image quality. In addition to the capability of high lateral resolution, the wide FOV of the microscope objective is also essential to the endoscope. Jianwen Dong's group proposed a meta-objective composed of two cascaded metalenses mounted on both sides of a 500-μm-thick silica film with diameters of 400 μm and 180 μm[229]. The lateral resolution reaches as high

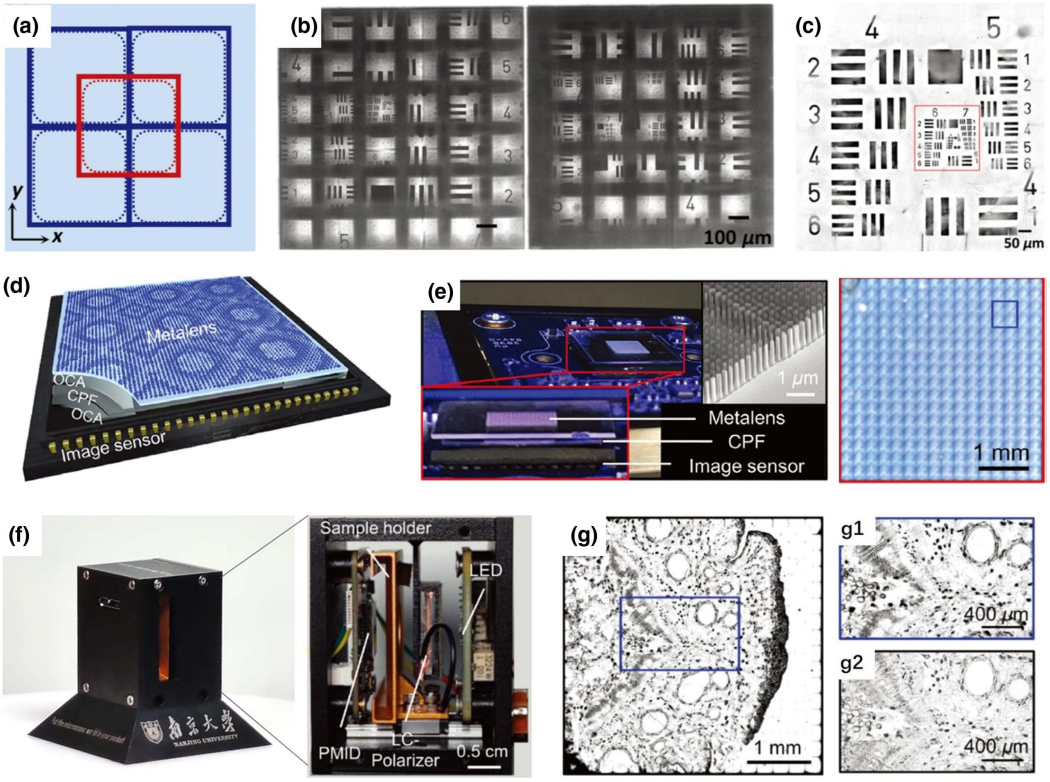

Fig. 28 Meta-microscope implemented by polarization multiplexed metalens array. (a) Two-polarization multiplexed focusing phase design in four lens units. (b) Two groups of sub-images captured by the integrated imaging system with respect LCP and RCP light illuminations. (c) Stitched large FOV (1.2 mm × 1.2 mm) microscope image of resolution chart with resolution of 1.74 μm[142]. (d) Schematic of SiN_x metalens array covering the whole CMOS. (e) Photograph of metalens imaging chip and (f) implemented meta-microscope with a total size of 3 cm × 3.5 cm × 4 cm. (g) Large FOV (4 mm × 4 mm) microscope image with comparison to that obtained through a commercial Olympus microscope (blue boxed area is FOV); insets (g1) and (g2) display the zoom-in images from the meta-microscope and Olympus, respectively[227].

as 775 nm in such a naked meta-objective, with monochromatic aberration correction in a 125-μm full FOV and near-diffraction-limit imaging. The single cell contour of biological tissue can be clearly observed when combined with a fiber bundle microscope system.

Normally, there exists a trade-off between lateral resolution and the DOF. With the rapid spread of tightly confined light due to diffraction, high-resolution optical imaging is hardly preserved in a relatively large depth range. To address the issue, Masoud Pahlevaninezhad *et al.* showed that a particular disposition of light illumination and collection paths can liberate optical imaging from the restrictions imposed by diffraction[230]. As shown in Fig. 29(b), the special design based on metasurfaces can decouple the lateral resolution from the DOF by establishing a one-to-one correspondence (bijection) along a focal line between incident and collected light. Implementing this approach in OCT, they further demonstrated tissue imaging at a wavelength of 1.3 μm with ~3.2 μm lateral resolution, maintained nearly intact over a 1.25-mm DOF. This method, termed bijective illumination collection imaging, requires no additional acquisition or computational burden, and might be adapted across various existing imaging modalities.

Phase contrast imaging is a powerful technique to observe non-labeled biological samples with small variations in refractive index or thickness. Developing a relevant miniature and low-cost system is attractive for various applications. Pengcheng Huo *et al.* demonstrated a Fourier transform setup incorporating a spin-decoupled metasurface for switching between bright-field imaging and phase contrast imaging modes [see Fig. 29(c)][231]. With 2D spatial differentiation capability, the system can achieve isotropic edge detection with samples such as resolution test charts and undyed onion epidermal cells. Junxiao Zhou *et al.* also demonstrated broadband 2D spatial differentiation and high-contrast edge imaging across the whole visible spectrum for both intensity and phase objects by inserting the metasurface into a commercial optical microscope[232]. Furthermore, Youngjin Kim *et al.* demonstrated a single metalens without a Fourier transform setup for more compact phase contrast imaging[233]. As illustrated in Fig. 29(d), the metalens in which the phase profile is a sum of the hyperbolic phase and spiral phase (topological charge =1), termed spiral metalens, can also perform 2D isotropic edge-enhanced imaging of various samples. Recently, a single metalens with an illumination-intensity-dependent computational function has been proposed and experimentally demonstrated. The metalens consists of nanoantenna structures with a static geometric phase and nonlinear metallic quantum well layer; it can offer an intensity-dependent dynamic phase, resulting in

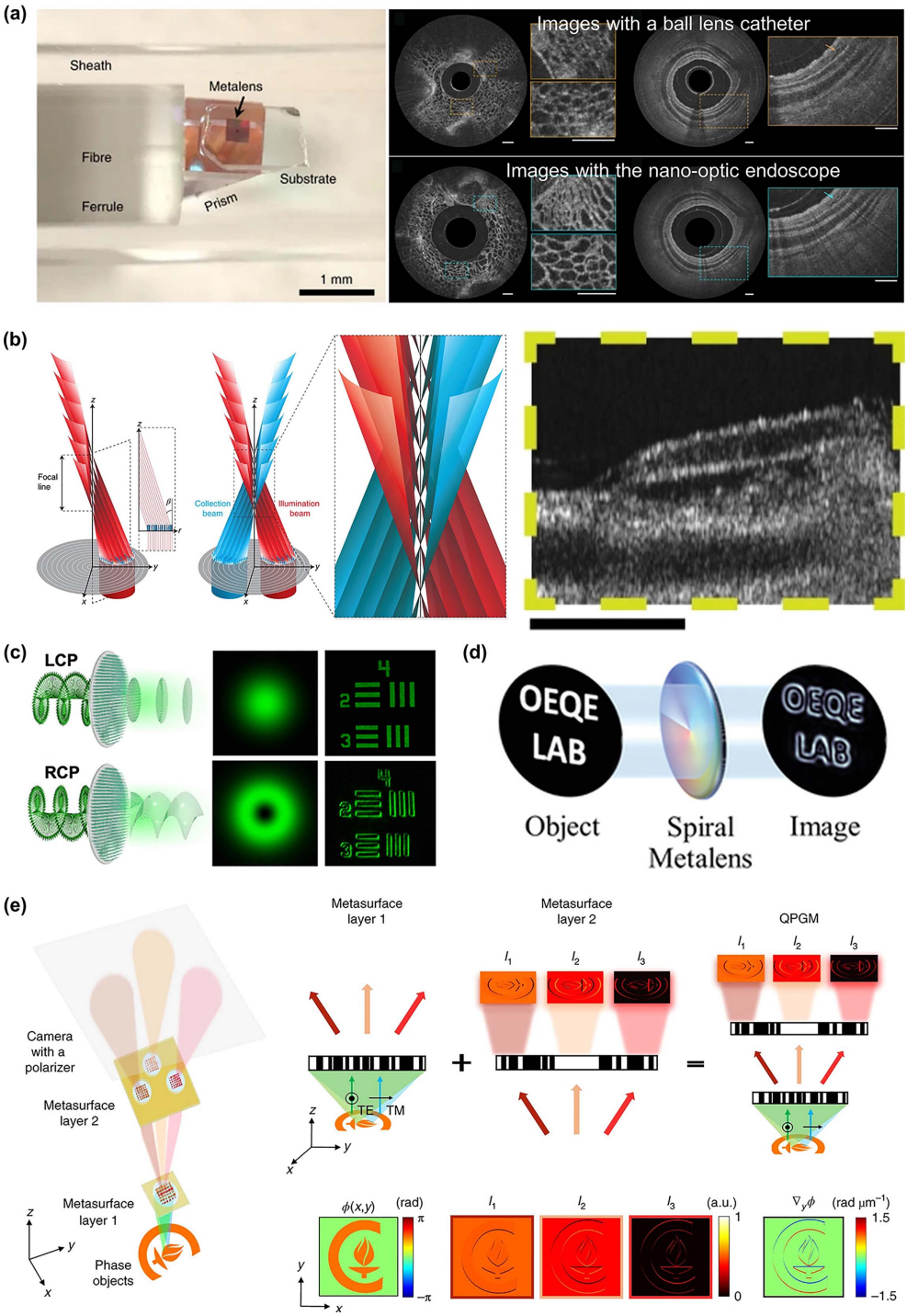

Fig. 29 Enhanced microscopy imaging. (a) Nano-optic endoscope for high-resolution optical coherence tomography *in vivo*[228]. (b) Bijective illumination collection imaging based on metasurfaces and corresponding tissue imaging results[230]. (c) Fourier transform setup for switching between bright-field imaging and phase contrast imaging modes[231]. (d) Spiral metalens for phase contrast imaging[233]. (e) Single-shot quantitative phase gradient microscopy using a system of multifunctional metasurfaces[235].

a continuously tunable coherent transfer function. With high-intensity illumination, the metalens presents an edge-detection image, while diffracting full images with low-intensity lighting[234]. Phase contrast imaging can capture only qualitative phase information, while acquiring quantitative phase data is a rapidly growing demand for more sophisticated analysis. Inspired by a classical differential interference contrast microscope (DIC), Andrei Faraon's group proposed a miniaturized quantitative phase gradient microscope (QPGM) based on two dielectric metasurface layers [see Fig. 29(e)][235]. Combining

both polarization and spatial multiplexing methods, the cascaded metasurfaces can simultaneously capture three DIC images to generate a quantitative phase gradient image in a single shot. The demonstrated system is of the order of 1 mm^3, and the phase gradient sensitivity is better than 92.3 mrad μm^{-1}. All these results showcase the potential of metalenses for developing miniaturized microscopy systems with enhanced functions.

5.5 Landscape Imaging

In most previous metalens imaging, we find it always suffers from small apertures (though new progress has been made for imaging without a need of achromatism). To develop a white-light landscape camera, a macroscopic (millimeter to centimeter sizes) lens is necessary, as a larger aperture determines a larger FOV, as shown in Fig. 30(a)[188]. To be more specific, white-light landscape imaging through two achromatic metalenses with diameters no more than 500 μm is first shown in Figs. 30(b) and 30(c)[130,163]. It is clear that the imaging performance is high at the center of the picture, while there exist obvious aberrations at the edge, even after the imaging process. As a contrast, the images taken from the AMDL with diameter nearly equal to 1 mm have fewer aberrations in a larger FOV, as shown in Fig. 30(d)[201]. By further increasing the diameter to 8 mm or 23.4 mm and incorporating the AMDL with an advanced image processing algorithm, such as deep learning, imaging performance can be improved to a level nearly on par with that of the lens modules in cell phones, as shown in Figs. 30(e) and 30(f)[182,190]. Therefore, the AMDL shows its advantages over metalenses in this area.

Imaging systems with folded/compressed working distances. Metalenses are viewed to have great potential for miniaturizing imaging systems due to the ultrathin and ultralight features. However, in most imaging systems, lenses occupy a very limited volume, while the space between lenses or the lens and detector takes up the most room in imaging systems. Folding or compressing the space/working distance is crucial to obtain the utmost miniaturization of imaging systems, especially in landscape and telescope applications. To address this issue, Cheng Guo *et al.* numerically demonstrated a nonlocal flat optic operating directly in the momentum domain to substitute free space. They derived the general criteria for a device to replace

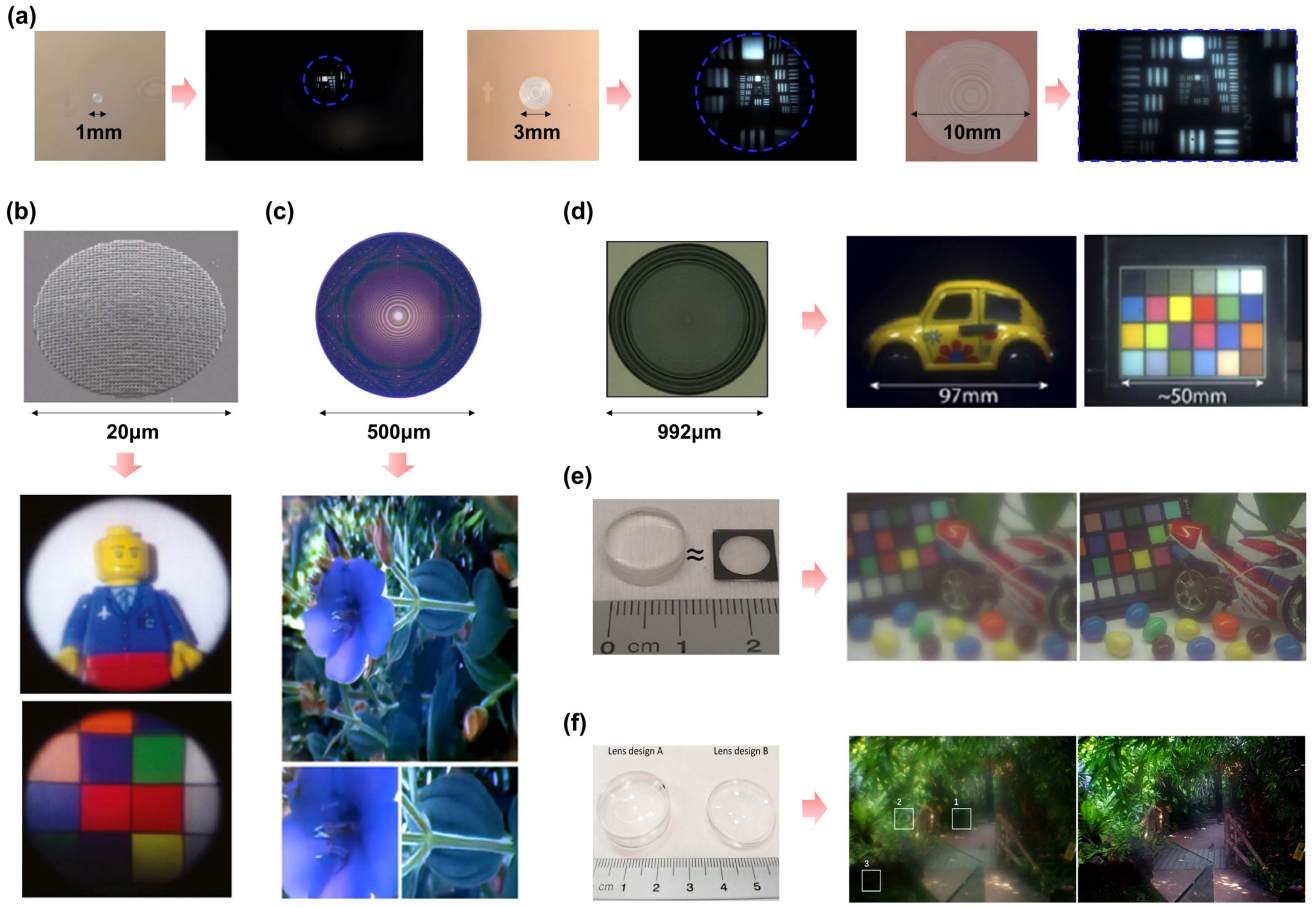

Fig. 30 (a) Three AMDLs with different diameters and the image of USAF taken from them with the same magnification. The closed blue dashed lines denote the FOV in each figure[188]. (b) Achromatic metalens with diameter equal to 20 μm and the images taken from it[130]. (c) Achromatic metalens with diameter equal to 500 μm and the images taken from it (after image processing)[163]. (d) AMDL with diameter equal to 992 μm and the images taken from it[201]. (e) AMDL with diameter equal to 8 mm and the images (before and after imaging process) taken from it[190]. (f) MDL with diameter equal to 23.4 mm and the images (before and after imaging process) taken from it[182].

free space and provided two concrete designs of such a device utilizing photonic Fano resonances[236]. Soon after, Orad Reshef *et al*. also proposed an optic to replace space, termed spaceplate [237]. As shown in Fig. 31(a), the spaceplate occupies a physical thickness of d while propagating light for an effective length of $d_{\text{eff}} > d$. The spaceplate relies on the momentum-dependent phase as

$$\varphi_{\text{SP}}(k_x, k_y, d_{\text{eff}}) = d_{\text{eff}}\left(|\vec{k}|^2 - k_x^2 - k_y^2\right)^{1/2}. \tag{30}$$

Such a phase response is called a nonlocal response, which is different from the position-dependent response (local response). It cannot redirect the angle of a light ray and has no optical power. Two types of spaceplates are proposed to shorten the distance from the lens to the focus: one is multilayer metamaterial, and the other is a uniaxial birefringent medium. Figure 31(a) also illustrates the images of a lens with and without a uniaxial spaceplate, indicating effective space compression. This design strategy has aroused great interest[238] and opens an avenue for ultrathin monolithic cameras.

In addition to the nonlocal solution, the pancake optic, which is usually composed of a beam splitter (BS) and a reflective polarizer (RP), also provides possibilities to fold the propagating space. However, due to the two interactions with the BS, the overall light efficiency is at most 25%. To address this issue, recently Chen Chen *et al.* proposed a pancake metalens that can fold the optical path almost at will while without light waste, in principle[239] [see Fig. 31(c)]. The working principle can be understood as first squeezing the imaging system with multiple k-vector manipulations, and then folding the squeezed optical path to a more compact lens system [Fig. 31(b)]. The pancake metalens is based on a meta-cavity consisting of a spin-dependent bifacial metasurface and a mirror. Imparting the bifacial metasurface with a specifically designed phase, they demonstrated a pancake metalens with on-demand (e.g., 2/3 and 4/5) reduction of imaging distance and relatively good imaging performance. Figure 31(d) shows the experimental setup and the imaging results of a pancake metalens (2/3 reduction of imaging distance) and its comparison with a normal metalens. This pancake meta-optics framework provides a new possible solution to the miniaturization of imaging systems and would provide insights for other meta-device applications.

5.6 AR/VR Application

In recent years, AR and VR have gained increasing attention in both academia and industry, and have experienced enormous growth. Comfortable wear of AR/VR headsets is an essential requirement for commercial applications, and is in high demand of a compact form factor. Planar optics including conventional diffractive optics and meta optics hold great promise to manipulate light and tackle this challenge[240,241]. Researchers have been developing various systems based on metalenses to address these concepts. For instance, Byoungho Lee *et al.* incorporated a see-through metalens to an AR near-eye display with an ultrawide FOV, full-color imaging, high resolution, and sufficiently large eyebox[242]. By virtue of the anisotropic optical response, the PB-phase-based see-through metalens can simultaneously serve as an imaging lens for virtual information and as transparent glass through which a real-world scene is viewed [see Fig. 32(a)]. The chromatic aberration of the metalens can be corrected by varying the imaging position with the wavelength using three dichroic mirrors. Based on nanoimprint technology, the metalens has a diameter of 20 mm and NA of 0.61, showing feasibility for practical mass-production.

To further reduce the form factor, the same research group proposed a holographic AR near-eye display using a PB phase eyepiece (PBPE) and a methodology to correct optical aberrations to discard other additional optical components[243]. The PBPE consists of two PB phase metalenses, a linear polarizer, and a quarter-wave plate [see Fig. 32(b)]. It acts as a convex lens with effective focal length $f/2$ for RCP light, and becomes a transparent plate for LCP light. The monochromatic aberration is corrected with computer-generated hologram calculation, and the chromatic aberration is corrected by floating the holographic images at different depths depending on the wavelength. As shown in Fig. 32(b), the observed images present quality superior to that without correction.

As seen above, chromatic aberration is one of the main challenges hindering metalens application in AR/VR. Many pioneering works have been reported to solve the problem. Different from the methods proposed by Byoungho Lee's group, Federico Capasso's group demonstrated a millimeter-scale diameter, high-NA, and RGB-achromatic metalens for direct utilization in AR/VR near-eye displays [see Fig. 32(c)][244]. By exploiting constructive interference of light from multiple zones and dispersion engineering, the metalens can achieve diffraction-limited achromatic focusing of the primary colors. It opens a new paradigm of metalens design with a combination of forward and inverse design methods. The excellent mixture of a real-word scene and a floating image indicates the limitless potential of metalenses in the field more than AR/VR.

It is worth noting that most of the above-mentioned metasurfaces modulate the optical wavefront through the independent response of each meta-atom, which can be categorized as local metasurfaces, although it can shape a wavefront at multiple selected wavelengths, but inevitably modifies light across the spectrum. As another category, nonlocal metasurfaces[245–247] tailor the wavefront through collective modes. It can produce great frequency selectivity based on high-quality-factor (Q factor) modes[248,249]. Bound states in the continuum (BICs) are prototypical states with infinite radiative Q factors despite having momentum matched to free space[250]. Applying a perturbation to break in-plane inversion symmetry of meta-atoms may create a quasi-BIC (q-BIC) that is leaky and excitable from spatial light[251]. The Q factor of q-BICs can be controlled by the strength of the perturbation, enabling simultaneous light confinement in both space and time. Encoding q-BICs with spatially varying PB phase, Nanfang Yu's group demonstrated nonlocal metasurfaces that can offer both spatial and spectral control of light, for instance, realizing metalenses focusing exclusively over a narrowband resonance while leaving off-resonant frequencies unaffected[252]. As shown in Fig. 32(d), a doublet with a single-function metasurface operating at the green wavelength and a dual-function metasurface operating at red and blue wavelengths can serve as an optical see-through lens in an AR headset. It reflects contextual information to the viewer's eye at selected narrowband wavelengths while permitting an unobstructed broadband view of the real world. Such a design strategy does not require extra polarizers or BSs, and has great potential in AR and other transparent display applications.

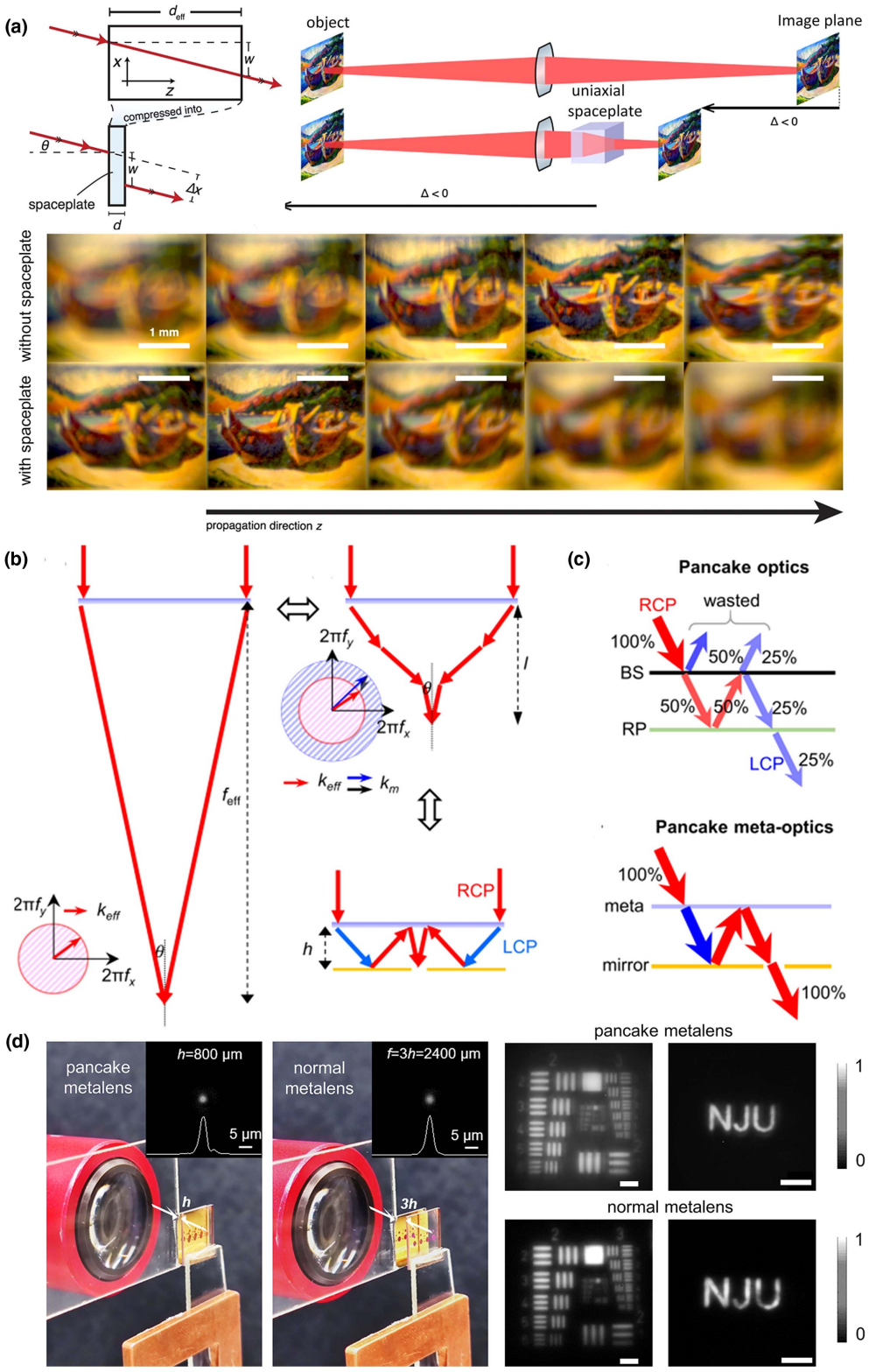

Fig. 31 Miniaturization of imaging systems by folding/compressing the working distance. (a) Spaceplate to compress the propagation distance and its imaging results combined with a lens[237]. (b) Operating principle of a pancake metalens. (c) Comparison between pancake optics and pancake meta-optics. (d) Comparison of the experimental setup and imaging results of pancake metalens and normal metalens[239].

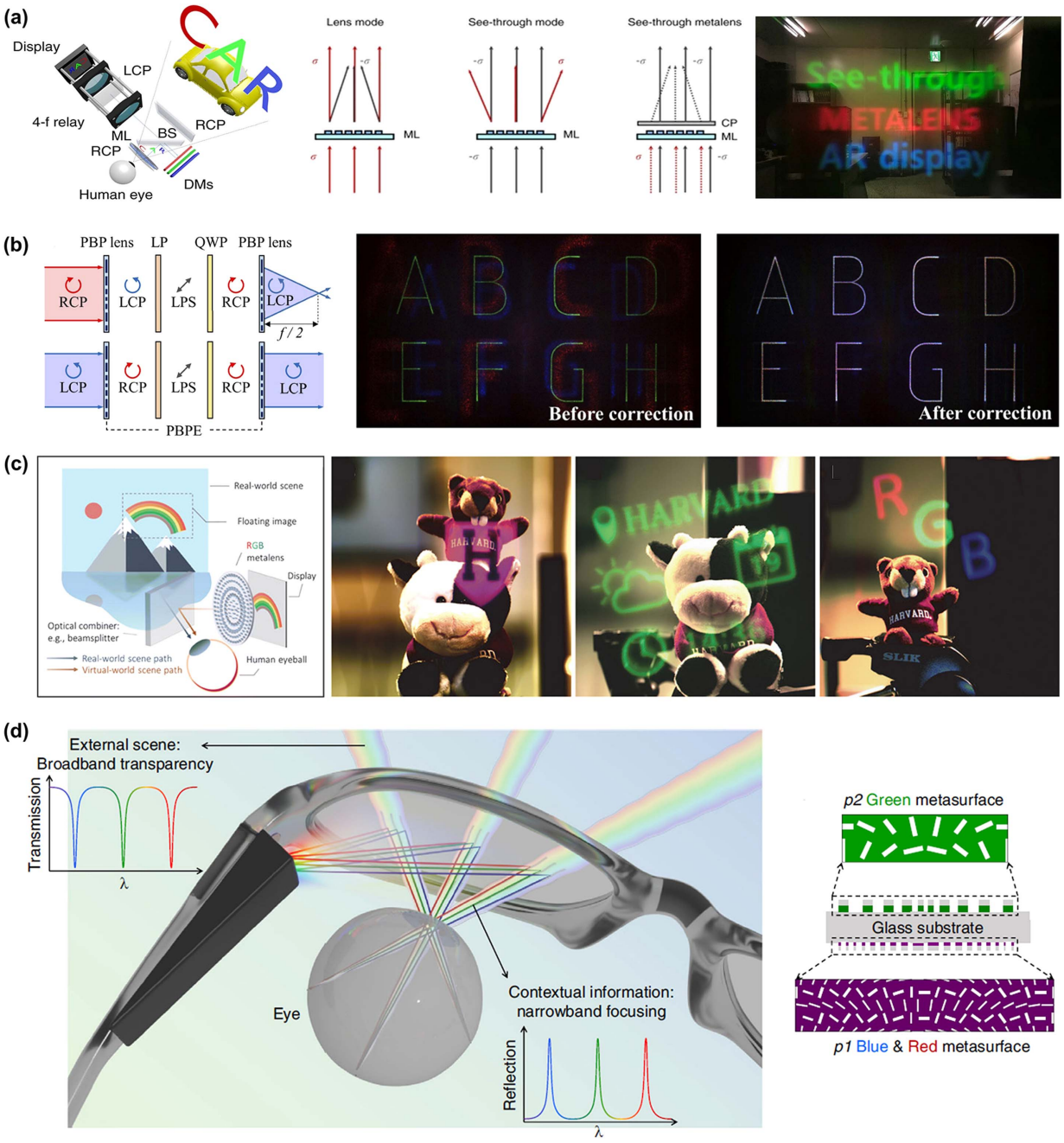

Fig. 32 Metalenses with AR/VR applications. (a) See-through near-eye display with a PB phase based metalens[242]; the left is the illustration of the prototype, the middle is the principle of the see-through metalens, and the right is the experimental AR image. (b) Aberration-corrected full-color holographic augmented reality near-eye display using a Pancharatnam–Berry phase lens[243]. (c) Full-color VR/AR display with RGB-achromatic metalens[244]. (d) Illustration of an AR headset with multifunctional nonlocal metasurfaces as optical see-through lenses[252].

6 Conclusion and Perspectives

During the past two decades, we have witnessed tremendous conceptual efforts associated with micro/nano optics and photonics researches, among which new concepts for revolutionary imaging functions and techniques have emerged, such as negative index metamaterials, superlenses, hyperlenses, and metalenses. In fact, each part of the text has been more or less addressed by other review papers, for example, Refs. [31,49,82,83,253–265]. This paper tries to provide an overall and historic view on this interesting and valuable progress from the perspective of imaging technology, where the intrinsic logical routes are worth revisiting carefully. The development context will have great inspiration for those carrying out the next stage of research.

Benefiting from the advances of micro/nano-fabrications, subwavelength artificial structures enabled the emergence of new conceptual metamaterials in the new century. They have significantly renewed recognition of the functional materials that were usually limited by their chemical compositions in the past, and opened a new avenue to design wave-functional materials (not limited in optics) almost at will. The superlens originating from negative refraction has excited worldwide research interest according to a revolutionary working principle, even bringing in a new era of super-resolution. Unfortunately, the development of engineering steps is far behind the advanced theory, resulting in big challenges for mass application. Even so, its derivative techniques (such as SPP nanolithography and plasmonic sensing) are still forging ahead toward applications[205,266], and some new developments are cast in related fields (e.g., compact photonic integrations[61]) and novel physics platforms[63].

In the optical regime, ultrathin metalenses recovered research vitality towards practical applications, because they circumvent the two major problems of extreme difficulty in nanofabrication and huge propagating loss of light inside bulk metamaterials. Nevertheless, to further reduce the loss, the constitution of metalens/metasurface material has been gradually changed from initial metal to dielectric, though it increases fabrication challenges to some extent. This review summarized part of the major progress of the metalens from the design principle, imaging performances, and possible and suitable applications scenarios. It can be concluded that the metalens holds two major advantages in compactness and multifunction, although its comprehensive performances are still inferior to those of traditional refraction lenses and compound lenses. However, both advantages favor very much the current developments of optical devices to ultra-compact and highly integratable. Therefore, the pressing matter of the moment is to improve the comprehensive performance of metalenses to a commercially acceptable level. Extensive efforts and detailed progress have been addressed in this review. Besides many new functions such as polarized imaging and differential imaging, high efficiency together with broadband achromatism and aberration-free images is still mainstream for imaging applications.

The development of MDL explicitly interpreted in Section 4 is indeed a parallel strategy to achieve light-thin and multifunctional flat lenses. In principle, the metalens is implemented by structuring a flat lens in the transverse dimension, specifically, the detailed sizes of nano-posts to control the resonance/guided modes to tune the resonance and propagation phases, and the rotation of units to tune the geometry phase. Correspondingly, the freeform MDL is intended to control the propagation phase in the longitudinal dimension by sophisticated diffractive ring heights with respect to certain FoMs. It has been well demonstrated that freeform MDL has many advantages in realizing large-sized and broadband achromatic flat lenses. A reasonable fact is that MDL usually can be fabricated with much higher height variations of each ring, which gives rise to the huge compensation phase as required in large-scale achromatic lenses, for example, the development of more than 10–15 μm maximum height rings, which is almost inaccessible for metalens units currently. Moreover, it is more feasible in large-scale and mass-production for a great reduction in structural data due to radial symmetry, although several methods have been proposed for data compression in mass-fabrication[173]. As a short summary, Table 2 intuitively shows the characteristics of the superlens, hyperlens, metalens, and MDL for imaging, which may be helpful for readers to quickly catch the major information of each type of these lenses.

To point out the major trends in lens development for revolutionary applications based on meta-designs, we provide several clues. The first is extending the design dimensions of metalens/MDL to introduce DoFs to further manipulate the spatial and frequency dispersion to access the highly efficient achromatic and large-FOV singlet flat lens. In this regard, the MDL could be considered as one step towards the longitudinal direction. Further opportunities still lie in a multilayered metalens/MDL, where interlayer coupling can be managed as a new DoF. Of course in a planar dimension, topological optimization can be widely adopted to generate non-periodic structures that can be considered a renewed transverse dimension. Second, new frameworks of the current metalens/MDL for particular application scenarios should be further explored, which can obtain equivalent high performances far beyond conventional lenses, e.g., by a metalens array for a large DOF[164,198], FOV[142,227], and view angle[143]. In this regard, to find appropriate application scenarios is more important than purely improving the comprehensive imaging performance of lenses, while the unique features of metalenses are exploited (such as polarization multiplexing, large dispersion for spectral resolution) for particular purposes. The third is the deep involvement of advanced

Table 2 Characteristics of Superlens, Hyperlens, Metalens, and MDL for Imaging.

	Superlens	Hyperlens	Metalens	MDL
Working principle	Evanescent wave amplification in bulk	Evanescent wave amplification in bulk	Propagation wave/phase reassemble	Propagation wave/ diffraction effect
Resolution	Super-resolution	Super-resolution	Diffraction limited	Diffraction limited
Imaging region	Near field	Near field/far field	Far field	Far field
Optical axis	None	None	Yes	Yes
Lens geometry	Flat	Flat/curved	Flat	Flat
Thickness	Tens of nm to microns	Tens of nm to microns	Tens of nm to microns	Microns to tens of microns
Constitutive materials	Metal	Metal/dielectric	Metal or dielectric	Dielectric
Unit cell	Meta-atom with negative ε or μ	Nanowire array or multilayered nanofilm	Meta-atom varies in shape, size, orientation	Diffraction ring varies in height

computational techniques. In fact, much recent impressive progress has demonstrated the important role of computational imaging processes[163,267]. There have been a wide range of these newly emerging and developing techniques, including topological optimization, inversion design, and deep learning based on various frameworks[268–271]. Especially, the neural-network-based algorithm has demonstrated its powerful capability in improving imaging quality. For example, the recent AR-oriented RGB achromatic metalens has efficiency of only less than 20%, which appears to work well for noise reduction[267]. Note that computational imaging itself has been a hot topic due to its advanced functionalities[272,273], which is out of the scope of this review. As a final perspective, more advanced manufacturing techniques are always in high pursuit. For instance, with mass-nanofabrication of meta nano-pillars with aspect ratios larger than 100:1 and maximum heights over 20 μm, the comprehensive imaging performances of a large-sized metalens is undoubtedly accessible. Another solution lies in the exploration of new quality optical materials with low loss, high refractive indices, ease of manufacturing, and tunability by external means. We have witnessed and are working in a great era opened by metamaterials, and we believe that there are tremendous revolutionary applications that will be enabled by meta-imaging sooner or later. With more and more involvement of industry, the revolution is beginning.

Acknowledgments

The authors acknowledge the financial support from the National Key R&D Program of China (2022YFA1404300) and National Natural Science Foundation of China (91850204, 92250304, 62288101). Tao Li acknowledges the support from Dengfeng Project B of Nanjing University.

References

1. E. Hecht, *Optics*, 4th edition (Addison Wesley, 2001).
2. M. Fernández-Suárez and A. Y. Ting, "Fluorescent probes for super-resolution imaging in living cells," *Nat. Rev. Mol. Cell Biol.* **9**, 929 (2008).
3. K. I. Willig *et al.*, "STED microscopy reveals that synaptotagmin remains clustered after synaptic vesicle exocytosis," *Nature* **440**, 935 (2006).
4. T. A. Klar and S. W. Hell, "Subdiffraction resolution in far-field fluorescence microscopy," *Opt. Lett.* **24**, 954 (1999).
5. G. H. Patterson and J. Lippincott-Schwartz, "A photoactivatable GFP for selective photolabeling of proteins and cells," *Science* **297**, 1873 (2002).
6. M. J. Rust, M. Bates, and X. Zhuang, "Sub-diffraction-limit imaging by stochastic optical reconstruction microscopy (STORM)," *Nat. Methods* **3**, 793 (2006).
7. J. N. Mait, G. W. Euliss, and R. A. Athale, "Computational imaging," *Adv. Opt. Photonics* **10**, 409 (2018).
8. A. M. Maiden and J. M. Rodenburg, "An improved ptychographical phase retrieval algorithm for diffractive imaging," *Ultramicroscopy* **109**, 1256 (2009).
9. M. T. Alonso, P. López-Dekker, and J. J. Mallorquí, "A novel strategy for radar imaging based on compressive sensing," *IEEE Trans. Geosci. Remote Sens.* **48**, 4285 (2010).
10. G. Zheng *et al.*, "Concept, implementations and applications of Fourier ptychography," *Nat. Rev. Phys.* **3**, 207 (2021).
11. Y. Liu and X. Zhang, "Metamaterials: a new frontier of science and technology," *Chem. Soc. Rev.* **40**, 2494 (2011).
12. C. Enkrich *et al.*, "Magnetic metamaterials at telecommunication and visible frequencies," *Phys. Rev. Lett.* **95**, 203901 (2005).
13. H.-K. Yuan *et al.*, "A negative permeability material at red light," *Opt. Express* **15**, 1076 (2007).
14. R. A. Shelby, D. R. Smith, and S. Schultz, "Experimental verification of a negative index of refraction," *Science* **292**, 77 (2001).
15. V. M. Shalaev *et al.*, "Negative index of refraction in optical metamaterials," *Opt. Lett.* **30**, 3356 (2005).
16. G. Dolling *et al.*, "Negative-index metamaterial at 780 nm wavelength," *Opt. Lett.* **32**, 53 (2007).
17. J. B. Pendry, "Negative refraction makes a perfect lens," *Phys. Rev. Lett.* **85**, 3966 (2000).
18. J. Valentine *et al.*, "Three-dimensional optical metamaterial with a negative refractive index," *Nature* **455**, 376 (2008).
19. N. Fang *et al.*, "Sub-diffraction-limited optical imaging with a silver superlens," *Science* **308**, 534 (2005).
20. X. Zhang and Z. Liu, "Superlenses to overcome the diffraction limit," *Nat. Mater.* **7**, 435 (2008).
21. Z. Liu *et al.*, "Far-field optical hyperlens magnifying sub-diffraction-limited objects," *Science* **315**, 1686 (2007).
22. N. Yu *et al.*, "Light propagation with phase discontinuities: generalized laws of reflection and refraction," *Science* **334**, 333 (2011).
23. M. Khorasaninejad *et al.*, "Metalenses at visible wavelengths: diffraction-limited focusing and subwavelength resolution imaging," *Science* **352**, 1190 (2016).
24. S. Zhang *et al.*, "High efficiency near diffraction-limited mid-infrared flat lenses based on metasurface reflectarrays," *Opt. Express* **24**, 18024 (2016).
25. A. Arbabi *et al.*, "Miniature optical planar camera based on a wide-angle metasurface doublet corrected for monochromatic aberrations," *Nat. Commun.* **7**, 13682 (2016).
26. S. Wang *et al.*, "Broadband achromatic optical metasurface devices," *Nat. Commun.* **8**, 187 (2017).
27. W. T. Chen *et al.*, "A broadband achromatic metalens for focusing and imaging in the visible," *Nat. Nanotechnol.* **13**, 220 (2018).
28. M. Meem *et al.*, "Broadband lightweight flat lenses for long-wave infrared imaging," *Proc. Natl. Acad. Sci.* **116**, 21375 (2019).
29. S. Shrestha *et al.*, "Broadband achromatic dielectric metalenses," *Light Sci. Appl.* **7**, 85 (2018).
30. F. Presutti and F. Monticone, "Focusing on bandwidth: achromatic metalens limits," *Optica* **7**, 624 (2020).
31. H. Liang *et al.*, "High performance metalenses: numerical aperture, aberrations, chromaticity, and trade-offs," *Optica* **6**, 1461 (2019).
32. E. Abbe, "Beiträge zur Theorie des Mikroskops und der mikroskopischen Wahrnehmung," *Arch. für mikroskopische Anat.* **9**, 413 (1873).
33. V. G. Veselago, "The electrodynamics of substances with simultaneously negative values of ϵ and μ," *Phys.-Usp.* **10**, 509 (1968).
34. J. B. Pendry *et al.*, "Extremely low frequency plasmons in metallic mesostructures," *Phys. Rev. Lett.* **76**, 4773 (1996).
35. J. B. Pendry *et al.*, "Magnetism from conductors and enhanced nonlinear phenomena," *IEEE Trans. Microw. Theory Tech.* **47**, 2075 (1999).
36. A. V. Kildishev and V. M. Shalaev, "Engineering space for light via transformation optics," *Opt. Lett.* **33**, 43 (2008).
37. A. A. High *et al.*, "Visible-frequency hyperbolic metasurface," *Nature* **522**, 192 (2015).
38. R. V. Craster and S. Guenneau, *Acoustic Metamaterials: Negative Refraction, Imaging, Lensing and Cloaking*, Vol. **166** (Springer Science & Business Media, 2012).
39. R. Zhu *et al.*, "Negative refraction of elastic waves at the deep-subwavelength scale in a single-phase metamaterial," *Nat. Commun.* **5**, 5510 (2014).
40. D. Wang *et al.*, "Realization of broadband polarization-insensitive negative refraction using water-based metamaterial," *Mater. Res. Express* **9**, 75801 (2022).

41. J. D. Joannopoulos, P. R. Villeneuve, and S. Fan, "Photonic crystals: putting a new twist on light," *Nature* **386**, 143 (1997).
42. M. E. Stewart *et al.*, "Quantitative multispectral biosensing and 1D imaging using quasi-3D plasmonic crystals," *Proc. Natl. Acad. Sci.* **103**, 17143 (2006).
43. V. M. Shalaev, "Optical negative-index metamaterials," *Nat. Photonics* **1**, 41 (2007).
44. N. I. Zheludev and Y. S. Kivshar, "From metamaterials to metadevices," *Nat. Mater.* **11**, 917 (2012).
45. R. H. Ritchie, "Plasma losses by fast electrons in thin films," *Phys. Rev.* **106**, 874 (1957).
46. J. Schilling, "Uniaxial metallo-dielectric metamaterials with scalar positive permeability," *Phys. Rev. E* **74**, 46618 (2006).
47. J. Yao *et al.*, "Optical negative refraction in bulk metamaterials of nanowires," *Science* **321**, 930 (2008).
48. T. Xu *et al.*, "All-angle negative refraction and active flat lensing of ultraviolet light," *Nature* **497**, 470 (2013).
49. L. Ferrari *et al.*, "Hyperbolic metamaterials and their applications," *Prog. Quantum Electron.* **40**, 1 (2015).
50. H. J. Lezec, J. A. Dionne, and H. A. Atwater, "Negative refraction at visible frequencies," *Science* **316**, 430 (2007).
51. H. S. Eisenberg *et al.*, "Diffraction management," *Phys. Rev. Lett.* **85**, 1863 (2000).
52. T. Pertsch *et al.*, "Anomalous refraction and diffraction in discrete optical systems," *Phys. Rev. Lett.* **88**, 093901 (2002).
53. D. N. Christodoulides, F. Lederer, and Y. Silberberg, "Discretizing light behaviour in linear and nonlinear waveguide lattices," *Nature* **424**, 817 (2003).
54. E. Verhagen *et al.*, "Three-dimensional negative index of refraction at optical frequencies by coupling plasmonic waveguides," *Phys. Rev. Lett.* **105**, 223901 (2010).
55. Y. Liu and X. Zhang, "Metasurfaces for manipulating surface plasmons," *Appl. Phys. Lett.* **103**, 141101 (2013).
56. B. Xu, T. Li, and S. Zhu, "Simulation of massless Dirac dynamics in plasmonic waveguide arrays," *Opt. Express* **26**, 13416 (2018).
57. L. Verslegers *et al.*, "Deep-subwavelength focusing and steering of light in an aperiodic metallic waveguide array," *Phys. Rev. Lett.* **103**, 33902 (2009).
58. X. Fan and G. P. Wang, "Nanoscale metal waveguide arrays as plasmon lenses," *Opt. Lett.* **31**, 1322 (2006).
59. Z. Kang and G. P. Wang, "Object distance-independent near-field subwavelength imaging of metal waveguide arrays," *J. Opt. Soc. Am. B* **25**, 1984 (2008).
60. J. M. Zeuner *et al.*, "Optical analogues for massless Dirac particles and conical diffraction in one dimension," *Phys. Rev. Lett.* **109**, 023602 (2012).
61. W. Song *et al.*, "Subwavelength self-imaging in cascaded waveguide arrays," *Adv. Photonics* **2**, 036001 (2020).
62. W. Song *et al.*, "Dispersionless coupling among optical waveguides by artificial gauge field," *Phys. Rev. Lett.* **129**, 53901 (2022).
63. Y. Liu *et al.*, "All-angle reflectionless negative refraction with ideal photonic Weyl metamaterials," *Light Sci. Appl.* **11**, 276 (2022).
64. J. B. Pendry, D. Schurig, and D. R. Smith, "Controlling electromagnetic fields," *Science* **312**, 1780 (2006).
65. D. Schurig *et al.*, "Metamaterial electromagnetic cloak at microwave frequencies," *Science* **314**, 977 (2006).
66. R. Liu *et al.*, "Broadband ground-plane cloak," *Science* **323**, 366 (2009).
67. Y. Lai *et al.*, "Complementary media invisibility cloak that cloaks objects at a distance outside the cloaking shell," *Phys. Rev. Lett.* **102**, 093901 (2009).
68. Y. Lai *et al.*, "Illusion optics: the optical transformation of an object into another object," *Phys. Rev. Lett.* **102**, 253902 (2009).
69. D. A. Genov, S. Zhang, and X. Zhang, "Mimicking celestial mechanics in metamaterials," *Nat. Phys.* **5**, 687 (2009).
70. C. Sheng *et al.*, "Trapping light by mimicking gravitational lensing," *Nat. Photonics* **7**, 902 (2013).
71. C. Sheng *et al.*, "Wavefront shaping through emulated curved space in waveguide settings," *Nat. Commun.* **7**, 10747 (2016).
72. A. V. Kildishev, A. Boltasseva, and V. M. Shalaev, "Planar photonics with metasurfaces," *Science* **339**, 1232009 (2013).
73. S. M. Kamali *et al.*, "A review of dielectric optical metasurfaces for wavefront control," *Nanophotonics* **7**, 1041 (2018).
74. P. Lalanne and P. Chavel, "Metalenses at visible wavelengths: past, present, perspectives," *Laser Photon. Rev.* **11**, 1600295 (2017).
75. S.-J. Kim *et al.*, "Dielectric metalens: properties and three-dimensional imaging applications," *Sensors* **21**, 4584 (2021).
76. W. T. Chen and F. Capasso, "Will flat optics appear in everyday life anytime soon?" *Appl. Phys. Lett.* **118**, 100503 (2021).
77. D. Wen *et al.*, "Helicity multiplexed broadband metasurface holograms," *Nat. Commun.* **6**, 8241 (2015).
78. Y.-W. Huang *et al.*, "Aluminum plasmonic multicolor meta-hologram," *Nano Lett.* **15**, 3122 (2015).
79. Y. Yao *et al.*, "Electrically tunable metasurface perfect absorbers for ultrathin mid-infrared optical modulators," *Nano Lett.* **14**, 6526 (2014).
80. J. Yu *et al.*, "Dielectric super-absorbing metasurfaces via PT symmetry breaking," *Optica* **8**, 1290 (2021).
81. P.-Y. Chen, C. Argyropoulos, and A. Alù, "Broadening the cloaking bandwidth with non-Foster metasurfaces," *Phys. Rev. Lett.* **111**, 233001 (2013).
82. K. Huang *et al.*, "Planar diffractive lenses: fundamentals, functionalities, and applications," *Adv. Mater.* **30**, 1704556 (2018).
83. W. T. Chen, A. Y. Zhu, and F. Capasso, "Flat optics with dispersion-engineered metasurfaces," *Nat. Rev. Mater.* **5**, 604 (2020).
84. M. K. Chen *et al.*, "Principles, functions, and applications of optical meta-lens," *Adv. Opt. Mater.* **9**, 2001414 (2021).
85. S. Sun *et al.*, "Gradient-index meta-surfaces as a bridge linking propagating waves and surface waves," *Nat. Mater.* **11**, 426 (2012).
86. S. Sun *et al.*, "High-efficiency broadband anomalous reflection by gradient meta-surfaces," *Nano Lett.* **12**, 6223 (2012).
87. M. Decker *et al.*, "High-efficiency dielectric Huygens' surfaces," *Adv. Opt. Mater.* **3**, 813 (2015).
88. A. Arbabi *et al.*, "Subwavelength-thick lenses with high numerical apertures and large efficiency based on high-contrast transmitarrays," *Nat. Commun.* **6**, 7069 (2015).
89. A. Arbabi *et al.*, "Dielectric metasurfaces for complete control of phase and polarization with subwavelength spatial resolution and high transmission," *Nat. Nanotechnol.* **10**, 937 (2015).
90. L. Huang *et al.*, "Dispersionless phase discontinuities for controlling light propagation," *Nano Lett.* **12**, 5750 (2012).
91. W. Zhu *et al.*, "A flat lens with tunable phase gradient by using random access reconfigurable metamaterial," *Adv. Mater.* **27**, 4739 (2015).
92. N. K. Grady *et al.*, "Terahertz metamaterials for linear polarization conversion and anomalous refraction," *Science* **340**, 1304 (2013).
93. W. Liu and Y. S. Kivshar, "Generalized Kerker effects in nanophotonics and meta-optics," *Opt. Express* **26**, 13085 (2018).
94. A. Hassanfiroozi *et al.*, "Toroidal-assisted generalized Huygens' sources for highly transmissive plasmonic metasurfaces," *Laser Photon. Rev.* **16**, 2100525 (2022).
95. M. V. Berry, "The adiabatic phase and Pancharatnam's phase for polarized light," *J. Mod. Opt.* **34**, 1401 (1987).
96. N. Shitrit *et al.*, "Optical spin Hall effects in plasmonic chains," *Nano Lett.* **11**, 2038 (2011).
97. S. Liu *et al.*, "Photonic spin Hall effect: fundamentals and emergent applications," *Opto-Electron. Adv.* **1**, 220007 (2022).

98. L. Cong *et al.*, "Polarization control in terahertz metasurfaces with the lowest order rotational symmetry," *Adv. Opt. Mater.* **3**, 1176 (2015).
99. C. Chen *et al.*, "Metasurfaces with planar chiral meta-atoms for spin light manipulation," *Nano Lett.* **21**, 1815 (2021).
100. Z. Li *et al.*, "Dielectric meta-holograms enabled with dual magnetic resonances in visible light," *ACS Nano* **11**, 9382 (2017).
101. J. P. B. Mueller *et al.*, "Metasurface polarization optics: independent phase control of arbitrary orthogonal states of polarization," *Phys. Rev. Lett.* **118**, 113901 (2017).
102. F. Aieta *et al.*, "Aberration-free ultrathin flat lenses and axicons at telecom wavelengths based on plasmonic metasurfaces," *Nano Lett.* **12**, 4932 (2012).
103. A. Maréchal, "Mechanical integrator for studying the distribution of light in the optical image," *J. Opt. Soc. Am.* **37**, 403_1 (1947).
104. F. Aieta *et al.*, "Aberrations of flat lenses and aplanatic metasurfaces," *Opt. Express* **21**, 31530 (2013).
105. S. M. Kamali *et al.*, "Highly tunable elastic dielectric metasurface lenses," *Laser Photon. Rev.* **10**, 1002 (2016).
106. X. Chen *et al.*, "Dual-polarity plasmonic metalens for visible light," *Nat. Commun.* **3**, 1198 (2012).
107. J. Chen *et al.*, "A high-efficiency dual-wavelength achromatic metalens based on Pancharatnam-Berry phase manipulation," *Opt. Express* **26**, 34919 (2018).
108. C. Zhang *et al.*, "Low-loss metasurface optics down to the deep ultraviolet region," *Light Sci. Appl.* **9**, 55 (2020).
109. Q. Fan *et al.*, "High-efficiency, linear-polarization-multiplexing metalens for long-wavelength infrared light," *Opt. Lett.* **43**, 6005 (2018).
110. B. H. Chen *et al.*, "GaN metalens for pixel-level full-color routing at visible light," *Nano Lett.* **17**, 6345 (2017).
111. A. Wang, Z. Chen, and Y. Dan, "Planar metalenses in the mid-infrared," *AIP Adv.* **9**, 85327 (2019).
112. L. Guo *et al.*, "Design of aluminum nitride metalens for broadband ultraviolet incidence routing," *Nanophotonics* **8**, 171 (2019).
113. M. Rossi, R. E. Kunz, and H.-P. Herzig, "Refractive and diffractive properties of planar micro-optical elements," *Appl. Opt.* **34**, 5996 (1995).
114. O. Avayu *et al.*, "Composite functional metasurfaces for multispectral achromatic optics," *Nat. Commun.* **8**, 14992 (2017).
115. D. Lin *et al.*, "Photonic multitasking interleaved Si nanoantenna phased array," *Nano Lett.* **16**, 7671 (2016).
116. E. Arbabi *et al.*, "Two-photon microscopy with a double-wavelength metasurface objective lens," *Nano Lett.* **18**, 4943 (2018).
117. M. Khorasaninejad *et al.*, "Achromatic metasurface lens at telecommunication wavelengths," *Nano Lett.* **15**, 5358 (2015).
118. H. Li *et al.*, "Bandpass-filter-integrated multiwavelength achromatic metalens," *Photonics Res.* **9**, 1384 (2021).
119. M. Khorasaninejad *et al.*, "Achromatic metalens over 60 nm bandwidth in the visible and metalens with reverse chromatic dispersion," *Nano Lett.* **17**, 1819 (2017).
120. E. Arbabi *et al.*, "Controlling the sign of chromatic dispersion in diffractive optics with dielectric metasurfaces," *Optica* **4**, 625 (2017).
121. Z.-B. Fan *et al.*, "A broadband achromatic metalens array for integral imaging in the visible," *Light Sci. Appl.* **8**, 67 (2019).
122. W. T. Chen *et al.*, "A broadband achromatic polarization-insensitive metalens consisting of anisotropic nanostructures," *Nat. Commun.* **10**, 355 (2019).
123. A. McClung, M. Mansouree, and A. Arbabi, "At-will chromatic dispersion by prescribing light trajectories with cascaded metasurfaces," *Light Sci. Appl.* **9**, 93 (2020).
124. A. A. Fathnan and D. A. Powell, "Bandwidth and size limits of achromatic printed-circuit metasurfaces," *Opt. Express* **26**, 29440 (2018).
125. R. S. Tucker, P.-C. Ku, and C. J. Chang-Hasnain, "Slow-light optical buffers: capabilities and fundamental limitations," *J. Light. Technol.* **23**, 4046 (2005).
126. Y. Wang *et al.*, "High-efficiency broadband achromatic metalens for near-IR biological imaging window," *Nat. Commun.* **12**, 5560 (2021).
127. F. Balli *et al.*, "A hybrid achromatic metalens," *Nat. Commun.* **11**, 3892 (2020).
128. M. Li *et al.*, "Dual-layer achromatic metalens design with an effective Abbe number," *Opt. Express* **28**, 26041 (2020).
129. M. Mansouree *et al.*, "Multifunctional 2.5D metastructures enabled by adjoint optimization," *Optica* **7**, 77 (2020).
130. F. Balli *et al.*, "An ultrabroadband 3D achromatic metalens," *Nanophotonics* **10**, 1259 (2021).
131. Y. Wang, Q. Fan, and T. Xu, "Design of high efficiency achromatic metalens with large operation bandwidth using bilayer architecture," *Opto-Electron. Adv.* **4**, 200008 (2021).
132. C. Chen *et al.*, "Spectral tomographic imaging with aplanatic metalens," *Light Sci. Appl.* **8**, 99 (2019).
133. A. Kalvach and Z. Szabó, "Aberration-free flat lens design for a wide range of incident angles," *J. Opt. Soc. Am. B* **33**, A66 (2016).
134. X. Luo *et al.*, "Recent advances of wide-angle metalenses: principle, design, and applications," *Nanophotonics* **11**, 1 (2022).
135. B. Groever, W. T. Chen, and F. Capasso, "Meta-lens doublet in the visible region," *Nano Lett.* **17**, 4902 (2017).
136. Z. Lin *et al.*, "Topology-optimized multilayered metaoptics," *Phys. Rev. Appl.* **9**, 44030 (2018).
137. C. Hao *et al.*, "Single-layer aberration-compensated flat lens for robust wide-angle imaging," *Laser Photon. Rev.* **14**, 2000017 (2020).
138. A. Martins *et al.*, "On metalenses with arbitrarily wide field of view," *ACS Photonics* **7**, 2073 (2020).
139. M. Y. Shalaginov *et al.*, "Single-element diffraction-limited fisheye metalens," *Nano Lett.* **20**, 7429 (2020).
140. F. Zhang *et al.*, "Extreme-angle silicon infrared optics enabled by streamlined surfaces," *Adv. Mater.* **33**, 2008157 (2021).
141. E. Lassalle *et al.*, "Imaging properties of large field-of-view quadratic metalenses and their applications to fingerprint detection," *ACS Photonics* **8**, 1457 (2021).
142. B. Xu *et al.*, "Metalens-integrated compact imaging devices for wide-field microscopy," *Adv. Photonics* **2**, 066004 (2020).
143. J. Chen *et al.*, "Planar wide-angle-imaging camera enabled by metalens array," *Optica* **9**, 431 (2022).
144. R. Paniagua-Dominguez *et al.*, "A metalens with a near-unity numerical aperture," *Nano Lett.* **18**, 2124 (2018).
145. S. J. Byrnes *et al.*, "Designing large, high-efficiency, high-numerical-aperture, transmissive meta-lenses for visible light," *Opt. Express* **24**, 5110 (2016).
146. M. Kang *et al.*, "Efficient focusing with large numerical aperture using a hybrid metalens," *Phys. Rev. Appl.* **13**, 44016 (2020).
147. A. Arbabi *et al.*, "Increasing efficiency of high numerical aperture metasurfaces using the grating averaging technique," *Sci. Rep.* **10**, 7214 (2020).
148. Y. Bao *et al.*, "Coherent pixel design of metasurfaces for multidimensional optical control of multiple printing-image switching and encoding," *Adv. Funct. Mater.* **28**, 1805306 (2018).
149. S. M. Kamali *et al.*, "Angle-multiplexed metasurfaces: encoding independent wavefronts in a single metasurface under different illumination angles," *Phys. Rev. X* **7**, 41056 (2017).
150. X. Zhang *et al.*, "Controlling angular dispersions in optical metasurfaces," *Light Sci. Appl.* **9**, 76 (2020).
151. E. T. F. Rogers and N. I. Zheludev, "Optical super-oscillations: sub-wavelength light focusing and super-resolution imaging," *J. Opt.* **15**, 94008 (2013).
152. D. Tang *et al.*, "Ultrabroadband superoscillatory lens composed by plasmonic metasurfaces for subdiffraction light focusing," *Laser Photon. Rev.* **9**, 713 (2015).

153. G. H. Yuan, E. T. F. Rogers, and N. I. Zheludev, "Achromatic super-oscillatory lenses with sub-wavelength focusing," *Light Sci. Appl.* **6**, e17036 (2017).
154. Z. Li *et al.*, "Achromatic broadband super-resolution imaging by super-oscillatory metasurface," *Laser Photon. Rev.* **12**, 1800064 (2018).
155. D. Tang, L. Chen, and J. Liu, "Visible achromatic super-oscillatory metasurfaces for sub-diffraction focusing," *Opt. Express* **27**, 12308 (2019).
156. F. Qin *et al.*, "A supercritical lens optical label-free microscopy: sub-diffraction resolution and ultra-long working distance," *Adv. Mater.* **29**, 1602721 (2017).
157. S. D. Campbell *et al.*, "Review of numerical optimization techniques for meta-device design," *Opt. Mater. Express* **9**, 1842 (2019).
158. W. Li *et al.*, "Topology optimization of photonic and phononic crystals and metamaterials: a review," *Adv. Theory Simul.* **2**, 1900017 (2019).
159. C.-H. Lin *et al.*, "Automatic inverse design of high-performance beam-steering metasurfaces via genetic-type tree optimization," *Nano Lett.* **21**, 4981 (2021).
160. M. P. Bendsoe and O. Sigmund, *Topology Optimization: Theory, Methods, and Applications* (Springer Science & Business Media, 2003).
161. J. S. Jensen and O. Sigmund, "Topology optimization for nano-photonics," *Laser Photon. Rev.* **5**, 308 (2011).
162. T. Phan *et al.*, "High-efficiency, large-area, topology-optimized metasurfaces," *Light Sci. Appl.* **8**, 48 (2019).
163. E. Tseng *et al.*, "Neural nano-optics for high-quality thin lens imaging," *Nat. Commun.* **12**, 6493 (2021).
164. Q. Fan *et al.*, "Trilobite-inspired neural nanophotonic light-field camera with extreme depth-of-field," *Nat. Commun.* **13**, 2130 (2022).
165. Y. Fan *et al.*, "Experimental demonstration of genetic algorithm based metalens design for generating side-lobe-suppressed, large depth-of-focus light sheet," *Laser Photon. Rev.* **16**, 2100425 (2022).
166. M. K. Chen *et al.*, "A meta-device for intelligent depth perception," *Adv. Mater.* 2107465 (2022).
167. M. K. Chen *et al.*, "Artificial intelligence in meta-optics," *Chem. Rev.* **122**, 15356 (2022).
168. P. Su *et al.*, "Large-area optical metasurface fabrication using nanostencil lithography," *Opt. Lett.* **46**, 2324 (2021).
169. S. W. D. Lim, M. L. Meretska, and F. Capasso, "A high aspect ratio inverse-designed holey metalens," *Nano Lett.* **21**, 8642 (2021).
170. F. Zhao *et al.*, "Metalens-assisted system for underwater imaging," *Laser Photon. Rev.* **15**, 2100097 (2021).
171. M. K. Chen *et al.*, "Meta-lens in the sky," *IEEE Access* **10**, 46552 (2022).
172. T. W. Hughes *et al.*, "A perspective on the pathway toward full wave simulation of large area metalenses," *Appl. Phys. Lett.* **119**, 150502 (2021).
173. A. She *et al.*, "Large area metalenses: design, characterization, and mass manufacturing," *Opt. Express* **26**, 1573 (2018).
174. J.-S. Park *et al.*, "All-glass, large metalens at visible wavelength using deep-ultraviolet projection lithography," *Nano Lett.* **19**, 8673 (2019).
175. T. Hu *et al.*, "CMOS-compatible a-Si metalenses on a 12-inch glass wafer for fingerprint imaging," *Nanophotonics* **9**, 823 (2020).
176. C. A. Dirdal *et al.*, "Towards high-throughput large-area metalens fabrication using UV-nanoimprint lithography and Bosch deep reactive ion etching," *Opt. Express* **28**, 15542 (2020).
177. G. Yoon *et al.*, "Printable nanocomposite metalens for high-contrast near-infrared imaging," *ACS Nano* **15**, 698 (2021).
178. V. J. Einck *et al.*, "Scalable nanoimprint lithography process for manufacturing visible metasurfaces composed of high aspect ratio TiO2 meta-atoms," *ACS Photonics* **8**, 2400 (2021).
179. D. C. O'Shea *et al.*, *Diffractive Optics: Design, Fabrication, and Test*, Vol. **62** (SPIE Press, 2004).
180. L. Hazra, "Diffractive optical elements: past, present, and future," *Proc. SPIE* **3729**, 198 (1999).
181. Y. Peng *et al.*, "Learned large field-of-view imaging with thin-plate optics," *ACM Trans. Graph.* **38**, 211 (2019).
182. G. J. Swanson, "The theory and design of multi-level diffractive optical elements," MIT Tech. Rep. 854 (1989).
183. D. W. Sweeney and G. E. Sommargren, "Harmonic diffractive lenses," *Appl. Opt.* **34**, 2469 (1995).
184. S. Sinzinger and M. Testorf, "Transition between diffractive and refractive micro-optical components," *Appl. Opt.* **34**, 5970 (1995).
185. P. Wang, N. Mohammad, and R. Menon, "Chromatic-aberration-corrected diffractive lenses for ultra-broadband focusing," *Sci. Rep.* **6**, 21545 (2016).
186. L. L. Doskolovich *et al.*, "Design of diffractive lenses operating at several wavelengths," *Opt. Express* **28**, 11705 (2020).
187. M. Meem *et al.*, "Inverse-designed achromatic flat lens enabling imaging across the visible and near-infrared with diameter > 3 mm and NA = 0.3," *Appl. Phys. Lett.* **117**, 041101 (2020).
188. X. Xiao *et al.*, "Large-scale achromatic flat lens by light frequency-domain coherence optimization," *Light Sci. Appl.* **11**, 323 (2022).
189. S. Banerji *et al.*, "Extreme-depth-of-focus imaging with a flat lens," *Optica* **7**, 214 (2020).
190. Y. Peng *et al.*, "The diffractive achromat full spectrum computational imaging with diffractive optics," *ACM Trans. Graph.* **35**, 31 (2016).
191. B. K. Yildırım, H. Kurt, and M. Turduev, "Ultra-compact, high-numerical-aperture achromatic multilevel diffractive lens via metaheuristic approach," *Photonics Res.* **9**, 2095 (2021).
192. R. Hooke and T. A. Jeeves, ""Direct search" solution of numerical and statistical problems," *J. ACM* **8**, 212 (1961).
193. M. A. Seldowitz, J. P. Allebach, and D. W. Sweeney, "Synthesis of digital holograms by direct binary search," *Appl. Opt.* **26**, 2788 (1987).
194. R. L. Haupt and D. H. Werner, *Genetic Algorithms in Electromagnetics* (John Wiley & Sons, 2007).
195. J. Engelberg and U. Levy, "Standardizing flat lens characterization," *Nat. Photonics* **16**, 171 (2022).
196. N. Mohammad *et al.*, "Broadband imaging with one planar diffractive lens," *Sci. Rep.* **8**, 2799 (2018).
197. M. Meem, A. Majumder, and R. Menon, "Full-color video and still imaging using two flat lenses," *Opt. Express* **26**, 26866 (2018).
198. R. J. Lin *et al.*, "Achromatic metalens array for full-colour light-field imaging," *Nat. Nanotechnol.* **14**, 227 (2019).
199. A. Ndao *et al.*, "Octave bandwidth photonic fishnet-achromatic-metalens," *Nat. Commun.* **11**, 3205 (2020).
200. T. Sun *et al.*, "Polarization-insensitive achromatic metalens based on computational wavefront coding," *Opt. Express* **29**, 31902 (2021).
201. M. Meem *et al.*, "Imaging from the visible to the longwave infrared wavelengths via an inverse-designed flat lens," *Opt. Express* **29**, 20715 (2021).
202. F. Zhou *et al.*, "Vector light field display based on an intertwined flat lens with large depth of focus," *Optica* **9**, 288 (2022).
203. X. Luo *et al.*, "Subwavelength interference of light on structured surfaces," *Adv. Opt. Photonics* **10**, 757 (2018).
204. L. Liu *et al.*, "Large area and deep sub-wavelength interference lithography employing odd surface plasmon modes," *Sci. Rep.* **6**, 30450 (2016).
205. X. Luo, "Plasmonic metalens for nanofabrication," *Natl. Sci. Rev.* **5**, 137 (2018).

206. H.-S. Ee and R. Agarwal, "Tunable metasurface and flat optical zoom lens on a stretchable substrate," *Nano Lett.* **16**, 2818 (2016).
207. K. Iwami *et al.*, "Demonstration of focal length tuning by rotational varifocal moiré metalens in an IR-A wavelength," *Opt. Express* **28**, 35602 (2020).
208. Y. Luo *et al.*, "Varifocal metalens for optical sectioning fluorescence microscopy," *Nano Lett.* **21**, 5133 (2021).
209. S. Colburn, A. Zhan, and A. Majumdar, "Varifocal zoom imaging with large area focal length adjustable metalenses," *Optica* **5**, 825 (2018).
210. E. Arbabi *et al.*, "MEMS-tunable dielectric metasurface lens," *Nat. Commun.* **9**, 812 (2018).
211. M. Y. Shalaginov *et al.*, "Reconfigurable all-dielectric metalens with diffraction-limited performance," *Nat. Commun.* **12**, 1225 (2021).
212. R. Fu *et al.*, "Reconfigurable step-zoom metalens without optical and mechanical compensations," *Opt. Express* **27**, 12221 (2019).
213. L. Yu *et al.*, "Spin angular momentum controlled multifunctional all-dielectric metasurface doublet," *Laser Photon. Rev.* **14**, 1900324 (2020).
214. M. K. Chen *et al.*, "Edge detection with meta-lens: from one dimension to three dimensions," *Nanophotonics* **10**, 3709 (2021).
215. L. Li *et al.*, "Metalens-array–based high-dimensional and multiphoton quantum source," *Science* **368**, 1487 (2020).
216. M. L. Tseng *et al.*, "Vacuum ultraviolet nonlinear metalens," *Sci. Adv.* **8**, eabn5644 (2022).
217. X. Hua *et al.*, "Ultra-compact snapshot spectral light-field imaging," *Nat. Commun.* **13**, 2732 (2022).
218. M. Park *et al.*, "Virtual-moving metalens array enabling light-field imaging with enhanced resolution," *Adv. Opt. Mater.* **8**, 2000820 (2020).
219. Q. Guo *et al.*, "Compact single-shot metalens depth sensors inspired by eyes of jumping spiders," *Proc. Natl. Acad. Sci.* **116**, 22959 (2019).
220. C. Jin *et al.*, "Dielectric metasurfaces for distance measurements and three-dimensional imaging," *Adv. Photonics* **1**, 036001 (2019).
221. C. Chen *et al.*, "Highly efficient metasurface quarter-wave plate with wave front engineering," *Adv. Photonics Res.* **2**, 2000154 (2021).
222. R. M. A. Azzam, N. M. Bashara, and S. S. Ballard, "Ellipsometry and polarized light," *Phys. Today* **31**, 72 (1978).
223. M. Khorasaninejad *et al.*, "Multispectral chiral imaging with a metalens," *Nano Lett.* **16**, 4595 (2016).
224. Z. Yang *et al.*, "Generalized Hartmann-Shack array of dielectric metalens sub-arrays for polarimetric beam profiling," *Nat. Commun.* **9**, 4607 (2018).
225. E. Arbabi *et al.*, "Full-Stokes imaging polarimetry using dielectric metasurfaces," *ACS Photonics* **5**, 3132 (2018).
226. N. A. Rubin *et al.*, "Matrix Fourier optics enables a compact full-Stokes polarization camera," *Science* **365**, eaax1839 (2019).
227. X. Ye *et al.*, "Chip-scale metalens microscope for wide-field and depth-of-field imaging," *Adv. Photonics* **4**, 046006 (2022).
228. H. Pahlevaninezhad *et al.*, "Nano-optic endoscope for high-resolution optical coherence tomography *in vivo*," *Nat. Photonics* **12**, 540 (2018).
229. Y. Liu *et al.*, "Meta-objective with sub-micrometer resolution for microendoscopes," *Photonics Res.* **9**, 106 (2021).
230. M. Pahlevaninezhad *et al.*, "Metasurface-based bijective illumination collection imaging provides high-resolution tomography in three dimensions," *Nat. Photonics* **16**, 203 (2022).
231. P. Huo *et al.*, "Photonic spin-multiplexing metasurface for switchable spiral phase contrast imaging," *Nano Lett.* **20**, 2791 (2020).
232. J. Zhou *et al.*, "Two-dimensional optical spatial differentiation and high-contrast imaging," *Natl. Sci. Rev.* **8**, nwaa176 (2021).
233. Y. Kim *et al.*, "Spiral metalens for phase contrast imaging," *Adv. Funct. Mater.* **32**, 2106050 (2022).
234. J. Zhou *et al.*, "Nonlinear computational edge detection metalens," *Adv. Funct. Mater.* **32**, 2204734 (2022).
235. H. Kwon *et al.*, "Single-shot quantitative phase gradient microscopy using a system of multifunctional metasurfaces," *Nat. Photonics* **14**, 109 (2020).
236. C. Guo, H. Wang, and S. Fan, "Squeeze free space with nonlocal flat optics," *Optica* **7**, 1133 (2020).
237. O. Reshef *et al.*, "An optic to replace space and its application towards ultra-thin imaging systems," *Nat. Commun.* **12**, 3512 (2021).
238. K. Shastri *et al.*, "To what extent can space be compressed? Bandwidth limits of spaceplates," *Optica* **9**, 738 (2022).
239. C. Chen *et al.*, "Bifacial-metasurface-enabled pancake metalens with polarized space folding," *Optica* **9**, 1314 (2022).
240. J. Hua *et al.*, "Foveated glasses-free 3D display with ultrawide field of view via a large-scale 2D-metagrating complex," *Light Sci. Appl.* **10**, 213 (2021).
241. J. Hua, W. Qiao, and L. Chen, "Recent advances in planar optics-based glasses-free 3D displays," *Front. Nanotechnol.* **4**, 829011 (2022).
242. G.-Y. Lee *et al.*, "Metasurface eyepiece for augmented reality," *Nat. Commun.* **9**, 4562 (2018).
243. S.-W. Nam *et al.*, "Aberration-corrected full-color holographic augmented reality near-eye display using a Pancharatnam-Berry phase lens," *Opt. Express* **28**, 30836 (2020).
244. Z. Li *et al.*, "Meta-optics achieves RGB-achromatic focusing for virtual reality," *Sci. Adv.* **7**, eabe4458 (2021).
245. H. Kwon *et al.*, "Nonlocal metasurfaces for optical signal processing," *Phys. Rev. Lett.* **121**, 173004 (2018).
246. F. Monticone, C. A. Valagiannopoulos, and A. Alù, "Parity-time symmetric nonlocal metasurfaces: all-angle negative refraction and volumetric imaging," *Phys. Rev. X* **6**, 041018 (2016).
247. A. C. Overvig, S. C. Malek, and N. Yu, "Multifunctional nonlocal metasurfaces," *Phys. Rev. Lett.* **125**, 017402 (2020).
248. C. J. Chang-Hasnain and W. Yang, "High-contrast gratings for integrated optoelectronics," *Adv. Opt. Photonics* **4**, 379 (2012).
249. M. F. Limonov *et al.*, "Fano resonances in photonics," *Nat. Photonics* **11**, 543 (2017).
250. C. W. Hsu *et al.*, "Observation of trapped light within the radiation continuum," *Nature* **499**, 188 (2013).
251. K. Koshelev *et al.*, "Asymmetric metasurfaces with high-Q resonances governed by bound states in the continuum," *Phys. Rev. Lett.* **121**, 193903 (2018).
252. S. C. Malek *et al.*, "Multifunctional resonant wavefront-shaping meta-optics based on multilayer and multi-perturbation nonlocal metasurfaces," *Light Sci. Appl.* **11**, 246 (2022).
253. D. Lee *et al.*, "Metasurfaces-based imaging and applications: from miniaturized optical components to functional imaging platforms," *Nanoscale Adv.* **2**, 605 (2020).
254. M. Pan *et al.*, "Dielectric metalens for miniaturized imaging systems: progress and challenges," *Light Sci. Appl.* **11**, 195 (2022).
255. Y. He, B. Song, and J. Tang, "Optical metalenses: fundamentals, dispersion manipulation, and applications," *Front. Optoelectron.* **15**, 24 (2022).
256. S. Ijaz *et al.*, "The dawn of metadevices: from contemporary designs to exotic applications," *Adv. Devices Instrum.* **2022**, 9861078 (2022).
257. D. R. Smith, J. B. Pendry, and M. C. K. Wiltshire, "Metamaterials and negative refractive index," *Science* **305**, 788 (2004).
258. S. A. Ramakrishna, "Physics of negative refractive index materials," *Reports Prog. Phys.* **68**, 449 (2005).
259. C. M. Soukoulis, S. Linden, and M. Wegener, "Negative refractive index at optical wavelengths," *Science* **315**, 47 (2007).
260. C. Ma, R. Aguinaldo, and Z. Liu, "Advances in the hyperlens," *Chinese Sci. Bull.* **55**, 2618 (2010).
261. W. Zang *et al.*, "Chromatic dispersion manipulation based on metalenses," *Adv. Mater.* **32**, 1904935 (2020).

262. W. Li, J. Qi, and A. Sihvola, "Meta-imaging: from non-computational to computational," *Adv. Opt. Mater.* **8**, 2001000 (2020).
263. J. Chen *et al.*, "Metamaterials: from fundamental physics to intelligent design," *Interdiscip. Mater.* **2**, 12049 (2022).
264. Q. Ma *et al.*, "Information metasurfaces and intelligent metasurfaces," *Photon. Insights* **1**, R01 (2022).
265. Y. Guo *et al.*, "Classical and generalized geometric phase in electromagnetic metasurfaces," *Photon. Insights* **1**, R03 (2022).
266. C. Wang *et al.*, "Plasmonic structures, materials and lenses for optical lithography beyond the diffraction limit: a review," *Micromachines* **7**, 118 (2016).
267. Z. Li *et al.*, "Inverse design enables large-scale high-performance meta-optics reshaping virtual reality," *Nat. Commun.* **13**, 2409 (2022).
268. N. Wang *et al.*, "Intelligent designs in nanophotonics: from optimization towards inverse creation," *PhotoniX* **2**, 22 (2021).
269. J. Jiang, M. Chen, and J. A. Fan, "Deep neural networks for the evaluation and design of photonic devices," *Nat. Rev. Mater.* **6**, 679 (2021).
270. S. Molesky *et al.*, "Inverse design in nanophotonics," *Nat. Photonics* **12**, 659 (2018).
271. M. M. R. Elsawy *et al.*, "Numerical optimization methods for metasurfaces," *Laser Photon. Rev.* **14**, 1900445 (2020).
272. C. Zuo *et al.*, "Deep learning in optical metrology: a review," *Light Sci. Appl.* **11**, 39 (2022).
273. V. Boominathan *et al.*, "Recent advances in lensless imaging," *Optica* **9**, 1 (2022).